Search For Exclusive Diphoton Production with Intact Protons in pp Collisions at the LHC

Justin Williams

B.A. Physics, Mathematics, University of West Florida, 2016

Submitted to the graduate degree program in Department of Physics and Astronomy and the Graduate Faculty of the University of Kansas in partial fulfillment of the requirements for the degree of Doctor of Philosophy.

Committee members

Dr. Christophe Royon, Chairperson

Dr. Stephen Sanders

Dr. Christopher Rogan

Dr. Philip Barringer

Dr. Ken Fischer, External Reviewer

Date defended: May 10, 2021

The Dissertation Committee for Justin Williams certifies
that this is the approved version of the following dissertation :

Search For Exclusive Diphoton Production with Intact Protons in pp Collisions at the LHC

Dr. Christophe Royon, Chairperson

Date approved: May 10, 2021

Abstract

The Standard Model of particle physics has been largely successful in describing observed phenomena in the universe, but it is still believed to be incomplete. Many theories that address the shortcomings of the Standard Model also predict mechanisms of new physics that would enhance the four-photon coupling cross-section. In this work, a method to search for evidence of new physics in the diphoton final state is discussed using the CMS and PPS detectors. The quasi-real photon fluxes generated by protons at the LHC give rise to photon-photon interactions according to the Equivalent Photon Approximation. These electromagnetic interactions can create the exclusive production of two new photons while the protons remain intact in the final state and can be measured further down the LHC beam line by dedicated proton detectors. Measuring the forward protons and correlating their kinematics to that of the central two-photon system gives a strong discrimination against inclusive backgrounds. The data used in this analysis was collected with the CMS detector at the LHC from proton-proton collisions at a center-of-mass energy of 13 TeV. A study using data from 2016 only is presented before detailing an analysis of the full Run II data set – data collected in 2016, 2017, and 2018. In both studies, no events are observed above the Standard Model background prediction. The first limits are placed on the four photon anomalous coupling process and the strongest limits are placed on axion-like particle production in the mass range of 500 – 2000 GeV.

Acknowledgements

First and foremost, I would like to thank my doctoral adviser, Dr. Christophe Royon, for giving me a platform to develop my research and communication skills from the very beginning. Within the first three months of beginning graduate school, Dr. Royon allowed me to begin a research project and present at an international conference in Italy. Thank you for allowing me to be treated as a collaborator and a friend instead of only an employee.

Next, I would like to thank all of my CMS and PPS colleagues whose efforts have made this work possible. In particular I would like to thank Antonio Vilela Pereira and Ksenia Shchelina for guiding the PPS studies. I would also like to thank Jan Kaspar, Frigyes Nemes, and Andrea Bellora for their hard work on the PPS alignment, optics, and efficiencies, respectively.

I want to thank my fellow graduate students in our CMS KU group who have helped me through the last five years – Cristian, Cole, and Tommaso. Our constant discussions around the espresso machine both advanced and delayed the timeline of my degree.

I would like to thank the postdocs who mentored me in CMS analysis techniques – Laurent Forthomme and Georgios Kritiras.

I want to thank the Madison and Lila Self Graduate Fellowship program who funded four years of my research as well as helped me to develop my leadership skills through the development program.

I want to thank my undergraduate adviser, Dr. Christophe Varney, who helped me to hone my research skills and encouraged me to pursue a Ph.D in physics.

I would like to thank my family who has constantly supported me in all of my life's endeavors – Mom, Dad, and Kaylie.

Finally, and most importantly, I want to thank my wife Emily Williams for her constant support and grace throughout my time in graduate school. Thank you for supporting me as I worked late into the night or as I slept by the computer waiting for an important email. Thank you for allowing me to work for an extra hour when I promised it would only be 10 minutes as you sat outside of the physics building to pick me up. Thank you for listening to me rehearse dozens of talks on topics that were completely foreign to you.

Kansas, May 2021

Justin Williams

Contents

List of Figures

List of Tables

Chapter 1: Introduction

Contents

The Standard Model (SM) of particle physics has been exceptionally successful in predicting experimental results with extreme precision. However, several experimental and theoretical findings imply the existence of physics beyond the Standard Model (BSM). A few of the experimental contradictions are the existence of dark matter, the phenomenon of neutrino oscillations, and the measurement of the magnetic moment of the muon [1]. From a theoretical perspective, the hierarchy problem of the SM, the mechanism mediating the force of gravity, and the violation of charge and parity (CP) symmetries give rise to a need for a more complete theory.

Experiments around the world use novel methods and advanced technologies to search for explanations to these hints of new physics. Specifically in collider-based experiments, physicists search for final-state SM particles that could decay from new particles or processes not predicted by the SM. It has become increasingly popular to study photon-photon interactions as they are believed to couple with many new particles that could exist within our experimental reach.

1.1 Photon-photon interactions

The self interaction of photons is a purely quantum-mechanical effect attributed to the properties of the vacuum. Photon-photon collisions have historically been studied in collisions involving leptons such as at HERA and LEP. More recently, photon induced processes have been measured in proton-antiproton collisions at the Tevatron by the production of lepton pairs [2] and J/ψ mesons [3].

Although the Large Hadron Collider (LHC) primarily collides protons and heavy ions (HIs), the LHC provides a great environment for producing photon-photon collisions. As protons (or HIs) are accelerated around the LHC ring, these accelerating, charged particles emit a large amount of electromagnetic (EM) radiation that can be computed using the Equivalent Photon Approximation (EPA) [4, 5]. These EM fields can be equally viewed as fluxes of virtual photons.

When the charged particles pass near to each other without colliding, there is an opportunity to observe photon-photon collisions as illustrated in Figure 1.1.

There are advantages for using proton-proton (pp) collisions or HI collisions to produce an environment conducive to photon-photon collisions. In HI collisions, larger effective (quasi-real) photon fluxes exist because the EM radiation scales as Z^4 where Z is the

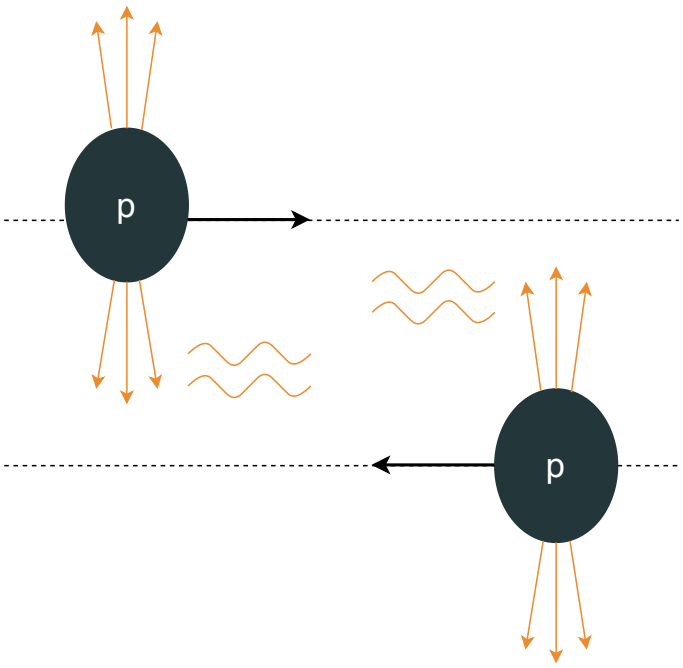

Figure 1.1: Schematic of two protons passing near to each other close enough for their electromagnetic fields to interact as virtual photons according to the EPA.

atomic number of the atom [6]. On the other hand, in pp collisions, much higher two-photon ($\gamma\gamma$) energies can be reached as a consequence of the smaller impact parameter [7] and the beam energy. In the case of the LHC, these $\gamma\gamma$ energies can be as high as 2.5 TeV.

Since photon-photon collisions occur in the case where the incoming particles do not interact hadronically [1], there are two distinct advantages. First, the collisions generally provide "clean" events where some central system is produced exclusively. This is opposed to a typical collision at a collider where the incoming particles are completely destroyed and produce a more complicated physics system in the process. Secondly, there is a chance for the incoming particles to survive the interaction and continue traveling through the accelerator. A later discussion in section 2.3 will detail the benefits of measuring the original particles after the interaction. The probability for a particle to remain intact after these EM interactions is known as the survival factor [8]. The average survival factor for protons at LHC energies has been calculated on the order of 90% [9].

1.2 Light-by-light scattering

Photon collisions provide excellent insight into the theory of quantum electrodynamics (QED) – the quantum theory of electromagnetism. Both the CMS and ATLAS collaborations have recently observed the process of two photons interacting to produce two new final state photons in HI collisions [10–12]. This process of $\gamma\gamma \rightarrow \gamma\gamma$ is a fundamental process of QED and is known as Light-by-Light (LbL) scattering. In the SM, the LbL pro-

[1] Gluon exchange processes are also possible but are not as prevalent at high energies as photon exchange processes.

cess is mediated by a box diagram of an electrically charged lepton, quark or W boson as shown in Figure 1.2.

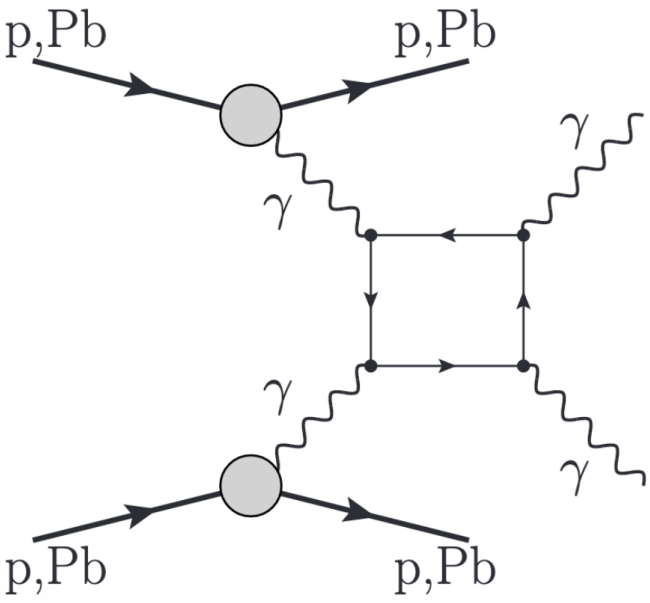

Figure 1.2: SM LbL scattering mediated by a box of either a quark, lepton, or W boson. Figure is extracted from Reference [6].

Since it proceeds at the lowest order in the fine structure constant (a_{em}), the elastic LbL reaction has not been observed directly until the aforementioned LHC results; although, it has been indirectly tested by the measurements of the magnetic moment of the electron [13] and muon [1, 14]. Similar processes have been detected at much lower energies such as photon scattering in the Coulomb field of a nucleus (Delbrück scattering) [15], a single photon splitting into two photons via interactions with external fields (photon splitting) [16], real photons combining to produce an e^+e^- pair [17], and multi-photon Compton scattering [18].

1.3 Anomalous couplings

LbL scattering is also interesting to study in the context of BSM physics as effects of new physics could lead to an increased production rate (cross-section) of the $\gamma\gamma \to \gamma\gamma$ process. Using pp collisions at the LHC, the experimental reach is powerful enough to probe the electroweak scale. One particular motivation is the existence of any new heavy, charged particle, which would contribute to the 4γ coupling. New particles with exotic charges are predicted by many models such as those of composite Higgs [19], warped extra dimensions [20], and Kaluza-Klein gravitons, [21] to name a few. With the assumption of a new mass scale heavier than the reachable experimental energy, the 4γ interactions can be described by an effective Lagrangian using dimension-8 operators

$$\mathcal{L}_{4\gamma} = \zeta_1 F_{\mu\nu}F^{\mu\nu}F_{\rho\sigma}F^{\rho\sigma} + \zeta_2 F_{\mu\nu}F^{\nu\rho}F_{\rho\beta}F^{\beta\mu} \quad (1.1)$$

These operators are identically zero in the SM, but in the case of a loop of a heavy

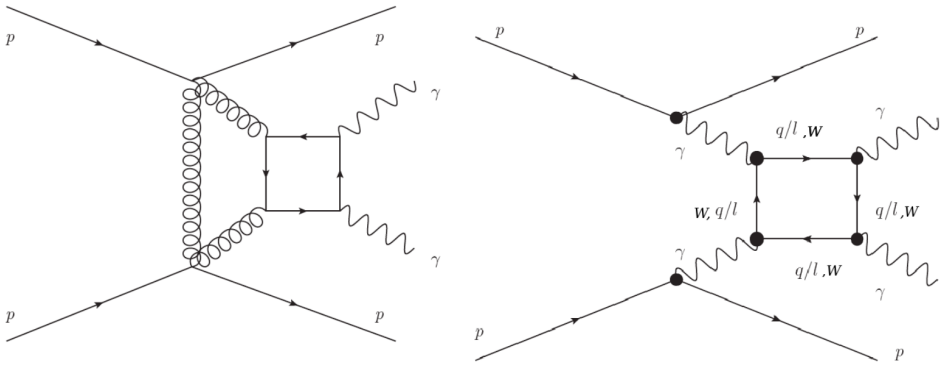

Figure 1.3: Feynman diagrams of processes predicted by the SM leading to exclusive diphoton production with two intact protons. The left diagram is a QCD process induced by gluon exchange, and the right diagram is a QED process induced by photon exchange. Figure extracted from Reference [22].

charged particle, the contribution to the 4γ process would be

$$\zeta_i = \frac{a_{\text{em}}^2 Q_{\text{eff}}^4}{m^4} N c_{i,S} \tag{1.2}$$

where

$$c_{1,S} = \begin{cases} \frac{1}{288} & S = 0 \\ -\frac{1}{36} & S = \frac{1}{2} \\ -\frac{5}{32} & S = 1 \end{cases}, \qquad c_{2,S} = \begin{cases} \frac{1}{360} & S = 0 \\ \frac{7}{90} & S = \frac{1}{2} \\ \frac{27}{40} & S = 1 \end{cases} \tag{1.3}$$

and S denotes the spin of the particle with mass m and charge Q_{eff}. The factor N accounts for all additional multiplicities such as color and flavor. Resonances of neutral particles could also contribute to non-zero ζ_i values as will be discussed in Section 1.4.

Using the effective Lagrangian in equation 1.1, the 4γ differential cross-section can be calculated as

$$\frac{d\sigma}{d\Omega} = \frac{1}{16\pi^2 s} \left(s^2 + t^2 + st\right)^2 \left(48(\zeta_1)^2 + 40\zeta_1\zeta_2 + 11(\zeta_2)^2\right) \tag{1.4}$$

where s and t are the Mandlestam variables.

Previous collider experiments have only investigated anomalous couplings of this nature using general searches with multi-purpose detectors and prior to the study detailed in Chapter 3, no collider limits existed on the 4γ anomalous coupling. Rather, using precision physics, the 4γ coupling can be probed with pp collisions at the LHC using proton detection techniques that are described in detail in Section 2.3. Since the process of interest is photon-induced, the original protons have a very high chance to remain intact in the final state as previously discussed. Anomalous 4γ couplings can be studied by measuring the two final state photons in one of the general purpose detectors and the two outgoing protons in dedicated forward proton detectors.

There are two processes in the SM to produce two photons exclusively with both protons intact, and they are shown in Figure 1.3.

The first diagram is the quantum chromodynamics (QCD) process of diphoton pro-

duction via (colorless) gluon exchange, and the second is the QED process of diphoton production via photon exchange discussed in Section 1.2. The contributions of each of these processes to the overall exclusive diphoton cross-section has been studied as a function of the minimum requirement on the mass of the photon pair. In the study, each photon was required to have a p_T above 10 GeV. In Figure 1.4, it is clear that the QCD process dominates at low diphoton masses while the QED process dominates at the higher diphoton masses – within the mass acceptance of the forward proton detectors at the LHC. Furthermore, at higher masses above approximately 100 GeV, it is the $W^{\pm}$ boson loop that is superior.

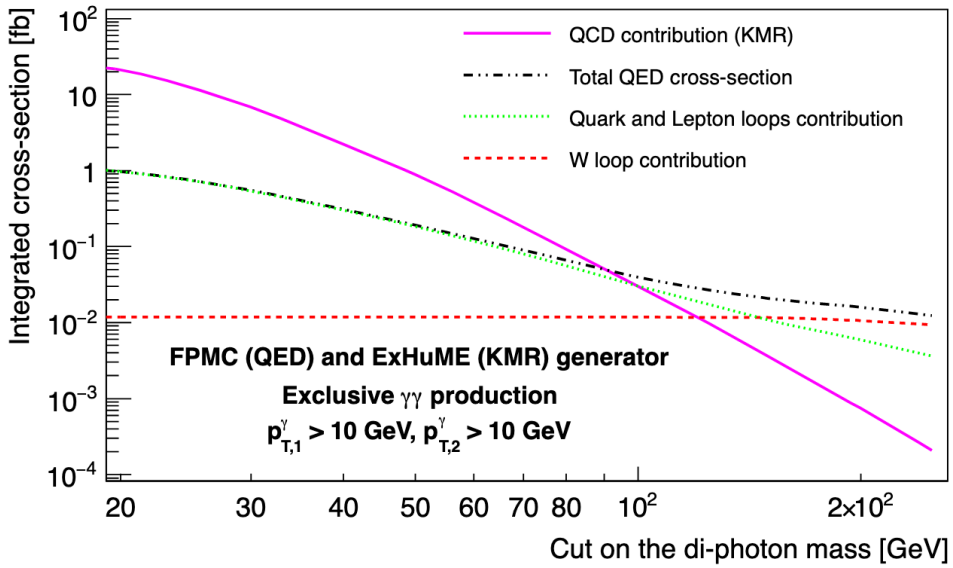

Figure 1.4: The integrated cross-section of various exclusive diphoton production methods with intact protons as a function of the cut on the diphoton mass. The pink and black dotted lines show the contribution to the integrated cross-section for the QCD and QED processes, respectively. The green and red lines show the W boson and quark/lepton contributions to the QED cross-section, respectively. Figure extracted from Reference [22].

To show the feasibility of performing this type of search at the LHC, a proposed set of selection criteria was studied to yield a high signal efficiency while providing a strong background suppression for 300 fb^{-1} of data collected at $\sqrt{s} = 14$ TeV. The backgrounds considered include SM exclusive $\gamma\gamma$, Drell-Yan (DY) dijet, double pomeron exchange (DPE), and inclusive $\gamma\gamma$ events. The event selection can be seen in Table 1.1 along with the expected number of signal and background events passing each selection requirement. All major sources of backgrounds are considered at detector level that would give two photons in the central detector plus two opposite-side forward protons. Even events where both protons are destroyed can act as background events for this study because of a phenomenon at the LHC called "pileup". The LHC circulates protons not in a continuous stream but in tightly packed "bunches" containing millions of protons. Every time these bunches cross, more than one pp collision takes place – this is known as pileup. In a given bunch crossing, there can be up to 60 interactions that create many particles in the detector as depicted in Figure 1.5. When one interaction produces two photons inclu-

sively and one or more unrelated interactions produce forward protons, these overlapping interactions create a background – this is the background created by pileup and it is illustrated in Figure 1.6.

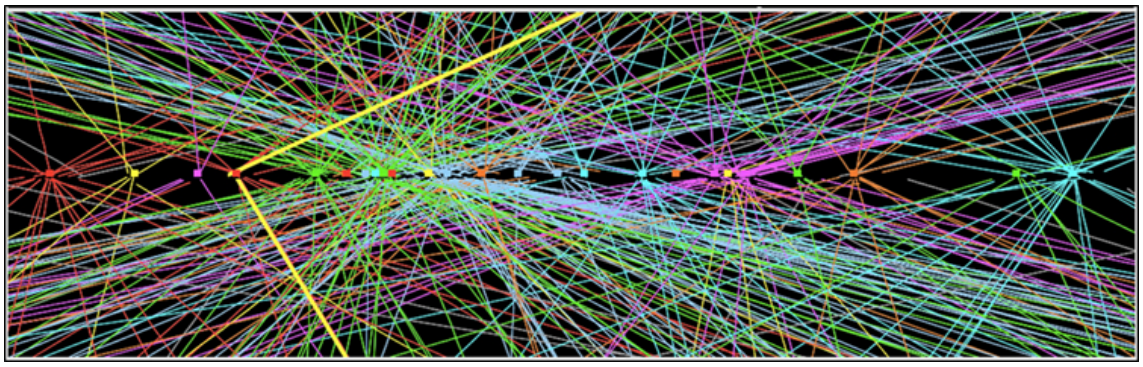

Figure 1.5: A depiction of many interactions taking place during one LHC bunch crossing.

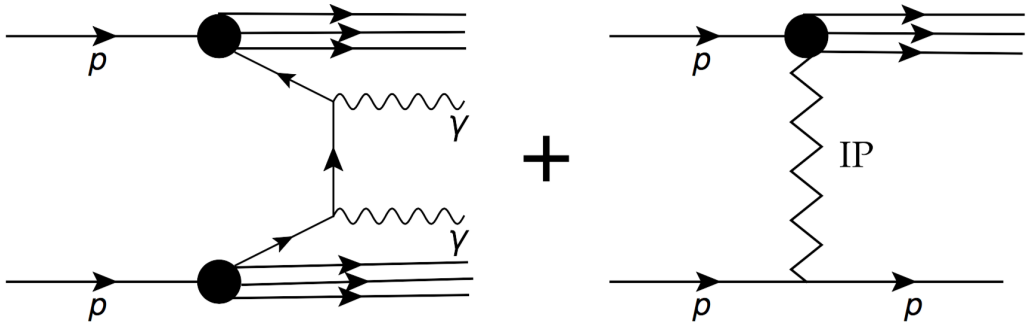

Figure 1.6: Two overlapping interactions that could create two photons in the central detector plus one or more protons in the forward detectors. This effect is referred to as pileup. Figure extracted from Reference [23].

The first step of the selection criteria requires that the fractional momentum loss, ξ, of the protons be within the acceptance of the forward proton detectors at the LHC ($0.015 < \xi < 0.15$). In accordance with the anomalous quartic gauge coupling (AQGC) kinematics, photons are also required to be produced at high transverse momentum ($p_{T\,1,(2)} > 200, (100)$ GeV) and high mass ($m_{\gamma\gamma} > 600$ GeV). After these cuts, the background contributions from the exclusive LbL process are negligible, and the dominant source is from SM diphoton production in association with pileup protons. To suppress this background, the signal event topology is used requiring photons to be produced back-to-back with respect to the azimuthal angle and to have similar p_T values. Finally, since all final state particles are measured, the background can be almost completely removed by performing a conservation of momentum between the central and forward systems. Both the diphoton system and the two proton system allow for the mass and rapidity of the produced photons to be reconstructed. The "missing" mass and rapidity of the diphoton system can be calculated from the ξ measurement of both protons such that

$$m_{pp} = \overline{s\xi_1\xi_2} \qquad y_{pp} = \frac{1}{2}\log\frac{\xi_1}{\xi_2} \,. \tag{1.5}$$

By requiring that these mass and rapidity variables match with the mass and rapidity of the diphoton system (within the detector resolutions), one can be sure that the measured protons are coming from the same vertex as the diphoton and not a pileup vertex.

Selection cut	Signal	Exclusive	DPE	DY dijet + PU	$\gamma\gamma$ + PU
$[0.015 < \xi_{1,2} < 0.15$ $p_{T\ 1,(2)} > 200, (100)$ GeV]	65	0.13	0.2	1.6	2968
$m_{\gamma\gamma} > 600$ GeV	64	0.10	0	0.2	1023
$[p_T^2/p_T^1 > 0.95$ $\lvert\Delta\phi\rvert > \pi - 0.01]$	64	0.10	0	0	80.2
$\sqrt{\xi_1 \xi_2 s}$=$m_{\gamma\gamma}$±3%	61	0.09	0	0	2.8
$\lvert y_{\gamma\gamma} - y_{pp}\rvert < 0.03$	60	0.09	0	0	0

Table 1.1: Number of signal and background events after various selection requirements for an integrated luminosity of 300 fb^{-1} at $\sqrt{s}$ = 14 TeV. The signal is fixed with parameters S=1, $\mathcal{Q}_{\text{eff}}$ = 4, m = 340 GeV. At least one converted photon is required. Table is adapted from Reference [22].

The diphoton mass spectrum for the various signal and backgrounds can be seen in Figure 1.7. The power of the matching technique can be seen in Figure 1.8.

1.4 Axion-like particles

Another mechanism by which the anomalous scattering of LbL could be produced by any resonance such as the production of an axion-like particle (ALP) – a light pseudoscalar particle having a coupling to electromagnetism. A Feynman diagram of this process is shown in Figure 1.9. These particles could explain the CP symmetry in QCD [24] or give evidence for one of the components of dark matter [25]. ALPs also arise in many BSM theories such as string theory [26], warped extra-dimensions [20], and composite Higgs [19].

A new spin-0 particle would have couplings to SM fermions in proportion to the fermion mass. Therefore, in the high energy regime (above the top mass), the dominant coupling is to gauge bosons or the Higgs boson. The coupling to photons has been studied, and the ability to probe ALP production at the LHC has been demonstrated [23].

The interaction of the (pseudo) scalar particle with photons in the case of a CP-even or CP-odd scalar can be described by an effective Lagrangian as

$$\mathcal{L}^{+}_{\text{eff}} = \frac{1}{2f^2 m_a^2} F_{\mu\nu}F^{\mu\nu\ 2}(CP-even), \qquad \mathcal{L}^{-}_{\text{eff}} = \frac{1}{2f^2 m_a^2} F_{\mu\nu}\tilde{F}^{\mu\nu\ 2}(CP-odd) \tag{1.6}$$

where f^{-1} is the coupling strength, m_a is the mass of the (pseudo) scalar, and $\tilde{F}^{\mu\nu} = \frac{1}{2}\epsilon^{\mu\nu\rho\sigma}F_{\rho\sigma}$.

The proposed search method follows that of References [22, 27, 28]. The considered luminosity is 300 fb^{-1} at $\sqrt{s}$ = 13 TeV with an average pileup of μ = 50. The selection criteria requests the leading (subleading) photon to have $p_T > 200$ (100) GeV, for the azimuthal separation of the photons to satisfy $\lvert\Delta\phi^{\gamma\gamma} - \pi\rvert < 0.01$, and the p_T ratio to

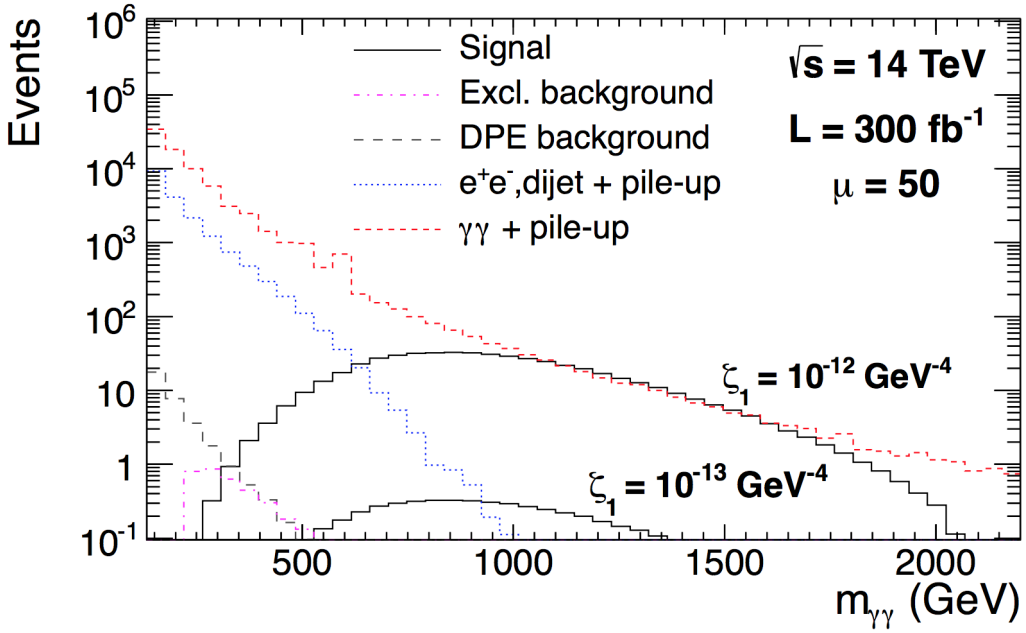

Figure 1.7: Diphoton invariant mass distribution for two potential signals ($\zeta_1 = 10^{-12}$ and 10^{-13} GeV^{-4}) and various backgrounds that could give two photons in the central detector plus two intact protons in the forward regions. Events are chosen having $p_T >$ 200 (100) for the leading (subleading) photon. The integrated luminosity considered is 200 fb^{-1}, and the average number of simulated interactions per bunch crossing is 50. Excl. stands for exclusive backgrounds and DPE stands for double pomeron exchange background. Figure extracted from Reference [22].

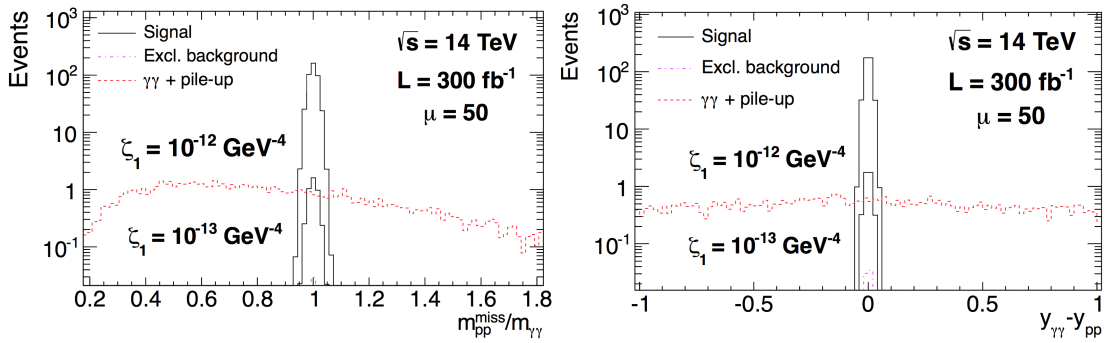

Figure 1.8: Diphoton mass to diproton missing mass ration (left) and rapidity difference (right). The distributions are shown for two potential signal values ($\zeta_1 = 10^{-12}$ and 10^{-13} GeV^{-4}) as well as the exclusive background and dominant inclusive $\gamma\gamma$ + pileup background. The integrated luminosity considered is 300 fb^{-1}, and the average number of pileup interactions is 50. Figure extracted from Reference [22].

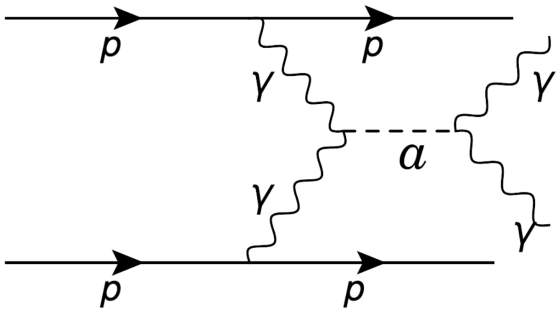

Figure 1.9: A diagram of exclusive diphoton production via the s-channel exchange of an axion-like particle. Figure extracted from Reference [23].

be $p_{T_2}^{\gamma}/p_{T_1}^{\gamma} > 0.95$. The system is then required to have a corresponding matching in mass and rapidity between the central diphoton and forward diproton where the diproton quantities can be calculated following Equation 1.5. This sequential selection criteria, shown in Table 1.2, removes virtually all background from the signal region.

Selection cut	**Signal**	**Exclusive**	**DPE**	e^+e^- **/ dijet + PU**	$\gamma\gamma$ **+ PU**
$[0.015 < \xi_{1,2} < 0.15$ $p_{T\ 1,(2)} > 200, (100)$ GeV$]$	23.1	0.1	0.1	1.2	1246
$m_{\gamma\gamma} > 600$ GeV	23.1	0.06	0	0.1	440
$[p_T^2/p_T^1 > 0.95$ $\lvert\Delta\phi\rvert > \pi - 0.01]$	23.1	0.06	0	0	35
$\lvert m_{pp}/m_{\gamma\gamma}$ - 1 $\rvert$	21.8	0.06	0	0	1.2
$\lvert y_{\gamma\gamma} - y_{pp} \rvert < 0.03$	21	0.06	0	0	0.2

Table 1.2: Number of signal and background events after applying the sequential selection cuts. The signal is chosen to have the parameters $m_a = 1200$ GeV and $f^{-1} = 0.1$ TeV^{-1}. The simulation is performed for an integrated luminosity of 300 fb^{-1} at $\sqrt{s} = 13$ TeV for 50 average pileup vertices. Table is adapted from Reference [23].

The effect of the matching criteria can clearly be seen in the distributions in Figure 1.10.

ALPs have been strongly constrained by many experiments [29] – some dedicated experiments and other general searches. A number of model-independent searches give rise to limits in the plane of the ALP mass versus the coupling strength. For example, the recent evidence for LbL scattering in HI collisions in CMS provides limits on ALP production [11].

However, at higher masses, there is an unexplored region of phase space that is now reachable in pp collisions at the LHC with intact protons. The potential reach of the search detailed above could explore mass ranges and coupling strengths that have been unattainable by previous experiments as shown in Figure 1.11 assuming a branching ratio of the ALP to two photons of $\mathcal{B}(a \to \gamma\gamma) = 1$ for 300 fb^{-1} of data.

In light of the aforementioned phenomenological studies, Chapters 3 and 4 will discuss the analyses that have been developed to search for 4γ anomalous couplings and ALP production using over 100 fb^{-1} of data collected at the LHC.

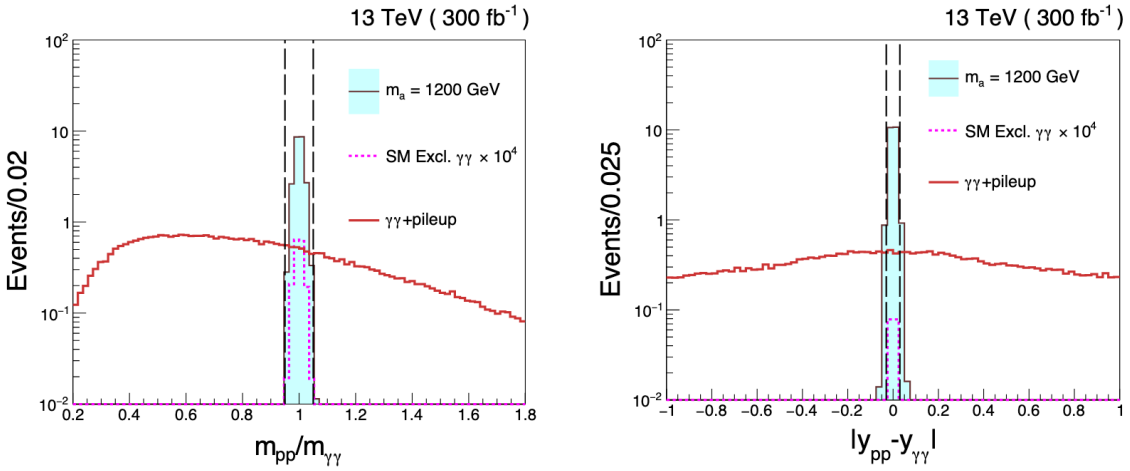

Figure 1.10: Ratio of the reconstructed diphoton mass to the missing diproton mass (left) and the difference of the reconstructed diphoton and diproton rapidities (right) for signal, exclusive diphoton, and $\gamma\gamma$ + pileup events. The signal is chosen to have the parameters m_a = 1200 GeV and f^{-1} = 0.1 TeV^{-1}. The integrated luminosity is 300 fb^{-1}, and the average pileup is 50. Figure is extracted from Reference [23].

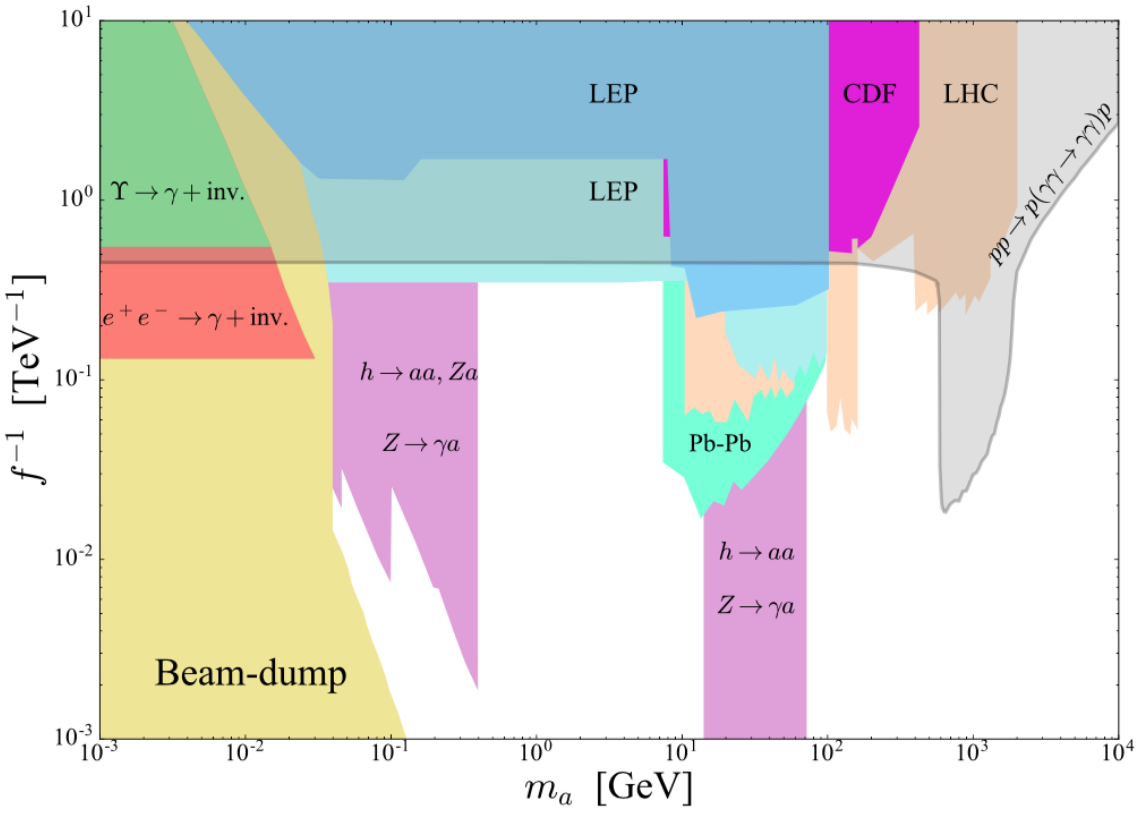

Figure 1.11: Exclusion regions for ALPs in the plane of the coupling (f^{-1}) and the mass (m_a). The colored regions show where the existence of ALPs has already been excluded, and the shaded region shows the expected 95% CL exclusion limit of the study detailed in the text. The expected limits assume $\mathcal{B}(a \to \gamma\gamma) = 1$ for 300 fb^{-1} of data. Figure extracted from Reference [23] and based on Reference [29].

Chapter 2: Experimental Setup

Contents

This chapter will discuss the LHC machine, the CMS experiment along with the relevant subdetectors, and Precision Proton Spectrometer (PPS).

2.1 The Large Hadron Collider

The Large Hadron Collider (LHC) is the largest and most powerful particle accelerator in the world. The machinery is 26.7 km in circumference and is located 175 m underground near the French-Swiss border at the European Organization for Nuclear Research (CERN). One of the main goals of the LHC was to discover the Higgs boson, which occurred in 2012 [30, 31]. Since that time, the main focus has shifted to searching for BSM physics. The LHC began operation in November of 2009 until early 2013 – the period known as Run 1. After a period known as Long Shutdown 1 (LS1), the LHC produced more data between 2015 and 2018, the period known as Run 2. At the current time, the LHC is in the Long Shutdown 2 (LS2) period before collecting more data in Run 3.

For the majority of the running periods, protons are collided at extremely high energies at various points around the LHC ring every 25 ns. The protons are taken from ionizing hydrogen gas inside a strong electric field. These protons are then accelerated in stages. The first stage of acceleration is performed by the linear accelerator, LINAC2 [32]. Here, protons are accelerated to one-third the speed of light (c) before being injected into the Proton Synchrotron Booster (PSB) [33]. The PSB is 157 m in circumference and accelerates the protons to 0.916 c. The last stage before entering the LHC is the Super Proton Synchrotron (SPS) [34] where the protons are increased to 0.999c. Finally, the protons are injected into the LHC beam line in packets and evenly divided between the two accelerators – one traveling clockwise and the other traveling counterclockwise.

Inside the LHC, protons are accelerated using Radiofrequecy (RF) cavities – a metallic chamber that contains an electromagnetic field [35]. The electric field inside the cavities is designed to oscillate at 400 MHz which is the exact frequency of proton bunches entering the cavity. It takes about 20 minutes of acceleration time for the protons to reach their final energy of 6.5 TeV before colliding at various points around the LHC.

In accelerator physics, the rate of collisions is measured as the instantaneous luminosity ($\mathcal{L}$) defined as

$$\mathcal{L} = \frac{1}{\sigma}\frac{dN_{events}}{dt} \tag{2.1}$$

where σ is the cross-section, and $\frac{dN_{events}}{dt}$ is the rate of collisions produced per unit time. The machine luminosity is dependent on parameters related to the beam specifications and for a Gaussian beam distribution at a circular collider, the luminosity can be expressed as

$$\mathcal{L} = \frac{N_b^2 n_b f_{rev} \gamma}{4\pi\epsilon_n \beta^* F} \tag{2.2}$$

where N_b is the number of protons in a given bunch, n_b is the number of bunches in each beam, f_{rev} is the frequency of revolution per bunch, γ is the relativistic factor, ϵ_n is the normalized transverse beam emittance, β^* determines the incident angle of the beams, and F is a reduction factor from the non-zero crossing-angle at the collision point. The peak luminosity of the LHC was designed to be $\mathcal{L} = 10^{34}$ cm^{2} s^{-1}; however, in 2018, the peak luminosity was more than double this value.

There are four interaction points (IPs) around the LHC where bunches collide to be measured by major experiments. Two of the experiments are general purpose detectors – CMS and ATLAS. The other experiments are ALICE and LHCb, designed to study heavy-ion physics and b-physics, respectively. The relative location of the IPs, and thus, the experiments, can be seen in Figure 2.1.

2.2 The CMS detector

The central feature of the CMS detector is a superconducting solenoid with a 6 m internal diameter, creating a magnetic field of 3.8 T. Within the solenoid volume sit a silicon pixel and strip tracker, a lead tungstate crystal electromagnetic calorimeter (ECAL), and a brass and scintillator hadron calorimeter (HCAL), each comprised of a barrel and two endcap portions. Forward calorimeters extend the pseudorapidity coverage provided by the barrel and endcap detectors. Muons are detected in gas-ionization chambers located in the steel flux-return yoke outside the solenoid. The various layers of the CMS detector are depicted in Figure 2.2. More details about each subdetector are provided later in the chapter.

Events of interest are selected using a two-tiered trigger system. The first level (L1), comprised of custom hardware processors, uses information collected by the calorimeters and muon detectors to select events at a rate of about 100 kHz within a latency of 4 μs [37]. The second level of the trigger system, known as the high-level trigger (HLT), uses a farm of processors running a version of the full event reconstruction software that is

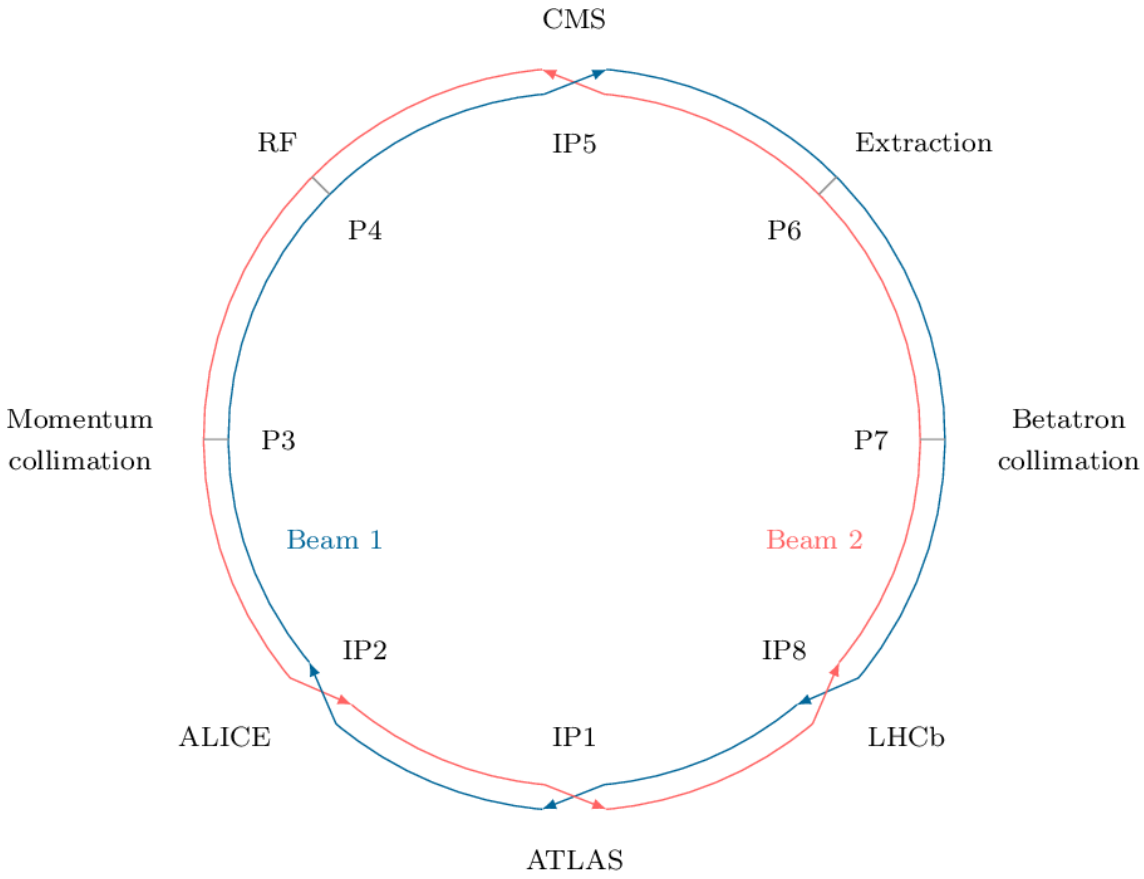

Figure 2.1: A schematic of the LHC with the relative placements of the interaction points and the major experiments.

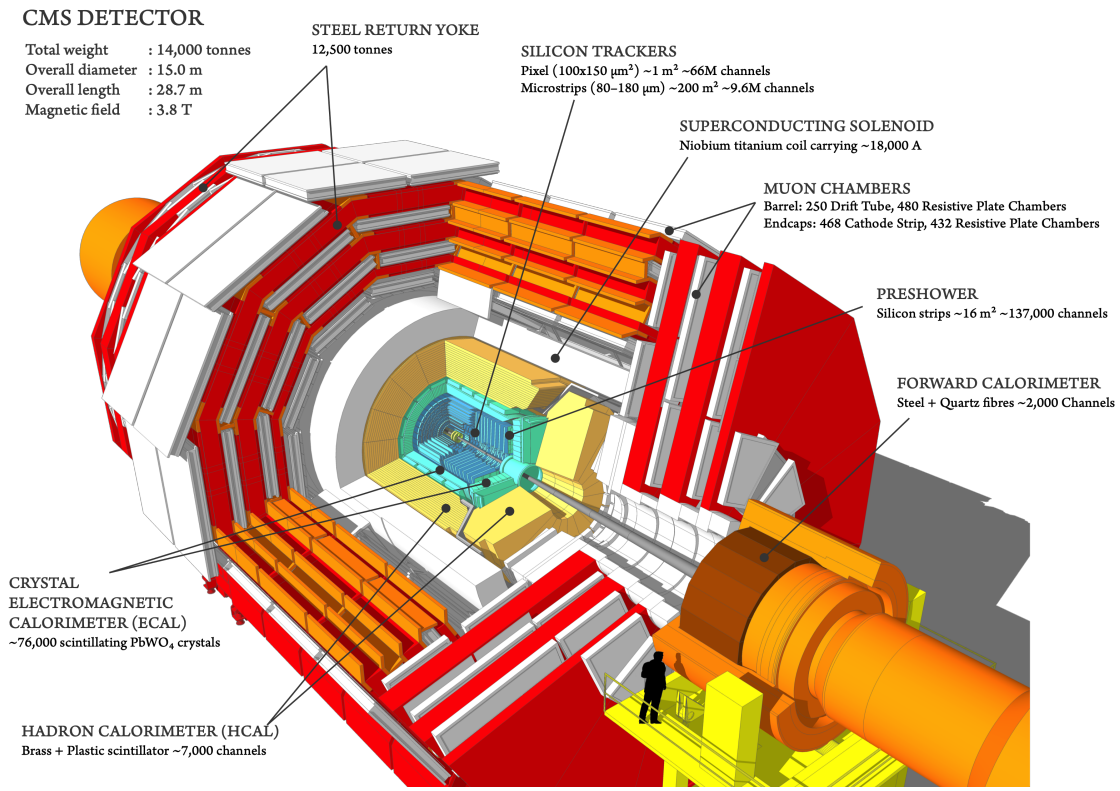

Figure 2.2: The CMS detector labeled with the various layered subdetectors. A human is added to show the relative size of the detector. Figure extracted from Reference [36].

optimized for efficient processing, and reduces the event rate to about 1 kHz before the data is stored [38].

The integrated luminosities for the 2016, 2017, and 2018 data-taking periods are individually known with uncertainties in the range of 2.3–2.5% [39–41], while the total Run 2 (2016–2018) integrated luminosity is known with an uncertainty of 1.8%. The improvement in precision is caused by the (uncorrelated) time evolution of some systematic effects.

The global event reconstruction algorithm (also called particle-flow (PF) event reconstruction [42]) attempts to reconstruct and identify each individual particle in an event by utilizing a combination of all subdetector information. Correctly identifying the particle type (photon, electron, muon, charged hadron, neutral hadron) is crucial in determining the particle direction and energy. Photons (e.g. coming from π^0 decays or from electron bremsstrahlung) are identified from energy measurements in the ECAL that are not linked to the extrapolation of a charged particle track in the ECAL. Electrons (e.g. coming from photon conversions in the tracker material) are identified by a primary charged particle track and one or more energy clusters in the ECAL corresponding to the extrapolated track trajectory or to possible bremsstrahlung photons emitted through the tracker material. Muons (e.g. from B hadron semileptonic decays) are identified by hits in the central tracker that are consistent with either a single track or several hits in the muon system, and associated with calorimeter deposits that are compatible with the muon hypothesis. Charged hadrons are identified by charged particle tracks that are neither consistent with

electrons nor muons. Finally, neutral hadrons are identified by energy deposits in the HCAL that are not associated with any charged hadron trajectory, or having an excess of energy deposits in the ECAL and HCAL compared with the energy expected from charged hadrons. The candidate vertex with the largest value of summed physics-object p_T^2 is taken to be the primary pp interaction vertex for an event.

The energy reconstruction for the various classification of particles is calculated using the information from the CMS subdetectors. The energy of photons is determined by the measurements from the ECAL. The energy of electrons is obtained from a combination of the track momentum at the interaction vertex, the corresponding ECAL cluster energy, and the energy sum of all bremsstrahlung photons attached to the track. The energy of muons is determined from the corresponding track momentum. The energy of charged hadrons is obtained from a combination of the track momentum and the corresponding ECAL and HCAL energies, corrected for the response function of the calorimeters to hadronic showers. Finally, the energy of neutral hadrons is determined from the corresponding corrected ECAL and HCAL energies.

Jets are reconstructed offline from energy deposits in the calorimeters, clustered together using the anti-k_T algorithm [43, 44] utilizing a distance parameter of 0.4. The algorithm assigns the measurement of each calorimeter tower to a momentum value calculated from the energy in the tower and the location of the tower. The raw jet energy is computed from the sum of the tower energies, and the raw jet momentum is computed by the vectorial sum of the tower momenta. The reconstructed jet momentum is found to be within 5 to 10% of the true momentum in simulation over the entire p_T spectrum for the jet acceptance. Other pp interactions within the same bunch crossing (pileup) can create additional tracks and energy deposits in the calorimeters. This effect is taken into account and mitigated by discarding charged particles that are identified to have originated from pileup vertices. An offset correction is then applied to the remaining energy and track contributions. Corrections to the jet energy are derived using simulation to correct the measured response of the jets to that of the average particle level jets. In situ measurements of the momentum balance in dijet, γ + jet, Z + jet, and multijet events are used to correct for residual differences between the jet energy scale of data and simulation [45]. The resolution on the jet energy is about 15–20% at 30 GeV, 10% at 100 GeV, and 5% at 1 TeV [45].

The missing transverse momentum vector, $\vec{p}_T^{\,\text{miss}}$, is calculated as the negative vectorial sum of the p_T of all PF candidates in the event and is corrected for the energy scale of reconstructed jets in the same event.

A transverse slice of CMS is shown in Figure 2.3, as well as the path of various particles through the subdetectors. CMS uses a coordinate system with the origin centered at the nominal collision point inside the detector, the y-axis pointing vertically upward, the x-axis pointing horizontally inward toward the center of the LHC ring, and the z-axis pointing along the beam direction from the LHC Point 5 towards the Jura mountains. The azimuthal angle (φ) is measured from the x-axis in the x-y plane and the polar angle (∂) is measured from the z-axis. Pseudorapidity is defined as η = -ln tan(∂/2). A more detailed description of the CMS detector can be found in Ref. [46].

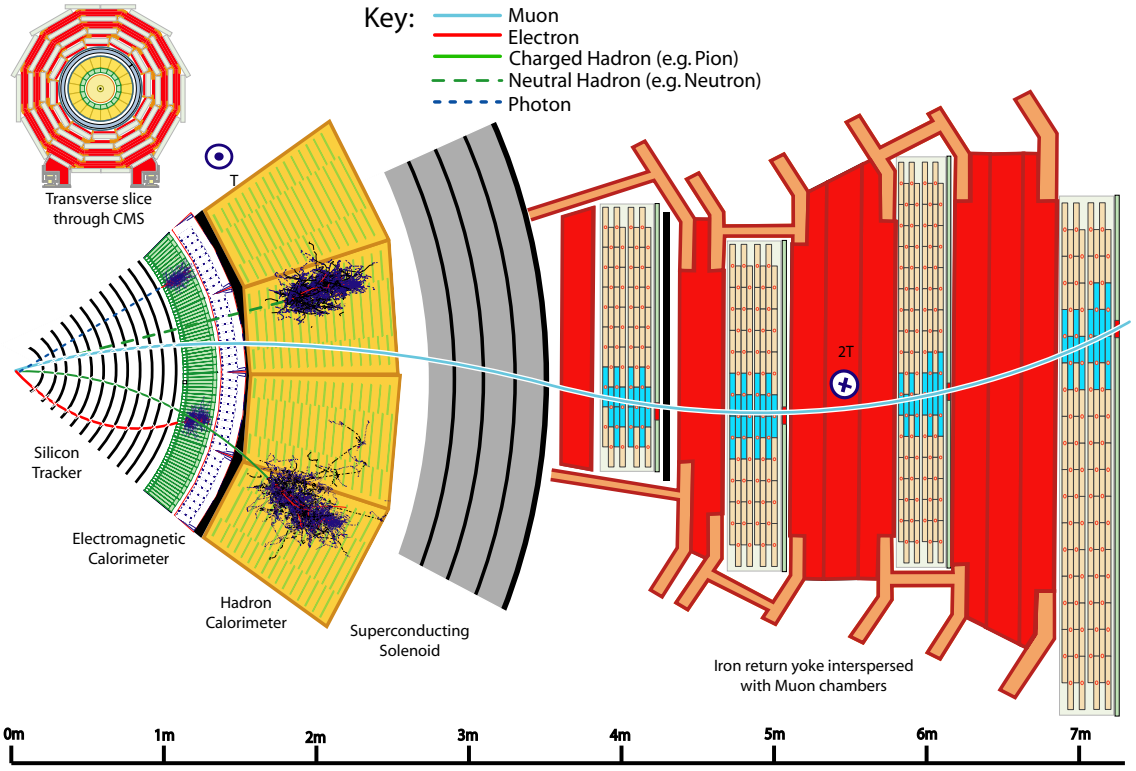

Figure 2.3: A schematic of the particle interactions for muons, electrons, charged and neutral hadrons, and photons in a transverse slice of the CMS detector. From left to right is depicted the interaction point, the tracker, the ECAL, the HCAL, the solenoid and the muon chambers.

2.2.1 Tracker

The CMS tracker employs silicon strip and pixel technology to measure the tracks of charged particles. Between the 2016 and 2017 data-taking periods, the original pixel detector was upgraded to maintain efficient tracking within the the environment of increased luminosity created by the accelerator upgrades during LS1. The original pixel detector consisted of three layers at radii of 4.4, 7.3, and 10.2 cm and two endcap disks on either side located 345 and 465 mm from the IP. For nonisolated particles within the p_T range of 1–10 GeVand $|\eta| < 1.4$, the track resolutions are typically 1.5% in p_T and 25–90 (45–150) μm in the transverse (longitudinal) impact parameter [47].

The upgraded detector, referred to as the CMS Phase-1 pixel detector, improves the performance for higher rate capability, radiation resistance, and more robust tracking [48]. The CMS Phase-1 pixel detector consists of four layers (L1-L4) at radii of 29, 68, 109, and 160 mm and three endcap disks (D1-D3) on either side located 291, 396, and 516 mm from the IP. For nonisolated particles within the p_T range of 1–10 GeVand $|\eta| < 3.0$, the track resolutions are typically 1.5% in p_T and 20–75 μm in the transverse impact parameter [49]. The layout of the original pixel detector is compared to the CMS Phase-1 pixel detector in Figure 2.4.

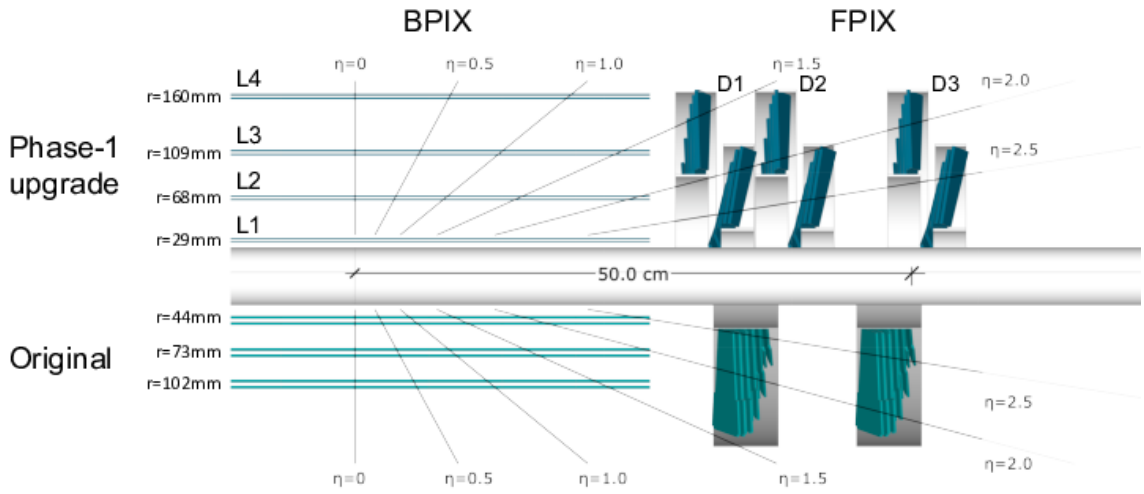

Figure 2.4: A longitudinal view comparing the layout of the original pixel detector with the CMS Phase-1 pixel detector. Figure extracted from Reference [48].

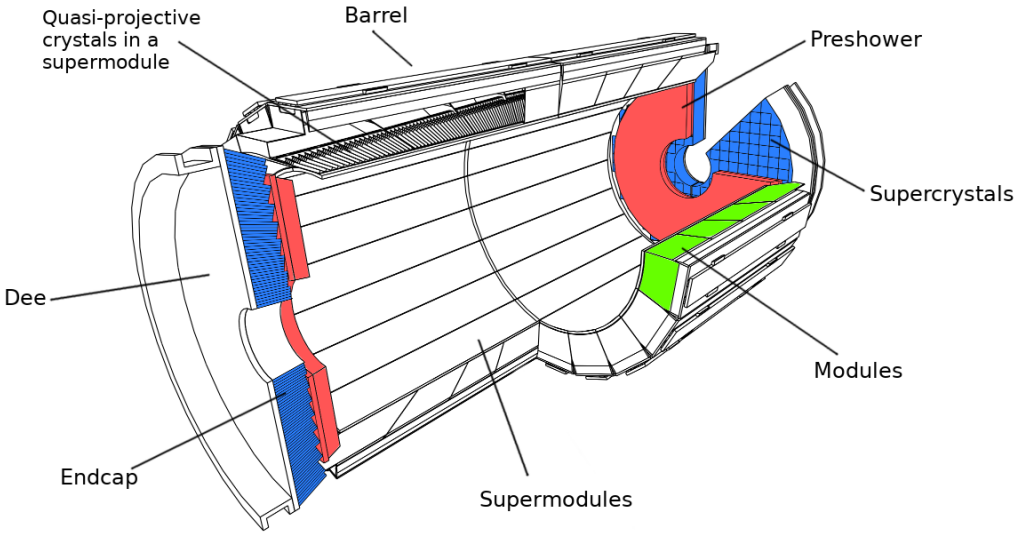

Figure 2.5: A schematic of the CMS ECAL showing the location of the barrel, endcap, and preshower subdetectors. Figure is extracted from Reference [51].

2.2.2 ECAL

The electromagnetic calorimeter consists of 75 848 lead tungstate ($PbWO_4$) crystals, which provide coverage in pseudorapidity $|\eta| < 1.48$ in a barrel region (EB) and $1.48 < |\eta| < 3.0$ in two endcap regions (EE). $PbWO_4$ was chosen because of its radiation hardness, its fast response time, and its small radiation length ($X_0 = 0.89\,\text{cm}$) [50]. Each crystal in the barrel is 23 cm long while the endcap crystals are 22 cm long. The crystals in the ECAL barrel are oriented so that the center of each crystal makes a 3^o angle with respect to the vector pointing to the IP. The purpose of this small angle is to avoid openings in the calorimeter aligned with incident particle trajectories. The barrel and endcap crystals have a $2.2 \times 2.2\,\text{cm}^2$ and $2.86 \times 2.86\,\text{cm}^2$ cross-section, respectively, corresponding to the average shower size of a photon in $PbWO_4$. The disadvantage of $PBWO_4$ is the low light yield, requiring the use of photodetectors for amplification. Avalanche photodiodes (APDs) with an amplification of 50 and vacuum phototriodes (VPTs) with an amplification of 10 are used as photodetectors in the barrel and endcap, respectively. After the signal is amplified by the photodetectors, it is passed into the front-end electronics where the information is digitized by an analog-to-digital converter (ADC), creating discrete amplitude measurements. These measurements sit in a buffer until the L1 trigger is activated at which point the 10 measurements from the selected event are passed into the CMS data stream. Knowledge of the pulse shapes of each electronic channel allows the signal amplitude (A) to be reconstructed offline.

Preshower detectors (ES) consisting of two planes of silicon sensors interleaved with a total of $3X_0$ of lead are located in front of each EE detector ($1.6 < |\eta| < 2.5$). The various components of the CMS ECAL can be seen in the schematic in Figure 2.5.

The energy resolution of the ECAL is defined as

$$\left(\frac{\sigma}{E}\right)^2 = \left(\frac{S}{\sqrt{E}}\right)^2 + \left(\frac{N}{E}\right)^2 + C^2 \qquad 2.3$$

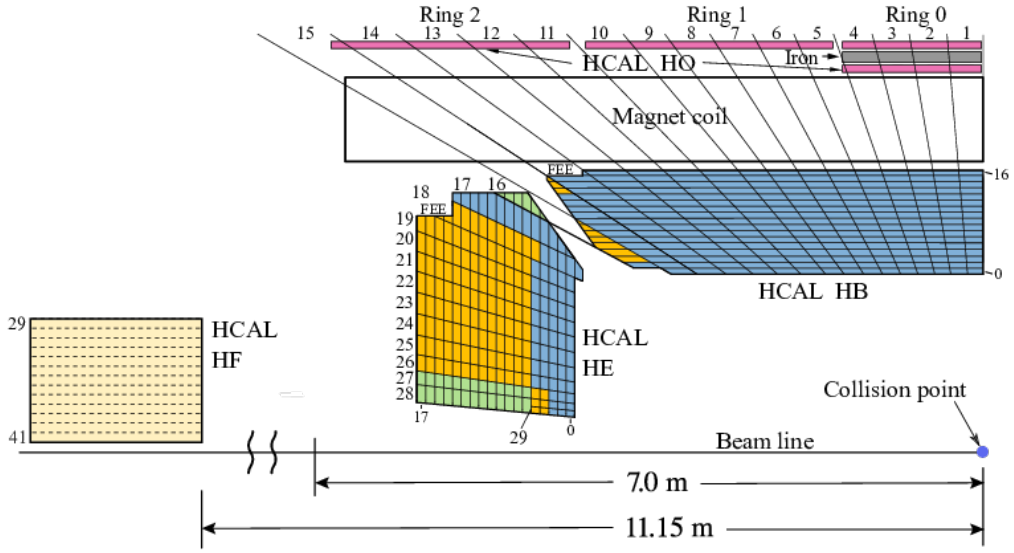

Figure 2.6: A quarter slice of the CMS HCAL in the r-z plane. FEE denotes the location of the front-end electronics. The colors represent different layers of detector that form different depth segments. HCAL segmentation in ϕ is not depicted. Figure extracted from Reference [54].

where S is the stochastic term, N is the noise contribution, and C is the scaling constant [52]. The contributions to S are event-by-event fluctuations in the shower containment, the energy resolution in the preshower, and the photostatistics in the photodetectors.

In the barrel section of the ECAL, an energy resolution of about 1% is achieved for unconverted or late-converting photons that have energies in the range of tens of GeV. The remaining barrel photons have a resolution of about 1.3% up to a pseudorapidity of $|\eta| = 1$, rising to about 2.5% at $|\eta| = 1.4$. In the endcaps, the resolution of unconverted or late-converting photons is about 2.5%, while the remaining endcap photons have a resolution between 3 and 4% [53].

2.2.3 HCAL

HCAL cells have widths of 0.087 in both pseudorapidity (η) and azimuth (ϕ) within the region of $|\eta| < 1.74$. In the η-ϕ plane, and within the region of $|\eta| < 1.48$, the HCAL cells map on to the 5×5 arrays of ECAL crystals to form calorimeter towers projecting radially outwards from the center of the detector. Within each of these tower, the sum of the energy deposits in the ECAL and HCAL is used to define the calorimeter tower energies, which are then used to derive the energies and directions of hadronic jets. When combining information from the entire detector, the jet energy resolution amounts typically to 15–20% at 30GeV, 10% at 100 GeV, and 5% at 1 TeV [45]. A schematic of the HCAL is shown in Figure 2.6.

2.3 The CMS Precision Proton Spectrometer

The CMS Precision Proton Spectrometer (PPS) is one of the CMS subdetectors that evolved out of a collaboration between the CMS and Total Elastic and Diffractive Cross-Section Measurement (TOTEM) experiments (previously named CT-PPS). The motivation for these detectors is to extend the CMS physics program to study central-exclusive production (CEP) processes in high-luminosity environments at the LHC both in the context of SM physics and BSM physics. The PPS detectors are located 210 and 220 m away from IP5 on either side of CMS as seen in Figure 2.7.

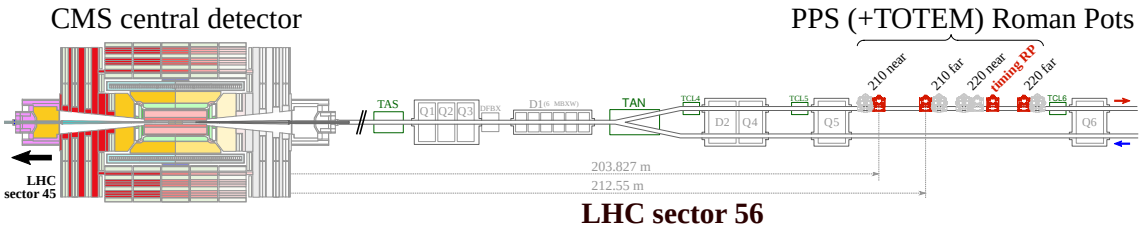

Figure 2.7: Layout of the PPS detectors with respect to CMS. One of the two symmetric sets of PPS detectors is shown. RPs are located at 210 and 220 m away from the IP with timing detectors located between the 220 m stations.

After a pp collision at IP5, if a proton remains intact in the final state, it will continue to travel down the LHC beam line, guided by the LHC magnets, until it interacts with the PPS detectors in the forward regions. The distance of the proton from the beam is proportional to the momentum loss of the proton, and in this way, the LHC magnetic lattice acts as a mass spectrometer for measuring protons. The PPS detectors located in the positive-z direction from CMS are referred to as sector-45 (for the area between IP4 and IP5), and the PPS detectors located in the negative-z direction from CMS are referred to as sector-56 (for the area between IP5 and IP6) as seen in Figure 2.8. At each of the 210 and 220 m stations, movable, near-beam machinery called Roman Pots (RPs) provide the housing for the proton tracking detectors. RPs were originally used at the ISR [55] before being employed at other colliders such as SPS, HERA, the Tevatron, and RHIC. Each PPS station is equipped with a horizontal RP that can move in the x-direction and a vertical RP that can move in the y-direction.

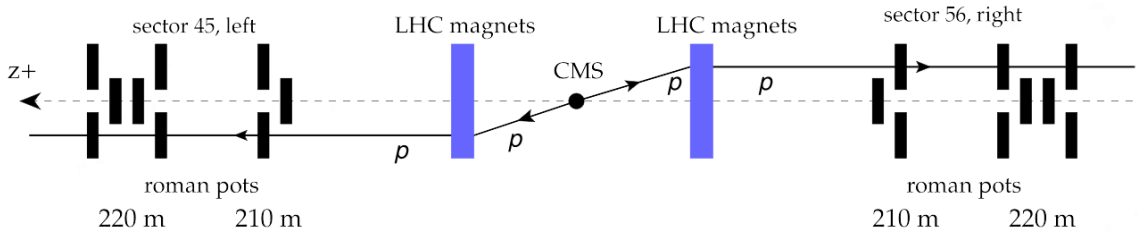

Figure 2.8: A schematic of the PPS detector system. After an interaction at the IP in CMS, protons travel through the LHC magnetic lattice until they reach the RP stations located on either side of CMS. The stations in the positive z-direction are referred to as sector-45 and the detectors in the negative z-direction are referred to as sector-56. Stations exist at both 210 and 220 m from the IP.

2.3.1 Tracking detectors

PPS used two different tracking technologies during the LHC Run 2. In 2016, silicon strip detectors were used in both the 210 and 220 m stations. The detector setup in this year was basically the same as what had been used previously by the TOTEM experiment in low-luminosity runs. There were two main goals of this exploratory operating period. The first goal was to prove the feasibility of operating a near-beam proton spectrometer at standard LHC luminosity conditions showing that the impedance of the detectors do not prevent the stability of the LHC beams and does not significantly affect the luminosity. The second goal was to fully integrate detectors into the CMS Data Acquisition (DAQ) system. Silicon strips were chosen following the design of the TOTEM detectors that had been used in previous years during low-luminosity runs at the LHC. The strips use a microchip edge-less technology built onto 300 μm of silicon substrate [56]. The purpose of minimizing the insensitive edge region is to maximize the acceptance for protons produced in coincidence with a central system of lower masses. Each station is equipped with 5 units each having 2 strip sensors with opposite orientations of $\pm 45^o$ with respect to the vertical axis. The strips obtain a 10 μm resolution in both the x and y planes. The lifetime for the strip sensors, because of radiation damage, is about 5×10^{14} proton/cm^2, so the sensors needed to be replaced periodically throughout the data taking process. The sensors use a VFAT2 ReadOut Chip (ROC) and were fully integrated into the CMS DAQ in 2016.

When multiple protons pass through strip detectors in a given bunch crossing, the ambiguities in the reconstruction algorithm from multiple hits in sensors of different orientations cause the event to be discarded. During the high-luminosity running conditions of the LHC, about 20% of events are expected to have multiple tracks in the PPS detectors. In 2017, 3D pixel sensors were introduced into the 220 m stations of PPS to enable multiple track reconstruction of the sensors and increase the radiation hardness. Then, in 2018, both the 210 and 220 m stations were equipped with 3D pixels. The reason that only the 220 m station was upgraded was to avoid the potential loss of data because of the commissioning time required for the newly installed stations. Each station consists of a stack of six detector planes where each plane uses a 1.6×2.4 cm^2 pixel sensor and six PSI46dig ROCs. The planes are tilted by 18.4^o to maximize the spatial resolution. Figure 2.9 shows the configuration of the tracking detectors by year.

2.3.2 Acceptance

The nominal acceptance of PPS is for protons having fractional momentum losses between 1.5% and 20%. Many beam, collimator, and detector effects can change this acceptance so it is important that these effects are monitored throughout the LHC running periods. The location of the RPs with respect to the IP also plays a large role in the acceptance. Figure 2.10 shows the simulated mass acceptance for PPS with two stations located 204 and 215 m away from the IP.

In the case where both protons are reconstructed, the acceptance can be understood

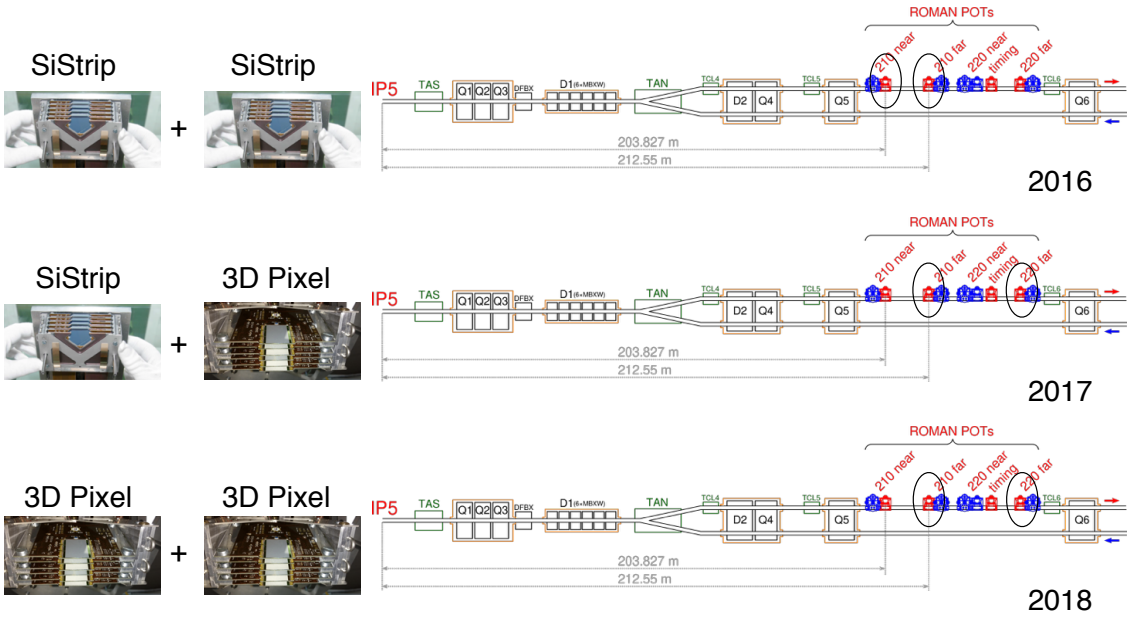

Figure 2.9: A schematic of the PPS detector configuration by year. The figure shows only one of the symmetric sides of the PPS detector stations. In 2016, silicon strip sensors were used in both the near and far stations. In 2017, silicon strips were used in the near stations while 3D pixel sensors were used in the far stations. In 2018, both stations were equipped with 3D pixel sensors.

as a function of the "missing mass" and rapidity of the protons calculated as

$$m_{pp} = \overline{s\xi_1\xi_2} \qquad y_{pp} = \frac{1}{2}\log\frac{\xi_1}{\xi_2} \tag{2.4}$$

where $\sqrt{s}$ is the center of mass energy.

Since these values conveniently correspond to the more familiar CMS variables of mass and rapidity, the PPS acceptance can be discussed in terms of the central system that could produce protons within the kinematic reach of the PPS detectors.

During the 2016 data taking period before Technical Stop 2, the acceptance as a function of the central system can be seen in Figure 2.11 for standard LHC optics. The figure shows that the single-arm acceptance region can probe lower masses and higher rapidities whereas the double-arm region is at higher masses (about 300 - 2000 GeV), and rapidities closer to zero.

2.3.3 Optics

By measuring proton tracks at the RP positions, it is possible to determine the proton kinematics at the IP by way of the beam optics, which provides a parametrization of the LHC magnetic lattice between the IP and the RPs. Figure 2.12 shows a schematic of a proton being transported non-linearly through the LHC to the RPs. The proton kinematics at the RP of a proton transported by the LHC magnetic lattice a distance s is given by

$$\vec{d}(s) = T(s,\xi)\cdot\vec{d}^{\,*} \tag{2.5}$$

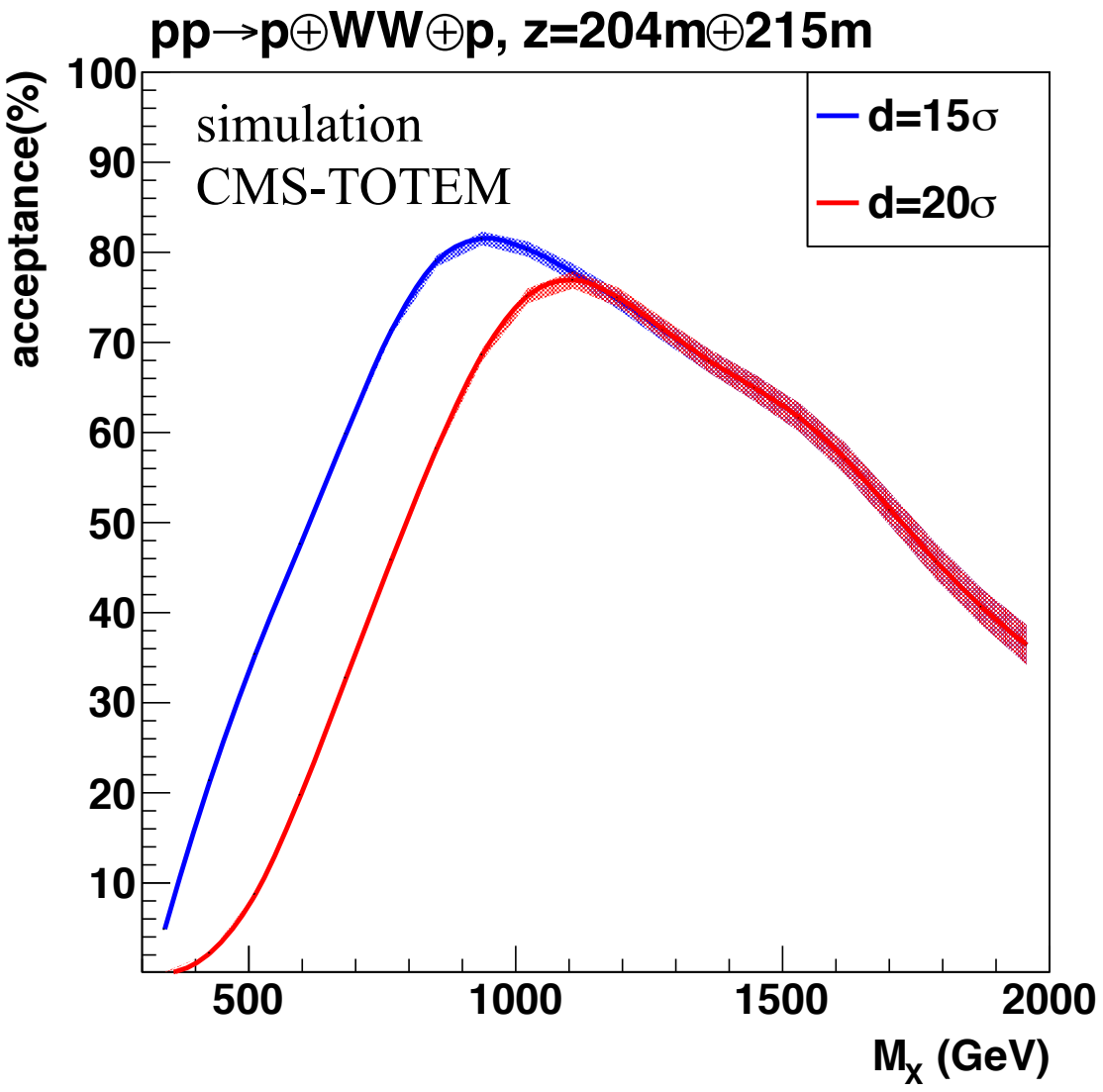

Figure 2.10: Acceptance for forward protons as a function of the centrally produced mass for exclusive WW events produced from photon-photon processes simulated with FPMC. In the simulation, tracking detectors are located at z=204 m and z=215 m. The blue (red) line shows the estimated acceptance when the detectors are inserted within 15 (20) standard deviations of the beamline. The shaded bands show the statistical uncertainty. Figure is extracted from Reference [57].

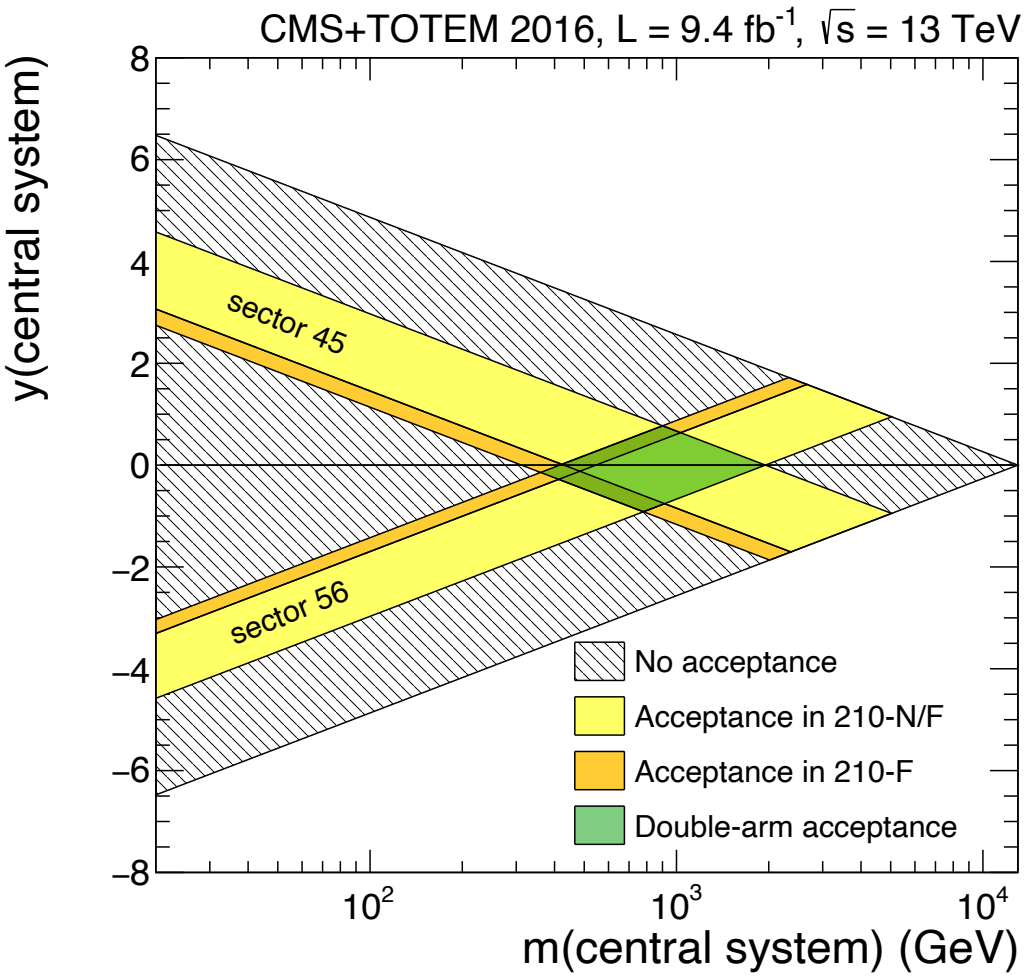

Figure 2.11: Acceptance of the PPS detectors in the 2016 pre-TS2 configuration in terms of the mass and rapidity of the central system. The yellow bands show the acceptance region for each of the PPS arms separately and the green region shows the acceptance for both arms.

where $\vec{d}$ is the proton kinematic vector at the RP,

$$\vec{d} = \begin{pmatrix} x & \partial_x & y & \partial_y & \xi \end{pmatrix}^T \tag{2.6}$$

$\vec{d}^*$ is the proton kinematic vector at the IP, and T(s, ξ) is the transportation matrix given in equation 2.7.

$$T = \begin{pmatrix} v_x & L_x & m_{13} & m_{14} & D_x \\ \frac{dv_x}{ds} & \frac{dL_x}{ds} & m_{23} & m_{24} & \frac{dD_x}{ds} \\ m_{31} & m_{32} & v_y & L_y & D_y \\ m_{41} & m_{42} & \frac{dv_y}{ds} & \frac{dL_y}{ds} & \frac{dD_y}{ds} \\ 0 & 0 & 0 & 0 & 1 \end{pmatrix} \tag{2.7}$$

In the transport matrix, L_x and L_y are the effective lengths in the x and y directions, D_x and D_y are the horizontal and vertical dispersions, respectively, and m_{ij} are the LHC magnetic coupling constants. The horizontal and vertical magnifications are given by

$$v_{x,y} = \sqrt{\beta_{x,y}/\beta^*} \cdot \cos \Delta\mu_{x,y} \tag{2.8}$$

where $\beta_{x,y}$ are the betatron amplitudes and the relative phase advance $\Delta\mu_{x,y}$ is given by

$$\Delta\mu_{x,y} = \int_{IP}^{RP} \frac{ds}{\beta_{x,y}} \tag{2.9}$$

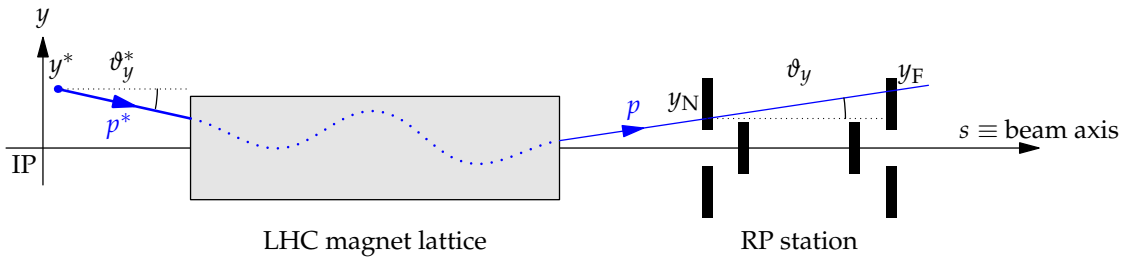

Figure 2.12: A schematic of the trajectory a proton could take from the IP through the LHC magnetic lattice (shaded rectangle) to reach the PPS RPs. An asterisk denotes the kinematics of the proton at the IP.

Keeping only the leading terms, the transportation equations used for proton reconstruction are

$$x = v_x(\xi) \cdot x^* + L_x(\xi) \cdot \partial_x^* + D_x(\xi) \cdot \xi \tag{2.10}$$

$$y = v_y(\xi) \cdot y^* + L_y(\xi) \cdot \partial_y^* + D_y(\xi) \cdot \xi \tag{2.11}$$

where an asterisk denotes the variables at the IP. Figure 2.13 shows the effects of the LHC optics on the proton position in the RPs in the x-y plane.

Analysis specific information about the optics determination will be discussed in a later portion of this thesis. More information about the use of the LHC optics can be found in Reference [58].

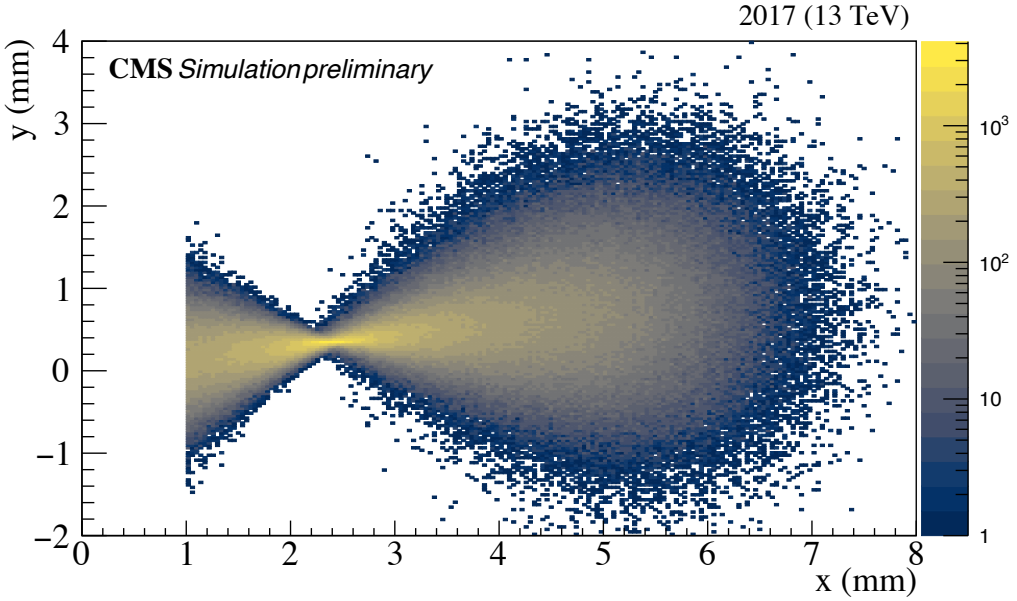

Figure 2.13: Simulation of protons propagated to the PPS detectors and their hits in the x-y plane. A depiction is shown of the focal point where x = x_0 and L_y = 0 (at about x=2.15 mm). This focal point is used to calculate the horizontal dispersion in the optics calibration for the proton reconstruction.

2.3.4 Alignment

The purpose of PPS is to measure the proton location with respect to the beam, and therefore, the alignment of the detectors with respect to the beam needs to be established. Alignment of the PPS detectors is performed first using data from low-luminosity runs where both the vertical and horizontal RPs are inserted very close to the beam (within 1 mm). The information of the relative alignment of the RPs is then used to correct the data at high-luminosity when the RPs are moved slightly further from the beam line. There are three steps to the alignment procedure. The first step is the beam-based alignment in which the RPs are calibrated with respect to the LHC collimators – the machinery used in the LHC to keep the particles confined inside the beam pipe. During low-luminosity runs, the RPs are slowly moved closer to the beam-line until contact with the beam is made noted by a loss in the beam-loss monitors. At this point, the RPs are at the same distance from the beam as the collimators, thus providing a starting point for the alignment. The second step takes advantage of the overlapping area between the vertical and horizontal RPs to align the RPs relative to one another. Using proton tracks that pass through multiple RPs allows to determine the relative alignment of all sensors within a given station as seen in Figure 2.14. The last step of the alignment process is the absolute alignment of the RPs with respect to the beam. A set of elastic-scattering events, tagged by the vertical RPs, is used to derive the position of the beam relative to the detectors using the azimuthal symmetry of the elastic process. Data taken during the high-luminosity runs is then corrected using the alignment data taken during the calibration runs. More information about the details of the alignment process can be found in Reference [59].

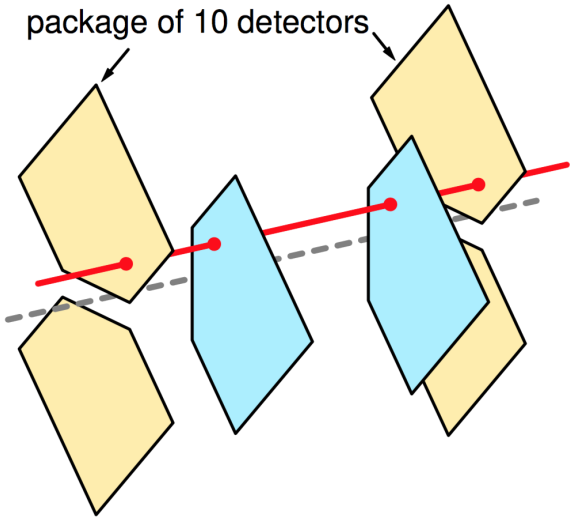

Figure 2.14: The red line represents a proton track passing through the overlapping region of both vertical and horizontal RPs. The dotted line represents the LHC beam line.

2.3.5 Physics validation

During the LHC Run 2 period, PPS collected over 110 fb^{-1} of data. The data recorded by the RPs relative the data recorded with CMS can be seen in Figure 2.15

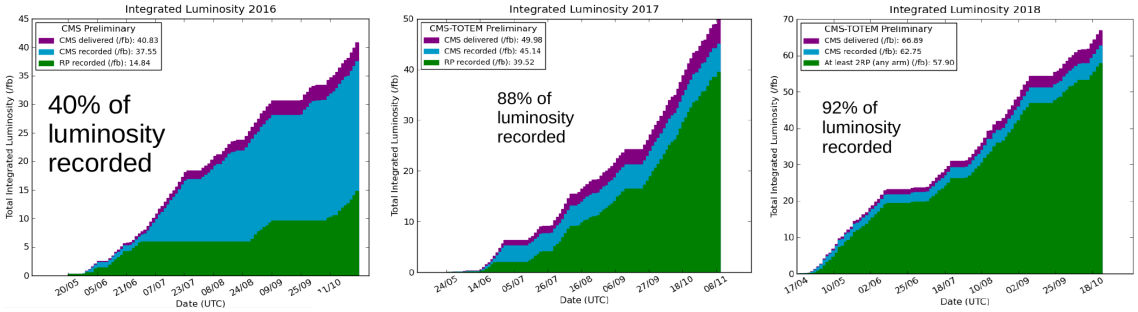

Figure 2.15: A comparison of the data recorded by the CMS detector (blue) and the PPS RPs (green). The left plot shows the comparison for 2016 data, the middle plot shows the comparison for 2017 data, and the right plot shows the comparison for 2018 data. This amount of luminosity is a great achievement for PPS, especially accounting for the luminosity efficiency in 2017 and 2018.

Using 9.4 fb^{-1} of data from 2016, the first validation of the PPS system came through the observation of the SM process $\gamma\gamma \to \ell\ell$ as shown in Figure 2.16.

The case in which both protons dissociate was treated as a background in this study. Candidates were selected with two opposite sign leptons passing a dedicated criteria while having at least one proton intact in the final state. The lepton criteria consisted of $p_T^{\ell} > 50\text{GeV}$ and $M_{\ell\ell} > 110\text{GeV}$ to avoid the peak of the Z boson. Additionally, events were selected based on the azimuthal separation of the leptons as well as the cleanliness of the dilepton vertex as seen in Figure 2.17.

Events were determined to be signal if they had a corresponding matching between

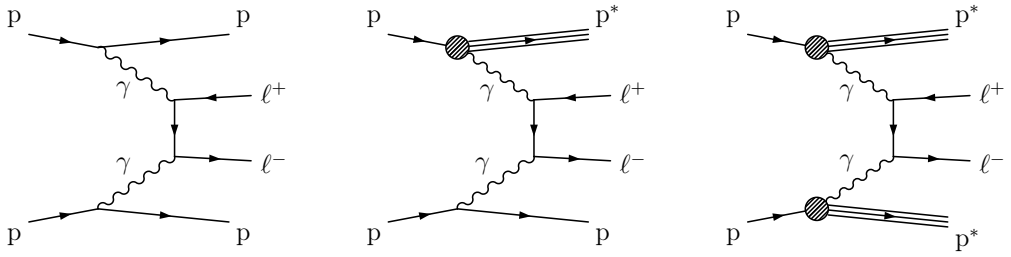

Figure 2.16: All three Feynman diagrams show the photoproduction of two opposite sign leptons. The leftmost diagram shows the case where both protons remain intact in the final state, the middle diagram shows the case where only one proton remains intact in the final state, and the rightmost diagram shows the case where both protons dissociate.

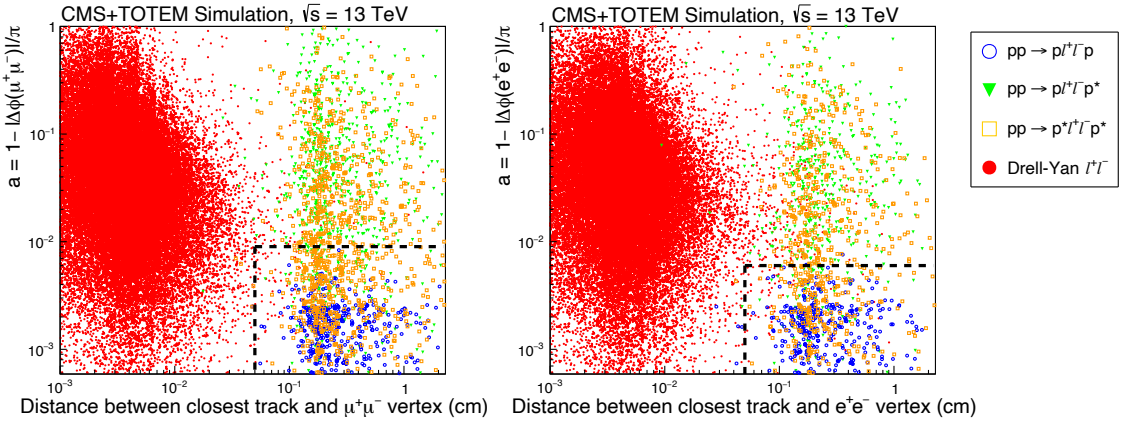

Figure 2.17: Acoplanarity versus the distance from the dilepton vertex to the closest track for the dimuon channel (left) and the dielectron channel (right). The red points represent the Drell-Yan process (background), the yellow double-dissociative $\gamma\gamma \to \ell\ell$ process (background), the green points represent the single-dissociative $\gamma\gamma \to \ell\ell$ process (signal), and the blue points represent the exclusive $\gamma\gamma \to \ell\ell$ process (signal). The figure is extracted from reference [60].

the reconstructed proton ξ and the dilepton $\xi^{\pm}_{\ell^+\ell^-}$ such that

$$\xi^{\pm}_{\ell^+\ell^-} = \frac{1}{\sqrt{s}} \sum_{i=1}^{2} p_T^{\ell_i} e^{\pm\eta_{\ell_i}} \qquad 2.12$$

In the end, 12 single dissociative events were observed in the dimuon channel and 8 single-dissociative events were observed in the dielectron channel over a background of 1.49 ± 0.07(statistical) ± 0.53(systematic) and 2.36 ± 0.09(statistical) ± 0.47(systematic), respectively. This signal yield corresponds to a significance greater than 5.1σ and the first observation of this process at the electroweak scale. The observed events can be seen in Figure 2.18 and more information can be found in Reference [60].

The observation of this "standard candle" process proves the feasibility of using the PPS alignment, optics, and proton reconstruction to conduct physics analysis in standard LHC luminosity conditions.

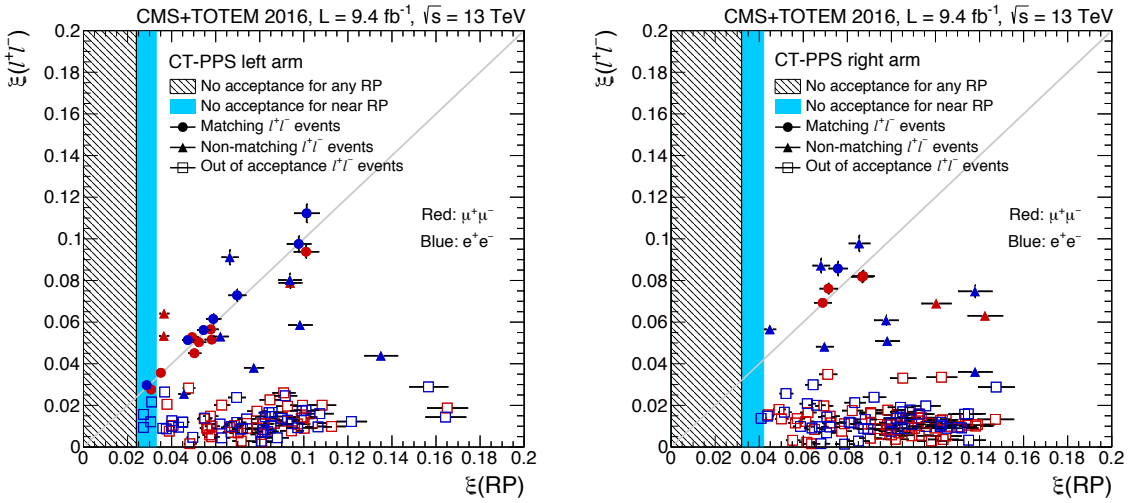

Figure 2.18: Correlation between the ξ value reconstructed from the leptons ($\xi(\ell^+\ell^-)$) and the ξ value reconstructed by the RPs (ξ(RP)). The left plot is for protons in sector45 and the right plot is for protons in sector56. The shaded region corresponds to the region outside the kinematic acceptance of both the near and far RPs. The horizontal error bars indicate the error on ξ(RP) and the vertical error bars indicate the error on $\xi(\ell^+\ell^-)$. The events labeled "out of acceptance" are events where $\xi(\ell^+\ell^-)$ is outside of the RP acceptance and a background proton is reconstructed with non-matching kinematics. The figure is extracted from reference [60].

Chapter 3: Search For Exclusive Diphoton Events With Data Collected In 2016

Contents

A search for central exclusive two-photon production of photon pairs is performed at a center-of-mass energy $\sqrt{s} = 13$ TeV using 9.4 fb^{-1} from the central CMS detector and the CMS-TOTEM Precision Proton Spectrometer [61]. The search targets photon exchange events producing two photons in the central detector with intact, outgoing protons in the final state. By searching in a high diphoton mass region, $m_{\gamma\gamma} > 350$ GeV, standard model diphoton production is suppressed and an anomalous coupling signal might remain. A very strong pileup background suppression is obtained by measuring intact protons in the forward regions. The background is dominated by inclusive diphoton production in coincidence with pileup protons. Events are selected with individual photon $p_T > 75$ GeV and at least one proton track measured in PPS on either side of CMS. With no exclusive candidates observed (and none expected) in the whole 2016 data-taking periods, an upper limit of 4.4 fb is set on the fiducial production cross-section for this process for

proton momentum losses $0.070 < \xi < 0.111$ (0.138) corresponding to the acceptance of the forward detectors on the positive-z and negative-z sides of CMS, respectively. The first collider limits are placed on four-photon anomalous quartic gauge couplings.

3.1 Samples

The samples described in this section include the LHC data from 2016, the simulated inclusive background MC samples, and the AQGC signal MC samples.

3.1.1 Data samples

Three data samples were used in this study, corresponding to the first datasets acquired with the PPS detectors inserted. A long gap was observed between runs C and G, corresponding to one and a half months where the radiation damage suffered by the strips detectors caused their collection efficiency to drop drastically. Thus, the commissioning of PPS timing detectors was prioritized with respect to the tracking component for this period. However, for the beginning of Run G, some efficiency was recovered by increasing the bias voltage of the sensors.

Additionally, a few of the first and last luminosity sections of each LHC stable fill, corresponding to the few minutes where the pots were being inserted or retracted to prevent any damage lead by beam instabilities, are dropped from the usable runs. This corresponds to a drop of 6.2 fb^{-1} from the 15.6 fb^{-1} recorded in CMS for the equivalent period. The three datasets can be seen in Table 3.1.

Era	**LHC run range**	$\mathcal{L}$ **(fb^{-1})**
Run B	273725–275376	4.29
Run C	275657–275931	1.44
Run G	279766–280385	3.63

Table 3.1: A list of the era, run range, and luminosity corresponding to the three data samples used for analysis.

To process the data samples we use `flashgg`, a framework developed for major CMS diphoton searches, and described in [62]. Originally designed for H$\to\gamma\gamma$ analyses, `flashgg` uses a multi-variate algorithm (MVA) to build diphoton candidates and diphoton vertices, which are normally very difficult to reconstruct.

3.1.2 Background samples

Various background processes are simulated that are believed to contribute to the selected data of this study. A complete list of all background samples used for the description of the selection regions is shown in Table 3.2. All samples are mixed with simulated pileup vertices to mimic the effect from the LHC collisions. The samples are then reweighted to the pileup distribution from the three data-taking eras.

Sample	σ_{gen} pb	Number of events
Incl. $\gamma\gamma$	134.3	3.9×10^6
Incl. γ	862.4	72.8×10^6
$Z\gamma$	123.8	14.4×10^6
$W\gamma$	378.2	6.1×10^6
$t\bar{t}$	511.3	10.2×10^6
QCD	113,100	20.8×10^6

Table 3.2: A list of the background samples used to describe the data as well as their generated cross-section and number of events.

The leading inclusive $\gamma\gamma$ background as well as the $W\gamma$ and $Z\gamma$ subleading backgrounds are simulated by MadGraph5_aMC@NLO 2.2.2 [63] at next-to-leading order (NLO) accuracy with NNPDF3.0 parton distribution functions (PDFs) at next-to-NLO accuracy [64]. The $W\gamma$ and $Z\gamma$ events act as a background in scenarios where the decay product (electron) is misidentified as a photon. Other subleading backgrounds, namely the photon-enriched QCD, photon-enriched inclusive γ, and inclusive $t\bar{t}$ processes, are generated at LO by Pythia 8.205 [65] with NNPDF3.0 PDFs at LO accuracy. The exclusive SM LbL and DPE $\gamma\gamma$ processes are negligible in this mass range for the luminosity used in this study. LbL events are simulated using the Forward Physics Monte Carlo (Fpmc) [66] using the process implemented by the authors in Reference [27]. Furthermore, all samples considered in this search are processed with a Geant4 [67] simulation of the CMS central detector.

3.1.3 Signal samples

Similarly to the SM LbL process, AQGC signal events are simulated with FPMC assuming collinear photon emission from the protons. The photon fluxes from protons are modeled using the Budnev et al. paramaterization [68].

The anomalous coupling signal is expected at high diphoton mass, high photon p_T, and to be centrally produced within the detector. Because of their exclusive nature, the signal boasts the characteristic of having back-to-back photons with respect to the angle ϕ. These characteristics can be seen in Figure 3.1.

As an extra cross-check, two additional LbL samples were simulated with SuperChic v2.06 [69], and fed to the same reconstruction and analysis frameworks. Two soft survival factors scenarios were used for these two samples: a constant 100% survival factor, and the so-called survival *model 4* described in [70]. A good agreement is observed between the different samples. The input PDFs for incoming photons are the collinear LUXqed 2017 sets [71], expected to reproduce with good accuracy the collinear, resolved and unresolved photon emission over a broad range of Q^2 and x_{Bj}.

3.2 Photon identification and isolation

Photons are reconstructed from energy deposits in the ECAL using algorithms that constrain the superclusters in η and ϕ to the shape that is expected for high p_T photons

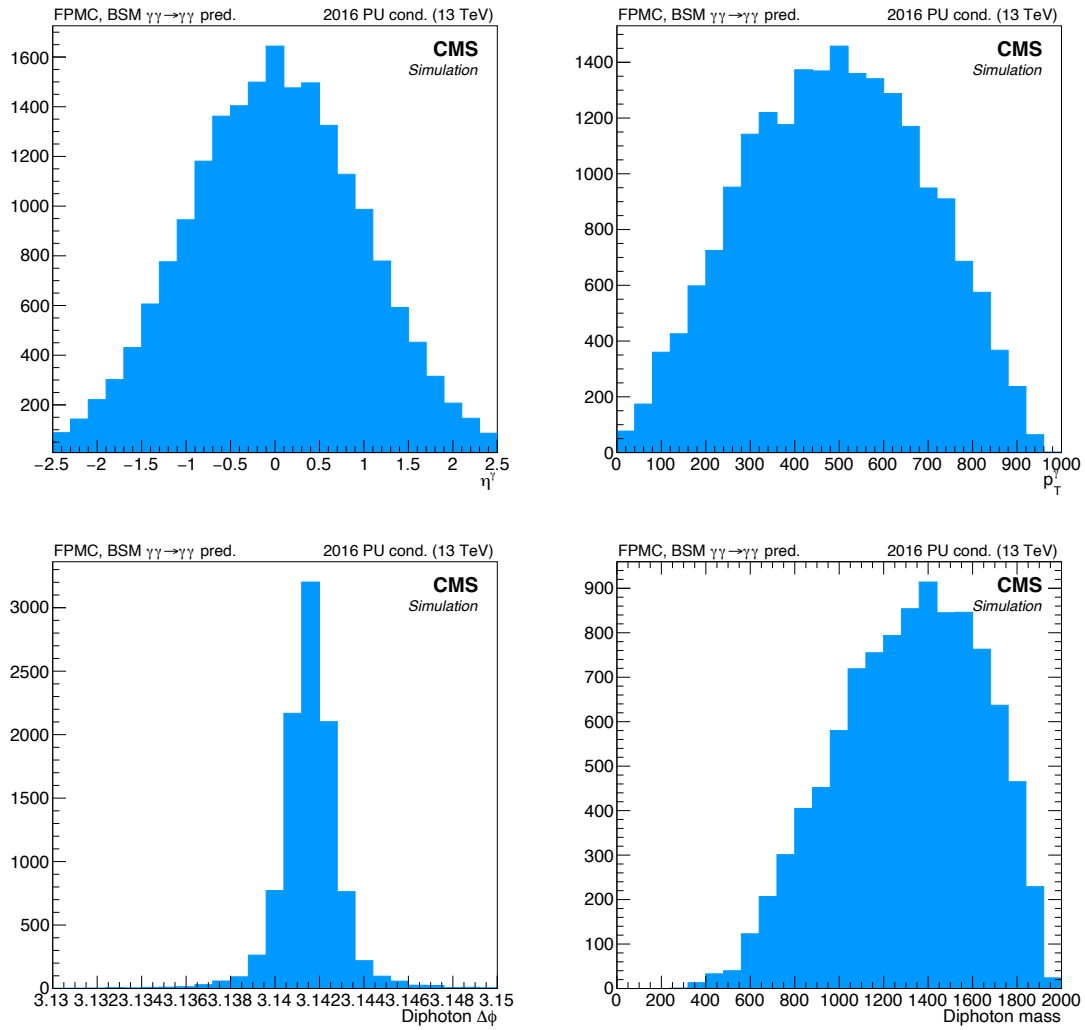

Figure 3.1: Kinematics coming from simulated anomalous coupling events with intact protons. These distributions are for the individual photons at generator level in FPMC and setting the coupling value, ζ_1, to 10^{-12} GeV^{-4}. On the top left is the photon η, on the top right is the photon p_T, on the bottom left is the diphoton $\Delta\phi$, and on the bottom right is the diphoton mass. The fractional momentum loss of the protons is imposed to be between 2 and 15% at generator level. The signal is shown to appear at high mass and central η.

and electrons. The algorithms do not use a hypothesis for the particle being a photon or electron, therefore, $Z \to e^+e^-$ events are typically used for measurements of the photon trigger and identification efficiencies [72]. However, an electron veto is applied later that rejects a photon candidate if its supercluster is matched to an electron track with no missing hits in the tracking layer. The fraction of events entering the four possible categories of the electron veto is shown in Figure 3.2.

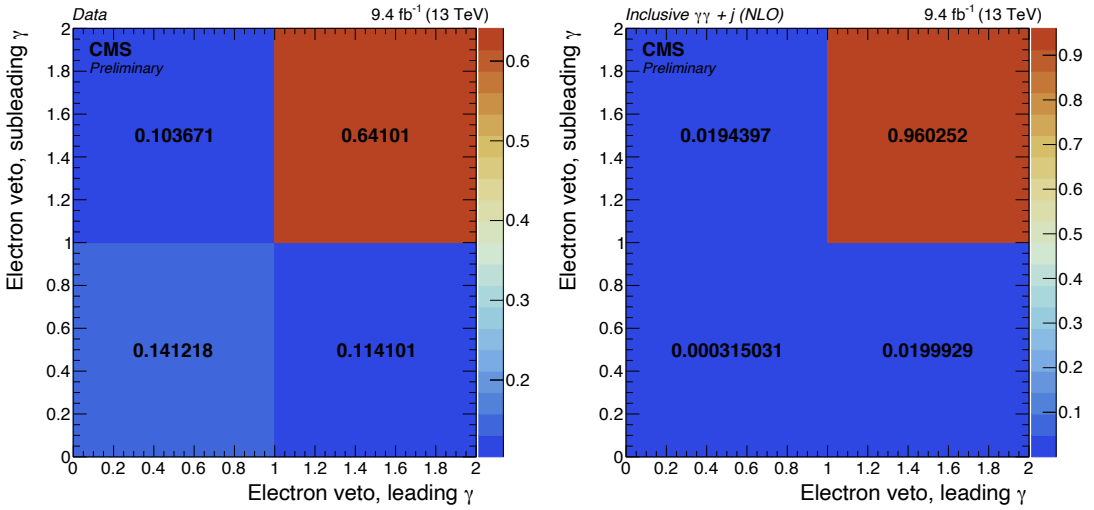

Figure 3.2: Fractional number of preselected diphoton events with $p_T(\text{single } \gamma) > 75$ GeV and $m_{\gamma\gamma} > 350$ GeV, and having both photons failing (bottom left bin), one photon failing (top left or bottom right bins), or both photons passing (top right bin) the conversion safe electron veto for the whole 2016 data (left) and dominant $\gamma\gamma + j$ background (right) samples.

We use the MVA-based photon ID from the Run II $H \to \gamma\gamma$ study detailed in Reference [73]. The ID uses isolation criteria based on the electromagnetic shower shape and activity around the shower to reduce the photon fake rate while maintaining a high signal efficiency. The shape of the shower in the ECAL is measured using the variable $i\sigma_{i\eta i\eta}$, which is the spatial second-order moment corresponding to the photon candidate in the η direction[72] and is defined as

$$\sigma_{i\eta i\eta} = \sqrt{\frac{\sum_{i\in 5\times5} w_i \left(\eta_i - \bar{\eta}\right)^2}{\sum_{i\in 5\times5} w_i}}, \qquad w_i = \max(0, 4.7 + \log(E_i/E_{5\times5})) \tag{3.1}$$

where η_i is the pseudorapidity in the i^{th} crystal, $\bar{\eta}$ is the average pseudorapidity of the 5×5 cluster, and w_i is the weighting term.

Photons can be further identified through the R_9 isolation variable. This R_9 quantity is defined as the ratio of energy deposited in the ECAL in a 3×3 cluster to the energy deposited in the 5×5 cluster encasing it, centered on the most energetic crystal. Photons that convert before reaching the ECAL will have showers with a larger spread leading to a lower R_9 value than unconverted photons. This kinematic variable also allows to veto poorly isolated photons, expected to increase the energy spread into a larger geometrical fraction of the calorimeter. Figure 3.3 shows the performance of the R_9 value in the barrel

for photons that convert in the tracker and photons that convert later or do not convert at all.

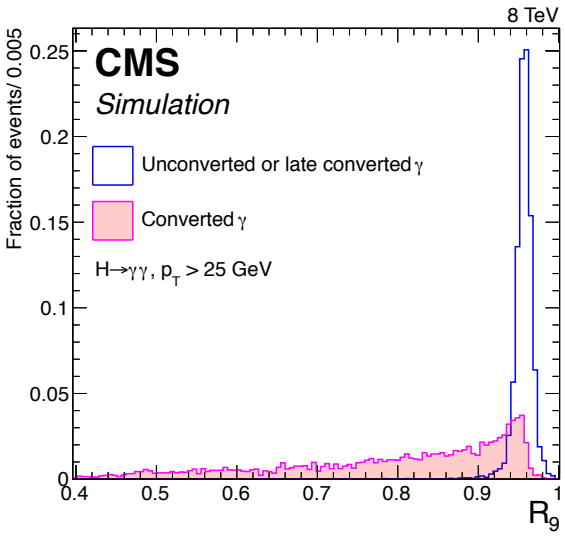

Figure 3.3: Distributions of the R_9 variable for photons in $H \to \gamma\gamma$ events. The distributions are shown for photons that convert in the tracker before a radius of 85 cm (red) and for photons that convert in the ECAL or not at all (blue). All photons are required to have a minimum p_T of 25 GeV. Figure extracted from Reference [72].

This is useful for identifying individual photons depositing their energy in the ECAL, which give a high R_9 value as opposed to π^0 decays that yield a much lower R_9 value as the two photons in the decay are separated by a very small distance. Additionally, a selection on the ratio of hadronic energy to electromagnetic energy (H/E) gives a further discrimination for photons. The overall efficiency for photon identification is shown to be about 90% for photons in the ECAL Barrel (EB) and about 87% for photons in the ECAL Endcap (EE). Photon identification criteria can be found in Table 3.3.

Photon Category	R_9	H/E	$\sigma_{i\eta i\eta}$
EB	≥ 0.94	< 0.082	< 0.014
EE	≥ 0.94	< 0.075	< 0.034

Table 3.3: The photon identification and selection criteria for high signal efficiency.

To obtain optimal energy resolution, calibrations and corrections are applied to the data for various detector effects. The ECAL crystal transparency is monitored and corrected for during each LHC run.

Along with other information described in [73] the Boosted Decision Tree (BDT) MVA is trained using

- p_T of both photons
- $\cos \Delta\phi_{\gamma\gamma}$
- vertices multiplicity in the event
- the BDT discriminant for the three best vertices taken from the vertex identification MVA

- the longitudinal distance Δz between the best vertex, and the second and third choices
- number of converted photons (either 0, 1, or 2)

To be inclusive of the signal, both photons are required to pass a loose selection on the ID MVA output score (> -0.9). Central scale factors provided by the CMS collaboration were used to correct the MC, where five bins of p_T and eight bins of supercluster $|\eta|$ are derived.

3.3 Selection

In this section, the event selection is discussed for the inclusive control region and the signal region. The section begins by describing the trigger selection and preselection used for all events. Then, the inclusive background kinematics are introduced as well as the method for deriving the background estimation. Finally, the "Elastic" selection used for selecting signal events is explained.

In all distributions pictured in this section the last bin is used for the overflow events.

3.3.1 Trigger selection

Events are chosen by the `HLT_DoublePhoton60` trigger path. This trigger was developed for the CMS inclusive diphoton high-mass resonant and non-resonant searches [74]. It requires two photon candidates to have a transverse momentum above 60 GeV and each to have a H/E value less than 0.15.

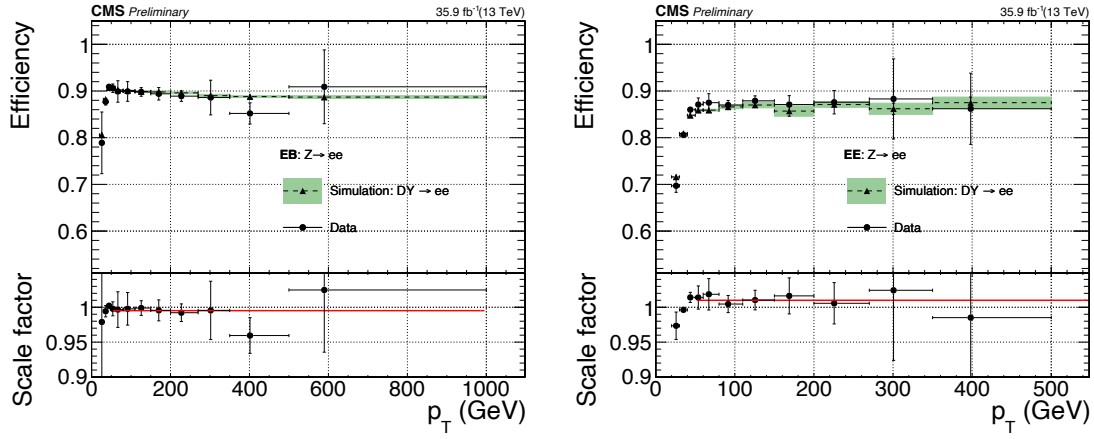

Figure 3.4: Top: Photon selection efficiency measured in barrel (left) and endcaps up to $|\eta| < 2.5$ (right) using the tag and probe method (all cuts except for electron rejection). Statistical and systematic errors are shown. Bottom: the scale factors calculated by dividing the data events by the simulated events. The scale factors are used to correct the MC used in the analysis.

The p_T cut on both photon candidates corresponds to a kinematic region where the scale factor for the HLT efficiencies have reached a plateau, as shown in Figure 3.4. A full description of the tag-and-probe technique used on $Z \to e^+e^-$ control samples for the evaluation of the selection efficiency can be found in Reference [75].

The pileup reweighting is applied on all simulated samples for the following figures. This latter allows to match the simulated primary vertices multiplicity with the "true" number of interactions in the event. For the data, the number of interactions is evaluated converting the average bunch instantaneous luminosity into the expected number of interactions per crossing for each lumi section, rescaled to the total inelastic cross section of 69.2 mb. The effect of this reweighting on the multiplicity of primary vertices distribution prior to any preselection beside the triggering and a p_T(single γ) $>$ 75 GeV, and $m_{\gamma\gamma} > 350$ GeV selection can be seen in Figure 3.5.

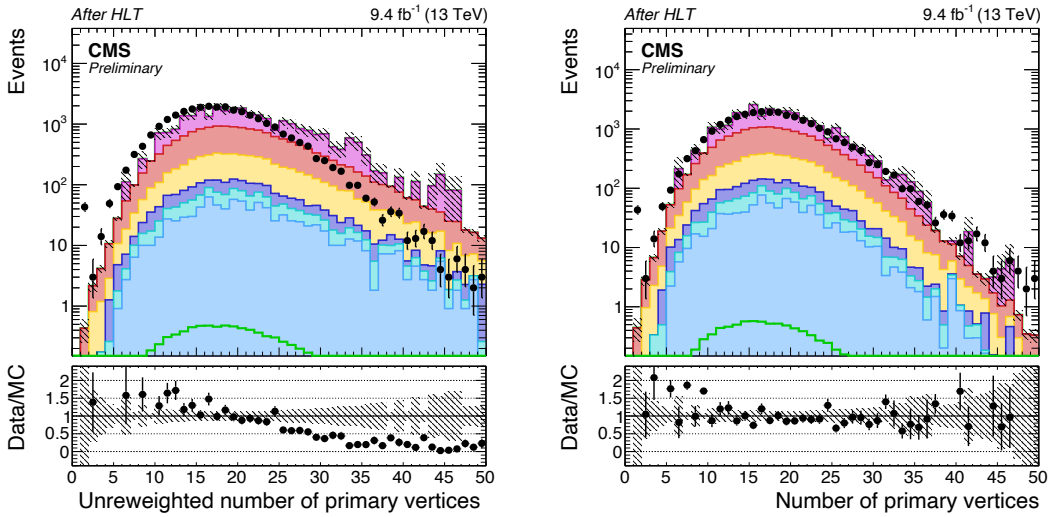

Figure 3.5: Uncorrected (left) and reweighted (right) primary vertices distribution for diphoton events with a loose preselection applied. The black points correspond to the data while the filled histograms correspond to various SM backgrounds. The pink, red, yellow, purple, light blue, and blue histograms correspond to the QCD, inclusive $\gamma\gamma$, inclusive γ, Wγ, Zγ, and $t\bar{t}$ samples, respectively. The green histogram is an AQGC signal sample multiplied by a factor of 5000 for illustration purposes.

An excess can be seen for events with one primary vertex. Most of these are coming from 'fake vertices' that can be cleaned by cutting on vertices very far (15+ cm) from the origin. Such a selection cannot be made in this study because a precise reconstruction of the diphoton vertex can not be obtained in exclusive diphoton events. However, these events have no effect on the results of the analysis.

3.3.2 Preselection

The diphoton invariant mass scale at which the loop of $W^{\pm}$ bosons is expected [27] to dominate Standard Model two-photon production of diphoton is approximately below 200 GeV. The invariant mass of the diphoton candidate is required to be above 350 GeV corresponding to the acceptance of the forward proton detectors.

Furthermore, the single photon pseudorapidity is constrained in the region $|\eta(\gamma)| <$ 2.5, with an additional veto between ±1.4442 and ±1.566, corresponding to the ECAL transition region between the barrel and the endcaps. As in CMS diphoton resonances searches, the "EEEE" category where both the photons are emitted in the electromagnetic

calorimeter endcaps, is rejected since over 90% of the signal photons are produced in the barrel. Single photons are also required to both pass the veto on prompt electrons defined in section 3.2 at this stage.

To summarize the preselection, we require:

- single photon $p_T > 50$ GeV
- a diphoton mass > 350 GeV
- $|\eta_\gamma| < 2.5$, with a veto on ECAL transition region
- at least one photon in the ECAL barrel
- prompt electron veto for leading and sub-leading photon candidate.

Figure 3.6 shows the agreement between data and MC for the diphoton mass after the preselection. Single-bin excesses can be observed in some kinematic plots. These excesses are resulting from the QCD MC that has very low statistics in these regions, and upon rescaling, these peaks are created. However, as we will see in our signal region, this QCD contribution is completely removed.

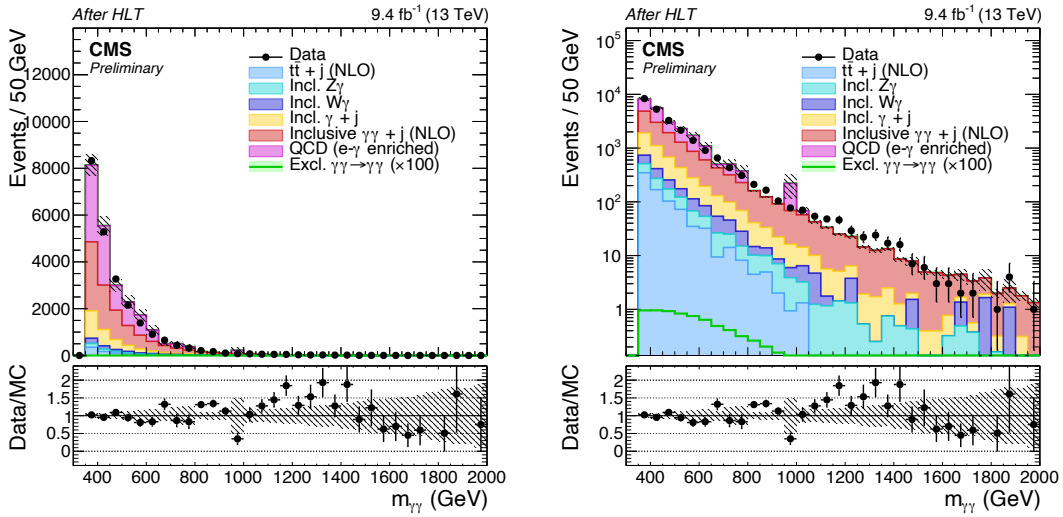

Figure 3.6: Diphoton candidates mass after the HLT selection and preselection defined in the text in linear scale (left) and log scale (right). The exclusive SM $\gamma\gamma \to \gamma\gamma$ prediction is magnified by two orders of magnitude for comparison purposes. The left and right plots are linear and log-y plots respectively.

3.3.3 Inclusive region

Although we consider all relevant types of inclusive backgrounds as seen in Figure 3.6, the inclusive $\gamma\gamma + j$ background gives the highest contribution at high mass. Here, we use $\gamma\gamma + j$ to mean a diphoton candidate in association with some form of radiation, whether it be soft radiation or hard radiation in the form of an actual jet.

To evaluate the inclusive diphoton (+jets) background modeling, a kinematic region enhancing contributions from this process is defined. On top of the preselection defined in the previous section, the single photons' transverse momentum is required to satisfy $p_T(\gamma) > 200$ GeV, and a full suppression of any exclusive contribution is ensured with an additional acoplanarity selection (see Section 3.3.4), namely $1 - |\Delta\phi_{\gamma\gamma}/\pi| > 0.025$. Cuts

made on the diphoton acoplanarity follow the single photon resolution seen in Figure 3.7.

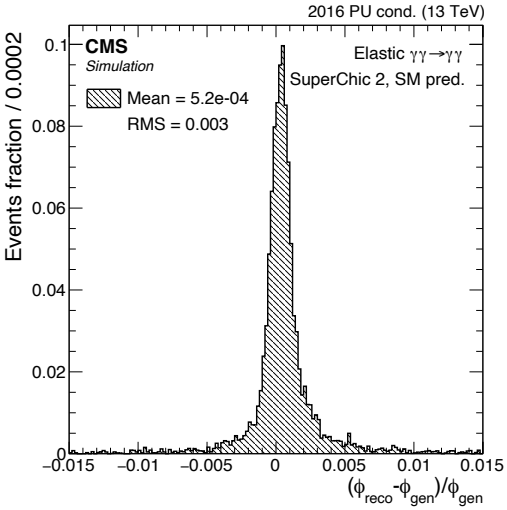

Figure 3.7: The single photon resolution found from generated and reconstructed phi values. The samples are SM LbL samples generated with SuperChic2 as described in the text. Samples using FPMC give comparable results.

In Figures 3.8 and 3.9, one can directly see the relative shape-based agreement between the inclusive distributions and the ones observed in data, once again emphasizing the good vertexing capabilities for such physics processes.

Sample	Events
Incl. $\gamma\gamma + j$	1003.3 ± 6.6
Incl. $\gamma + j$	225.5 ± 6.2
QCD	77.9 ± 62.9
Incl. $Z\gamma$	73.5 ± 2.8
Incl. $W\gamma$	61.7 ± 8.9
Incl. $t\bar{t} + j$	55.7 ± 7.8
Total predicted	1497.7 ± 64.7
Observed	1349
Data/MC	0.901

Table 3.4: Total inclusive background and observed data in the inclusive control region. All errors quoted are statistical only.

However, as illustrated in Table 3.4, a 9.9% deficit, flat in all diphoton kinematics quantities, is observed in this inclusive control region. We treat this deficit as an overall rescaling k for the dominant inclusive $\gamma\gamma + j$ background in the later stages of this analysis using:

$$k = \frac{n(\text{data}) - \sum_i n(\text{MC}_i)}{n(\gamma\gamma + j)} = 0.8518.$$

A closure test ensures this rescaling applied on the dominant background source only restores unity (1.000 ± 0.048) in the data/MC ratio for this control region. A 37% systematic error is assigned on the full reweighting procedure, corresponding to the difference observed in the k-factor extracted as a function of the acoplanarity variable (see Appendix A), and the one extracted as a flat constant.

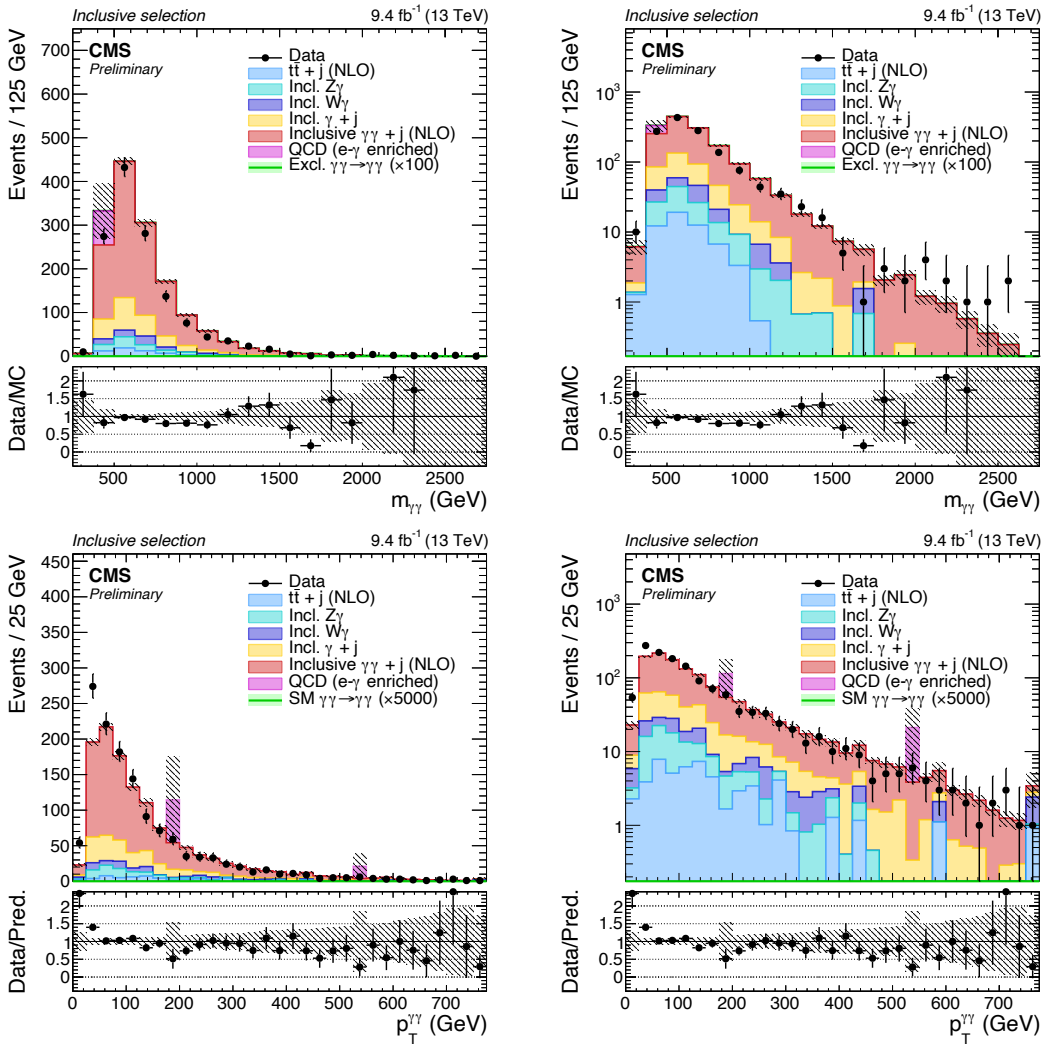

Figure 3.8: Diphoton invariant mass and transverse momentum distribution in the inclusive $\gamma\gamma + j$ region. The left and right columns are linear and log-y plots respectively.

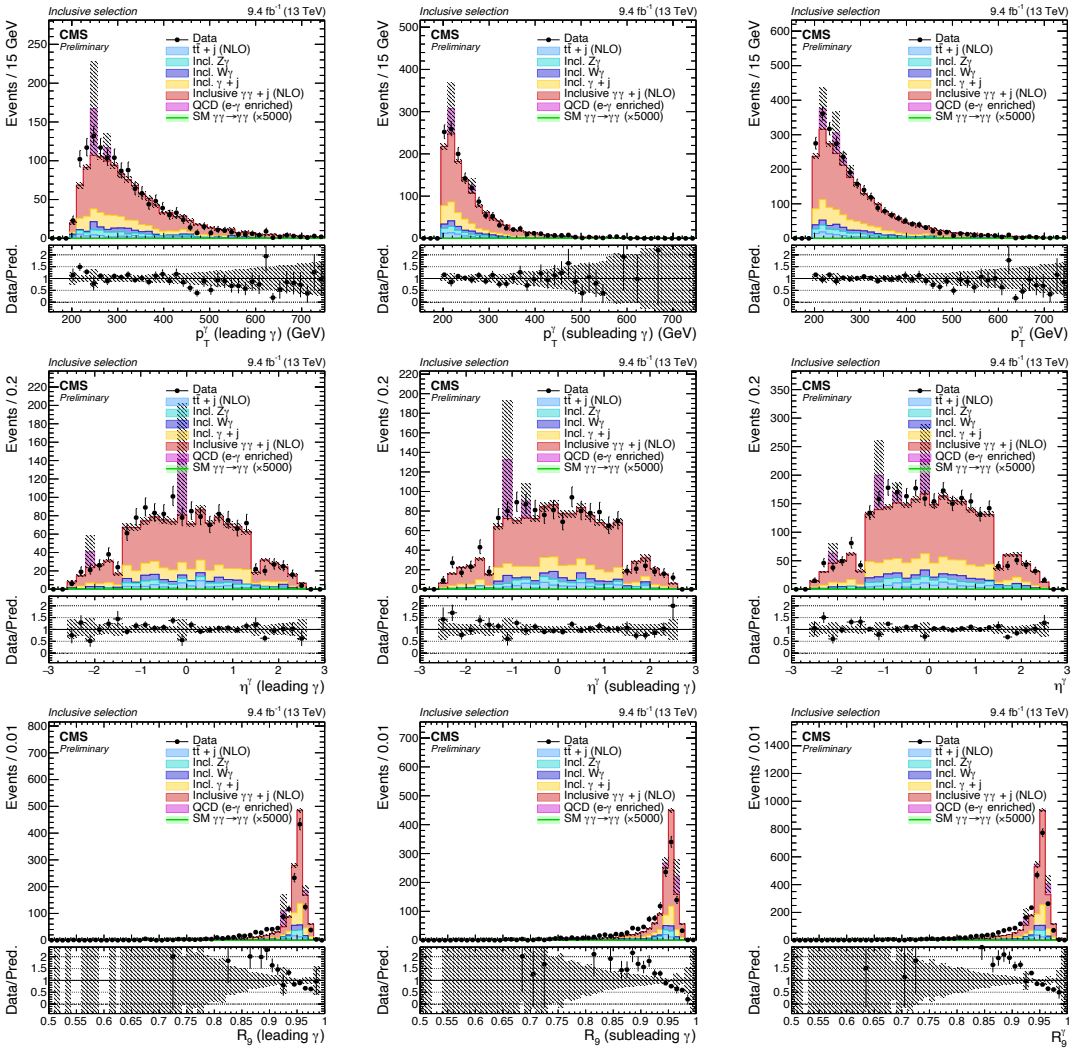

Figure 3.9: Leading, subleading, and combined photon kinematics for diphoton candidates after inclusive selection defined in the text. The exclusive SM $\gamma\gamma \to \gamma\gamma$ prediction is magnified by two orders of magnitude for comparison purposes.

Similarly to Equation 2.12, the central system ξ values can be defined as

$$\xi^{\pm}_{\gamma\gamma} = \frac{1}{\sqrt{s}} \sum_{i=1}^{2} p_{\mathrm{T}}^{\gamma_i} e^{\pm\eta_{\gamma i}},$$

corresponding to the overall momentum balance of the central event kinematics. One may note that in the case of exclusive production of such a diphoton system, this $\xi_{\gamma\gamma}$ should be matched, within uncertainties, to the forward proton momentum loss in both sectors, i.e. ξ_{RP}.

The convention we use for the plus and minus superscript refers to the outgoing forward scattered proton to be matched to the central system, hence for CMS, the positive-sign is associated to LHC sector 45 (beam 2) and the negative-sign is for LHC sector 56 (beam 1).

We show the ξ distributions for the inclusive region described here in Figure 3.10. A slight distortion within the statistical uncertainties may be observed for lower ξ values. However, we will see in later parts of this note that the higher-ξ region of interest for this study is correctly reproduced.

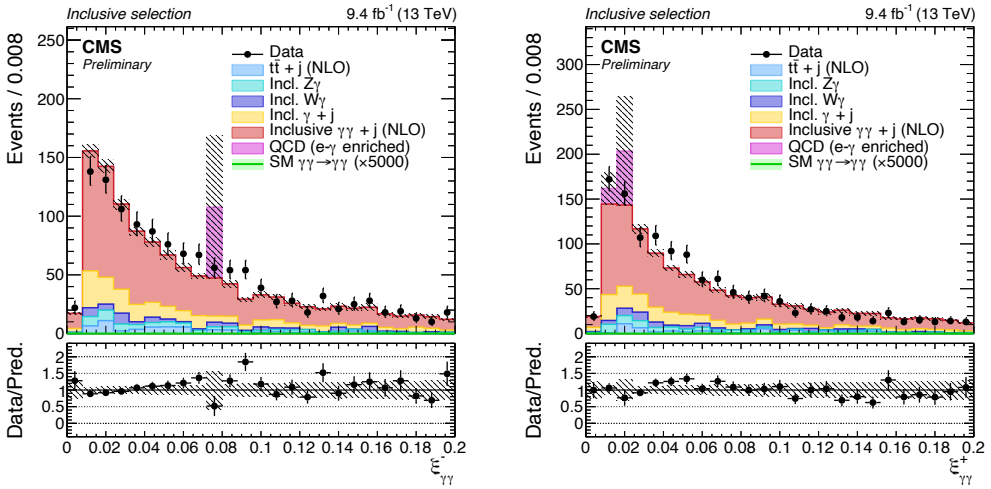

Figure 3.10: Fractional momentum loss reconstructed from the diphoton kinematics for the inclusive control region.

A templated exponential fit of observed data $\xi^{\pm}$ distributions is performed, and shown in Figure 3.11. The lower part of the fitting range is adapted to the central two-photon selection through the central-forward masses kinematical relation:

$$m_{cms} = \sqrt{s\xi_1\xi_2},$$

where the two ξ_i are the forward systems' fractional momentum losses.

Assuming symmetric distributions, the minimum ξ is 350 GeV/13 TeV = 0.027. For the upper limit of this fit, we use an upper value of 0.15 coinciding with the upper limit on the RP ξ acceptance, driven by the LHC collimators positions in 2016.

In section 3.5.4, this fitted distribution, will be used as a sampling distribution for the generation of "toy" events used in the background estimation.

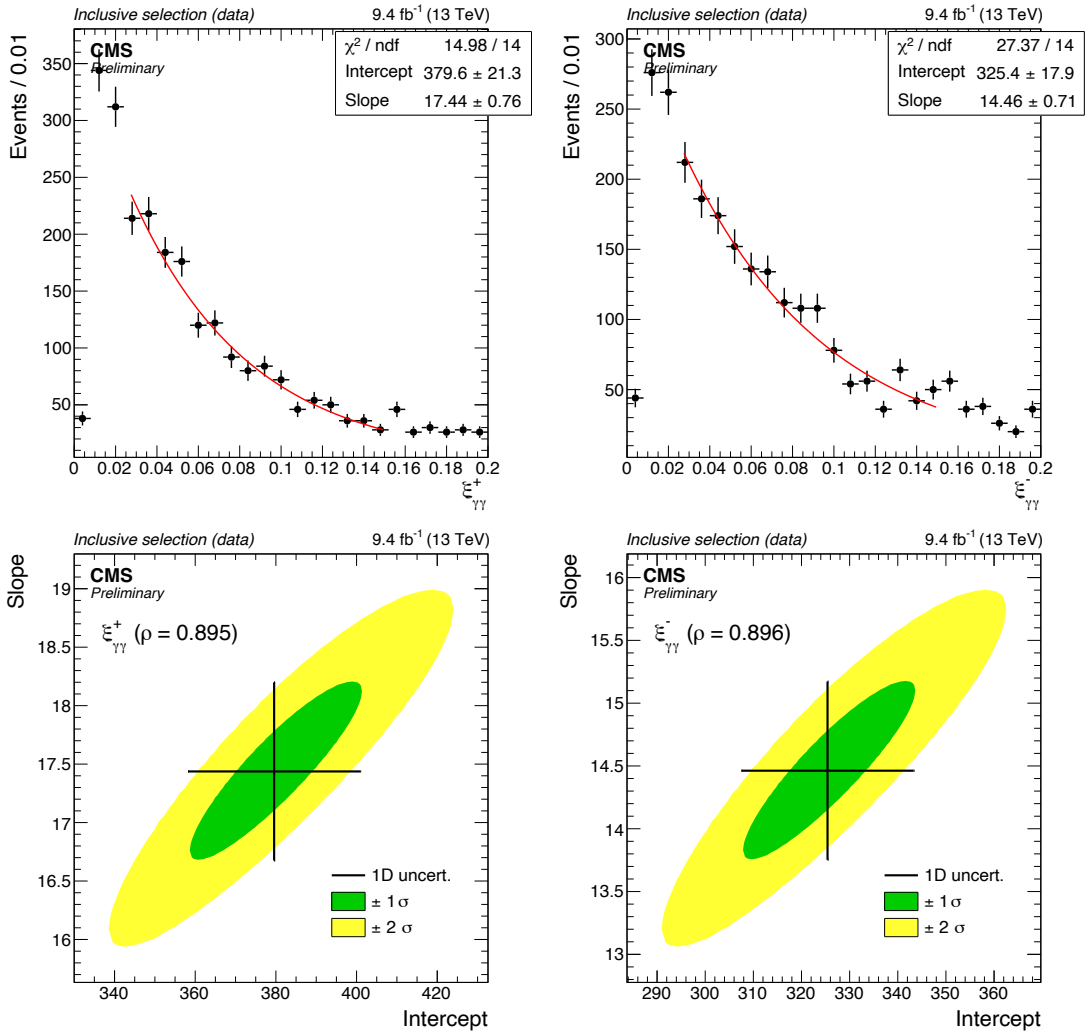

Figure 3.11: Top row: diphoton $\xi^{\pm}_{\gamma\gamma}$ spectra for sector 4-5 (left) and sector 5-6 (right) in the inclusive control region. Results of the exponential fit described in the text are displayed in the legend. Bottom row: estimated error correlation between the two fit parameters for the two sectors.

3.3.4 Elastic selection

The elastic selection is used for selecting the exclusive process of $\gamma\gamma \to \gamma\gamma$. In this special scattering process, the resulting photons are expected to be back-to-back with respect to the angle ϕ giving us a criterion from which we can select truly exclusive events.

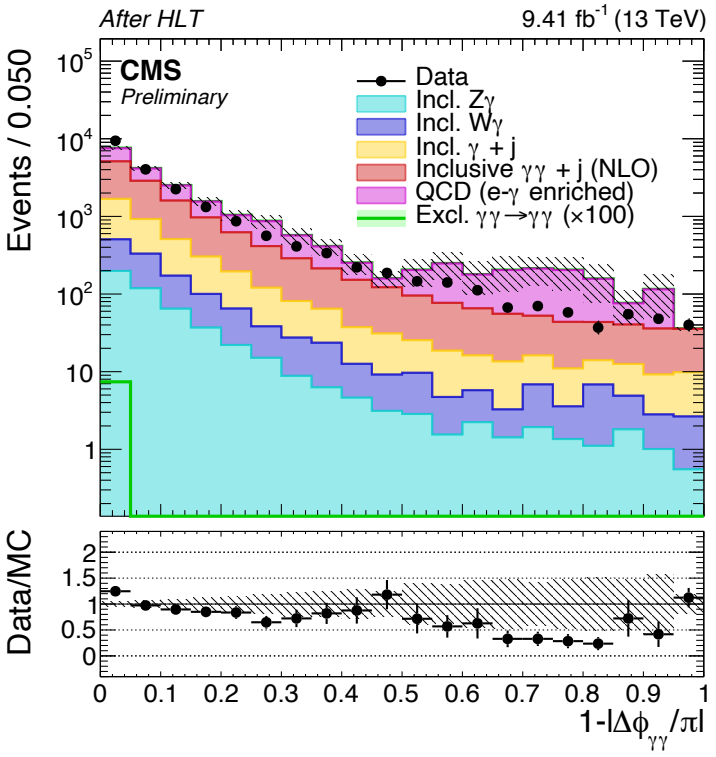

Figure 3.12: Acoplanarity distribution in the diphoton preselection region (at least one candidate with $m_{\gamma\gamma} > 350$ GeV) and $p_T^{\gamma} > 50$ GeV). An upper limit of $a < 0.005$ is applied on this variable for the selection of elastic candidates.

The main variable of interest to define this selection is the *acoplanarity* between the two photons, defined as $a \equiv 1 - \Delta\phi_{\gamma\gamma}/\pi$, with ϕ the azimuthal angle in the transverse plane (expressed in radians). This variable provides an excellent rejection of major inclusive backgrounds. Similarly to the two-photon production of dilepton discussed in [60], the photon-induced productions are expected to peak sharply at low-a. Hence, a $a < 0.005$ selection is applied. As described in section 3.2, the $R_9 > 0.94$ cut is applied to this selection region for identifying photons. Figure 3.12 shows the distribution of this variable throughout the data and MC at the preselection level.

Two-photon and single photon level control distributions can be seen for this elastic selection in Figures 3.13 and 3.14 respectively. Figure 3.15 shows the data/MC agreement between the number of diphoton candidates and the p_T^{miss}.

The most striking discrepancy arises in the reconstructed $p_T^{\gamma\gamma}$ spectrum for this coplanar selection. This effect is foreseen from the vertexing argument developed below. Unlike the early Run 1 CMS searches for two-photon production of lepton pairs [76], no selection is hence applied on this distribution in the following part of this analysis.

Sample	Events
Incl. $\gamma\gamma + j$	202.4 ± 2.9
Incl. $\gamma + j$	48.3 ± 2.9
Incl. $V\gamma$	0.7 ± 0.3
Total expected	251.4 ± 4.1
Observed	266
Data/MC	1.058

Table 3.5: Total inclusive backgrounds and observed data in the elastic signal search region (no further $\xi_{\gamma\gamma}$ selection is applied). All errors quoted are statistical only.

As listed in Table 3.5 and shown in Figures 3.13, 3.14, and 3.15, we observe a good agreement between expected and observed yields in most spectra for this elastic region. A 3σ excess of 5.8%, constant for the large majority of kinematics distributions of interest is observed in this search region.

A summary of the selections defined in this section can be found in Table 3.6.

Region	**Cuts**
HLT selection	HLT_DoublePhoton60* trigger
Preselection	HLT selection $p_{T\gamma} > 75$GeV $\eta < 2.5$ (transition veto) EBEB and EBEE only $m_{\gamma\gamma} > 350$ GeV
Inclusive selection	Preselection p_T (γ) > 200 GeV acop. > 0.025
Elastic selection	Preselection $R_9 > 0.94$ acop. < 0.005

Table 3.6: A summary of the various selection regions described in section 3.3.

Central system resolution

The offline diphoton vertex reconstruction is optimised for a large multiplicity of tracks observed in the central tracker. However, any elastic (two-photon) production of this central system predicts a diphoton primary vertex lacking additional charged tracks produced in its vicinity.

Therefore, the resolution on its transverse momentum and pseudorapidity is expected to drop with respect to the inclusive production processes.

In Figure 3.16, the vertices multiplicity, longitudinal position, and multiplicity of additional vertices surrounding the diphoton vertex are shown.

The resolution on this central two-photon kinematics is evaluated using the high-statistics elastic LbL SM signal samples described in section 3.1.3.

As pictured in Figure 3.17, when applying the elastic selection defined above, the diphoton mass and rapidity resolutions from the central system are reasonably good.

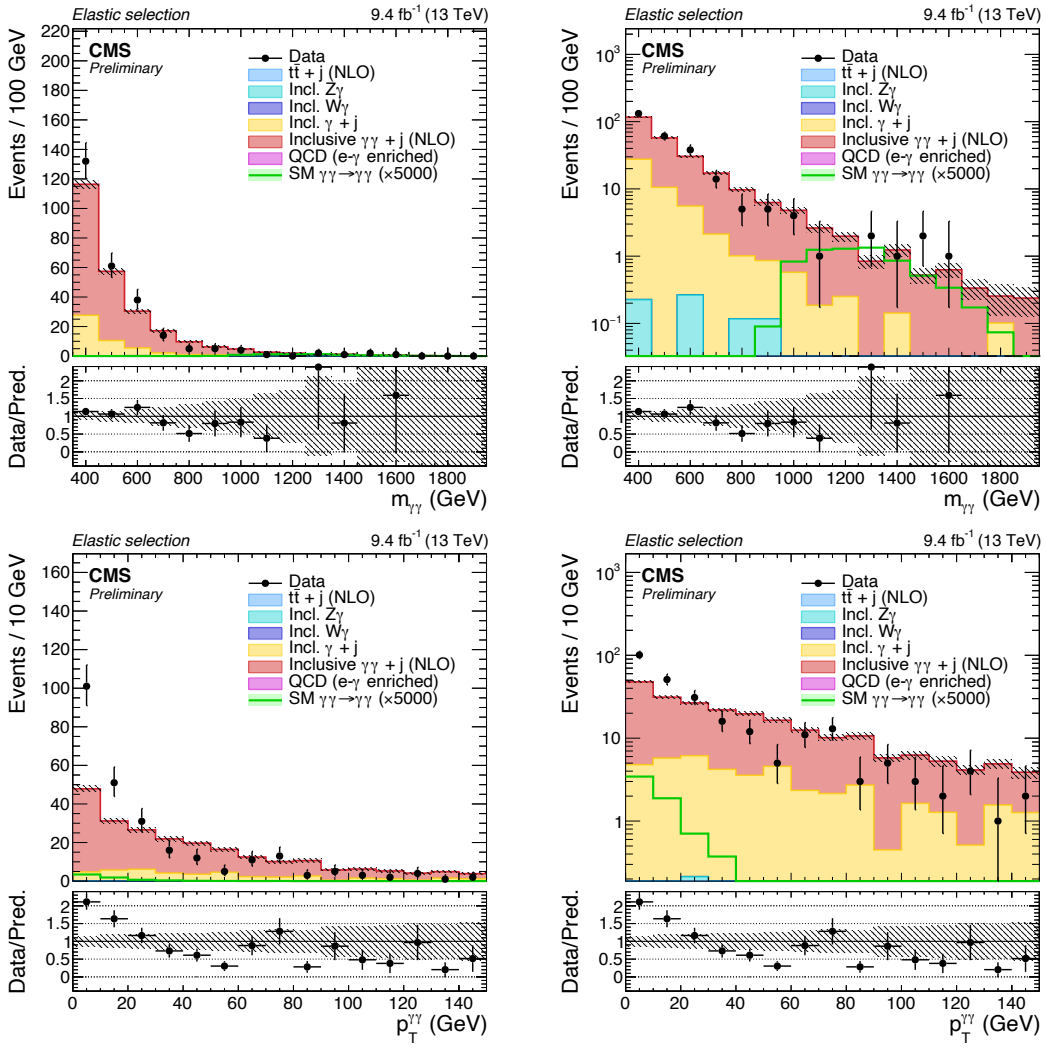

Figure 3.13: Linear and logarithmic scale distributions of the diphoton invariant mass spectrum in the elastic control region. Bottom figure depicts the photon pair transverse momentum distribution for the signal search region. As described in the text, the poor agreement for the latter is attributed to exclusive diphoton vertexing performances.

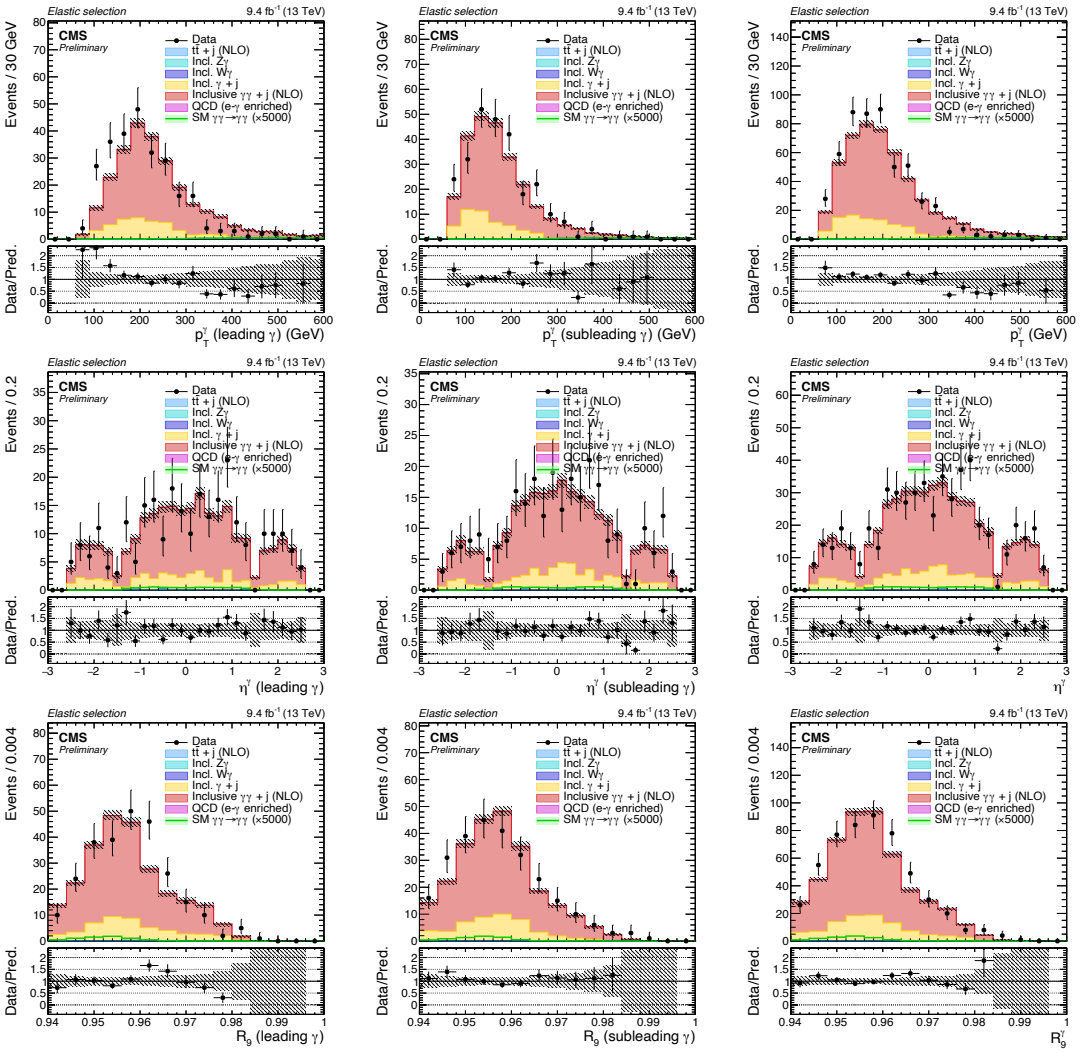

Figure 3.14: Single photon distributions for the elastic search region defined in the text. The rows, from top to bottom, show the p_T, η, and R_9. The columns, from left to right, show kinematics for the leading photon, subleading photon, and both photons. The exclusive SM $\gamma\gamma \to \gamma\gamma$ prediction is magnified by two orders of magnitude for comparison purposes.

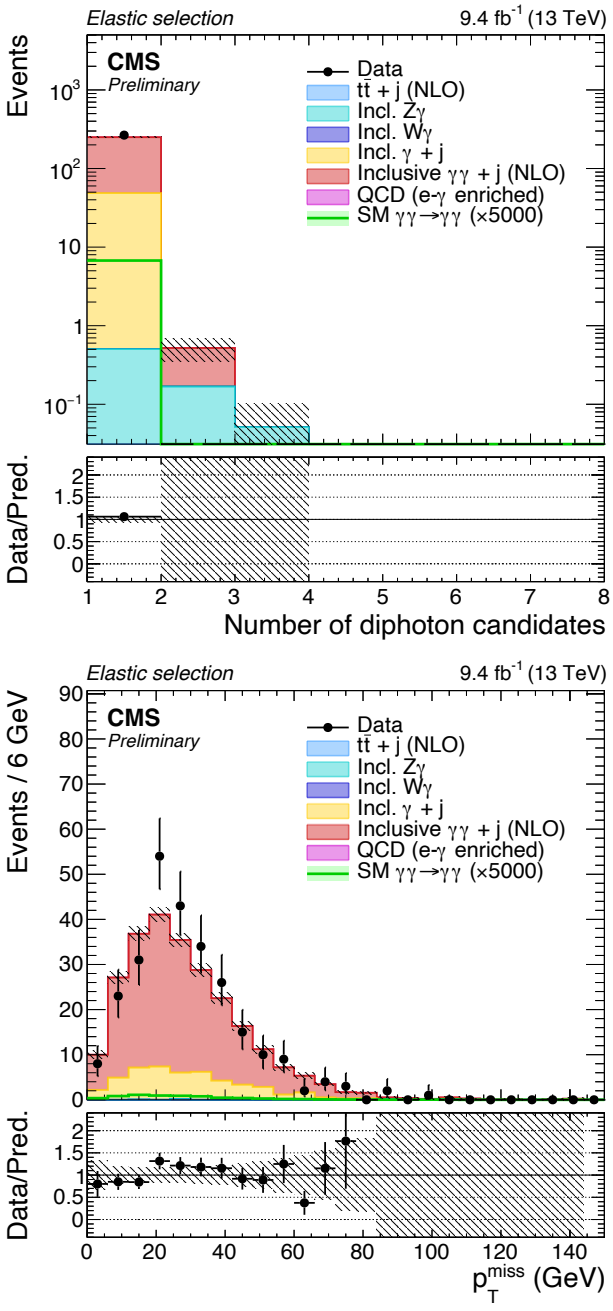

Figure 3.15: Left: number of elastic diphoton candidates reconstructed in the event. Right: total missing transverse energy for events with a diphoton system passing the elastic selection.

Both the FPMC and SuperChic 2 samples are used for comparison. For the latter, the loosest resolution among the two samples is used conservatively. Using the generator-level kinematic truth associated to each photon in all pairs, the expected mass and rapidity resolutions for the two-photon system are 2% and resp. 7.4%.

Additionally, we study the resolutions as a function of pileup. Then, the resolutions are studied based on low, average, and high pileup conditions as seen in Figure 3.18. We conclude that the mass and rapidity are not heavily dependent on the pileup conditions for the number of vertices in this range.

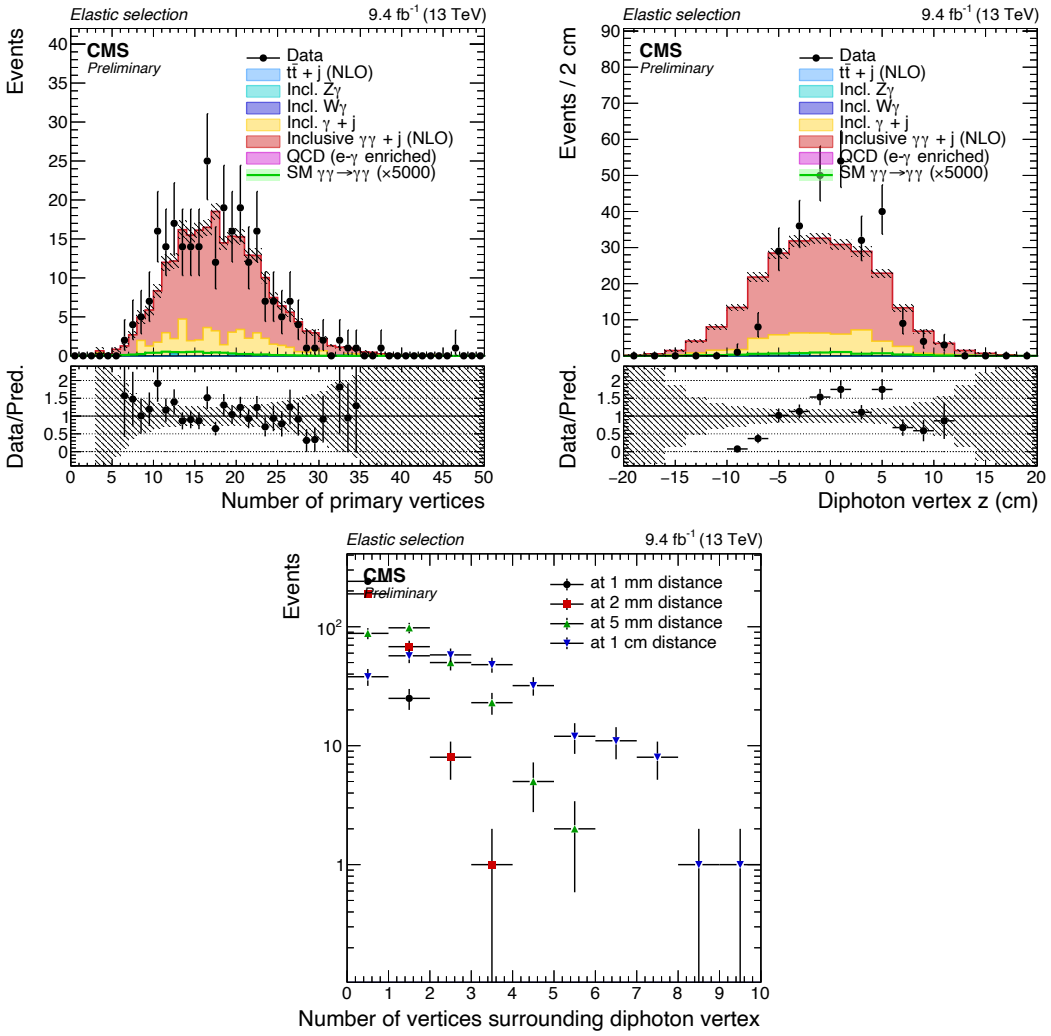

Figure 3.16: From left to right, top to bottom: primary vertices multiplicity for events with a diphoton candidate passing the elastic selection, longitudinal position of elastic diphoton vertices, and multiplicity of vertices reconstructed at a given distance of this diphoton candidate vertex.

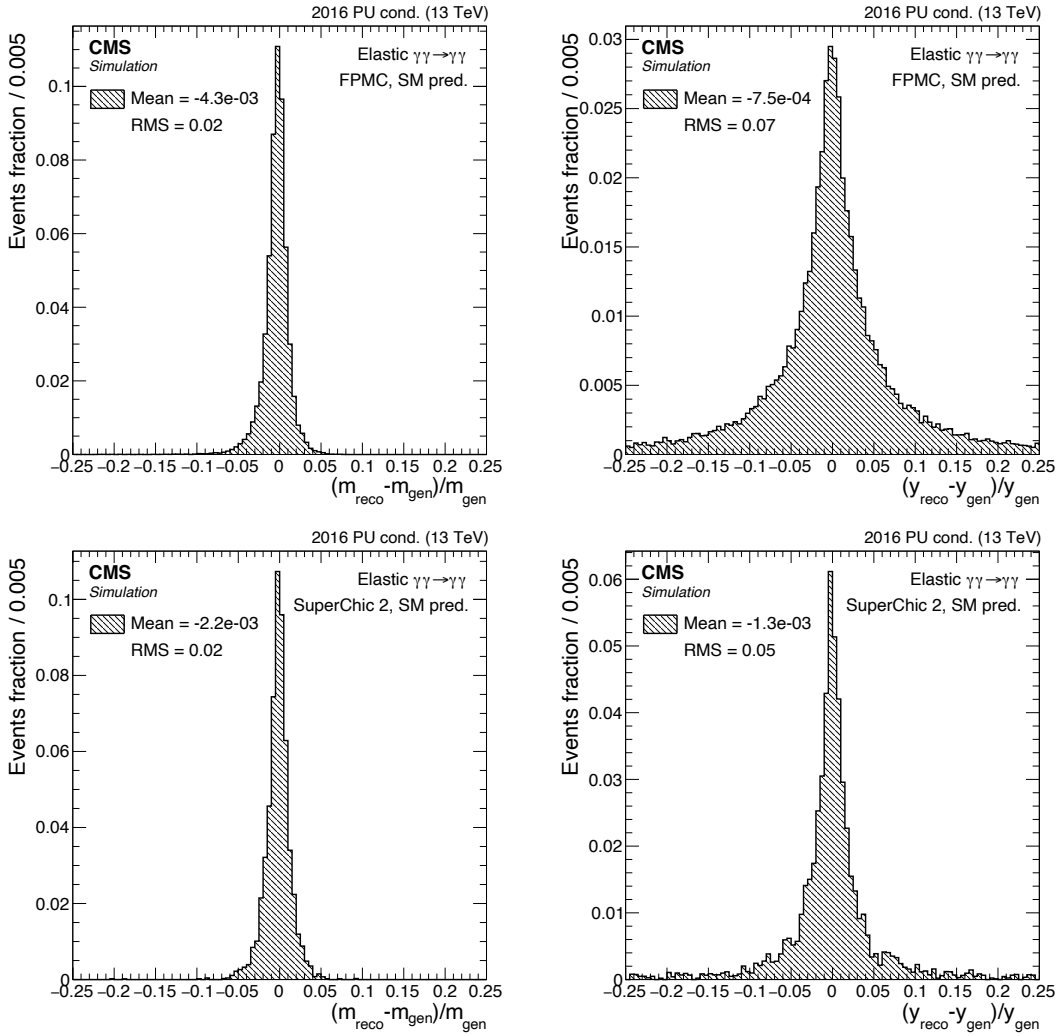

Figure 3.17: Central two-photon mass and rapidity resolutions evaluated for the SM LbL signal kinematics. The signal samples are generated with FPMC (top row) and SuperChic 2 (bottom row), as described above.

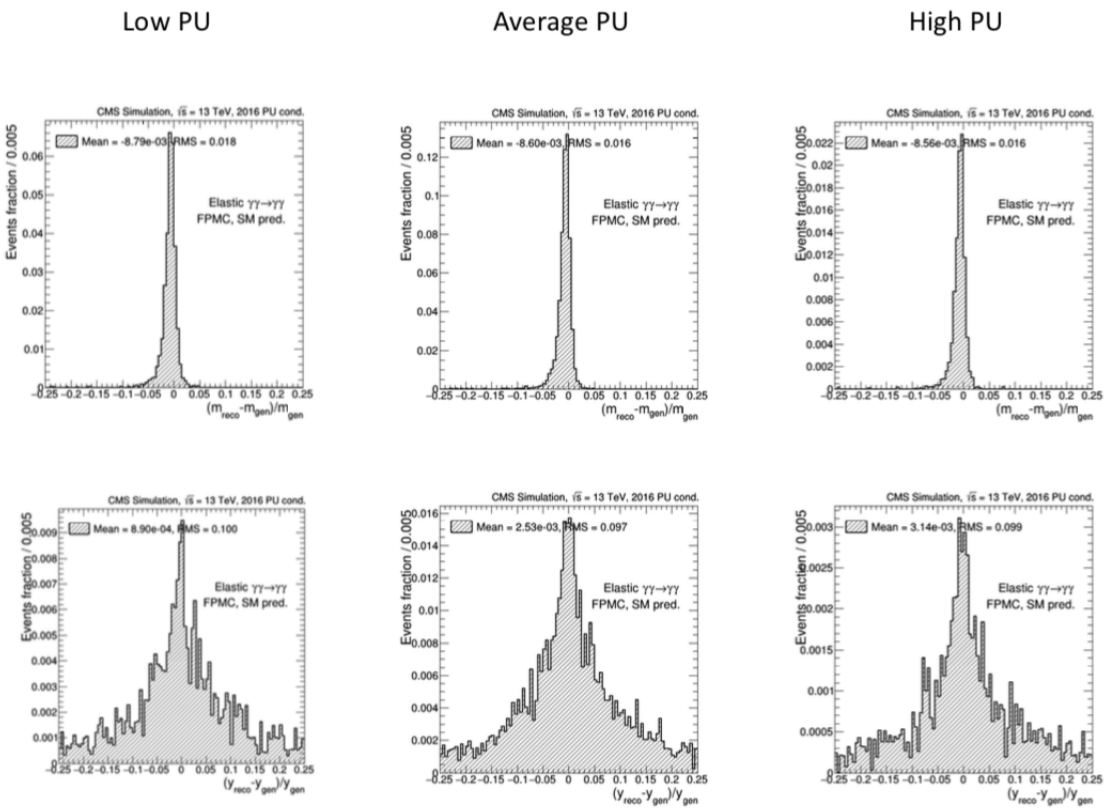

Figure 3.18: Mass and rapidity resolutions for events selected from an FPMC sample of anomalous coupling events. These resolutions are studied in three categories: low pileup, average pileup, and high pileup. The low pileup category are events with less than 14 vertices, average pileup events have a number of vertices between 14 and 24, and high pileup events are chosen as having more than 24 vertices. It is concluded that the resolution is not significantly affected by the number of pileup vertices.

3.4 Proton tagging

3.4.1 Forward pots alignment and ξ reconstruction

Proton tagging is performed using the CMS and TOTEM Precision Proton Spectrometer described in Section 2.3. In the 2016 configuration used for this study, the following nomenclature is used:

- 45-near and -far: $+z$-direction of CMS, 210 m from IP5
- 56-near and -far: $-z$-direction of CMS, 210 m from IP5

Following the discussion in Section 2.3.4, a set of alignment parameters allows the x/y map of forward proton tracks to be corrected before the extraction of the tracks kinematics. In 2016, the proton reconstruction used a linearized version of the proton transport equation:

$$x(s) \simeq v_x x^* + L_x \vartheta_x^* + D_x \xi \simeq D_x \xi, \tag{3.2}$$

with v_x the vertex offset, L_x the horizontal effective length, and D_x the horizontal dispersion involved in the leading term. All relevant parameters are extracted for the 2016 optics layout observed during data taking [58].

An ξ-dependent dispersion interpolation function is used for all four stations. The linear approximation satisfies the proportion $D_x \simeq x_0/\xi_0$ for every station, where

- ξ_0 is the momentum loss such as the vertical effective length $L_y(\xi_0) = 0$, as simulated by the MAD-X beamline parameterization.
- x_0 is the "pinch point" observed in the two-dimensional tracks distribution where $L_y(\xi)$ vanishes and leads to a higher occupancy around $y = 0$.

The momentum loss uncertainty quantifies the bias introduced by the linearization shown in the last term of 3.2, namely:

$$\delta\xi_{\text{bias}} = \frac{v_x x^* + L_x \vartheta_x^*}{\xi}.$$

It can be defined from the following terms, added in quadrature:

- the uncertainty on pots horizontal alignment (150 μm)
- a term modeling the vertex transverse size (a conservative 10 μm resolution is used)
- a term accounting for the angular beam spread (divergence) at the interaction point (we use 20 μrad),
- a sensors spatial resolution uncertainty of 12 μm
- a per-pot uncertainty on the dispersion values.

The dispersion uncertainty contribution is evaluated for all four pots used in this study. The ξ-independent value of their relative resolution is listed in Table 3.7.

	45-near	45-far	56-near	56-far
δD_x (%)	3.87	4.35	5.26	6.14

Table 3.7: Dispersion uncertainty computed for all four sensors used in this analysis. Values extracted from [58].

Combining all the effects mentioned above, the overall longitudinal momentum loss uncertainty is pictured as the thick black line in Figure 3.19, with all contributions displayed for illustration purpose.

3.4.2 Forward tracks acceptance

According to the crossing angle and dispersion configuration used in 2016, an estimate of the mass and rapidity acceptance for the central system is shown in Figure 2.11. The observed minimum value of the ξ acceptance is observed to be lower than the expectation from the machine parameters. The data-driven ξ_{min} acceptance is calculated in all four pots after the proton reconstruction procedure. The minimum value is defined as the value of ξ such that less than 1% of forward tracks are rejected. This effect is observed in both sectors, although, it is more prominent in sector56 as seen in Figure 3.20.

The expected and observed ξ_{min} values are shown in Figure 3.21 for all pots for events containing a diphoton candidate.

RP	45N	45F	56N	56F
Nominal ξ_{min}	0.033	0.024	0.050	0.037
Observed ξ_{min}	0.034	0.023	0.042	0.032

Table 3.8: Lowest ξ values as expected from the LHC optics and observed in data for each RP in the 2016 beam optics conditions.

3.4.3 Strips efficiency

The total strips inefficiency can be factorised in two major contributions: the strips multi-tracking inefficiency, and the radiation damage inefficiencies.

Multi-tracking inefficiency

The first inefficiency source results from the failure of the reconstruction algorithm for the silicon strip detectors when more than one proton is present in a given bunch-crossing. Designed for low-luminosity data taking conditions, the algorithm for reconstruction with strip detectors is not compatible with events having more than five non-contiguous hits within one detector plane. A negative correlation between the RP efficiency and the number of vertices at the IP can be seen in Figure 3.22. For simplicity, the multi-tracking inefficiency is taken to be constant at 70% and we associate a 10% absolute systematic uncertainty.

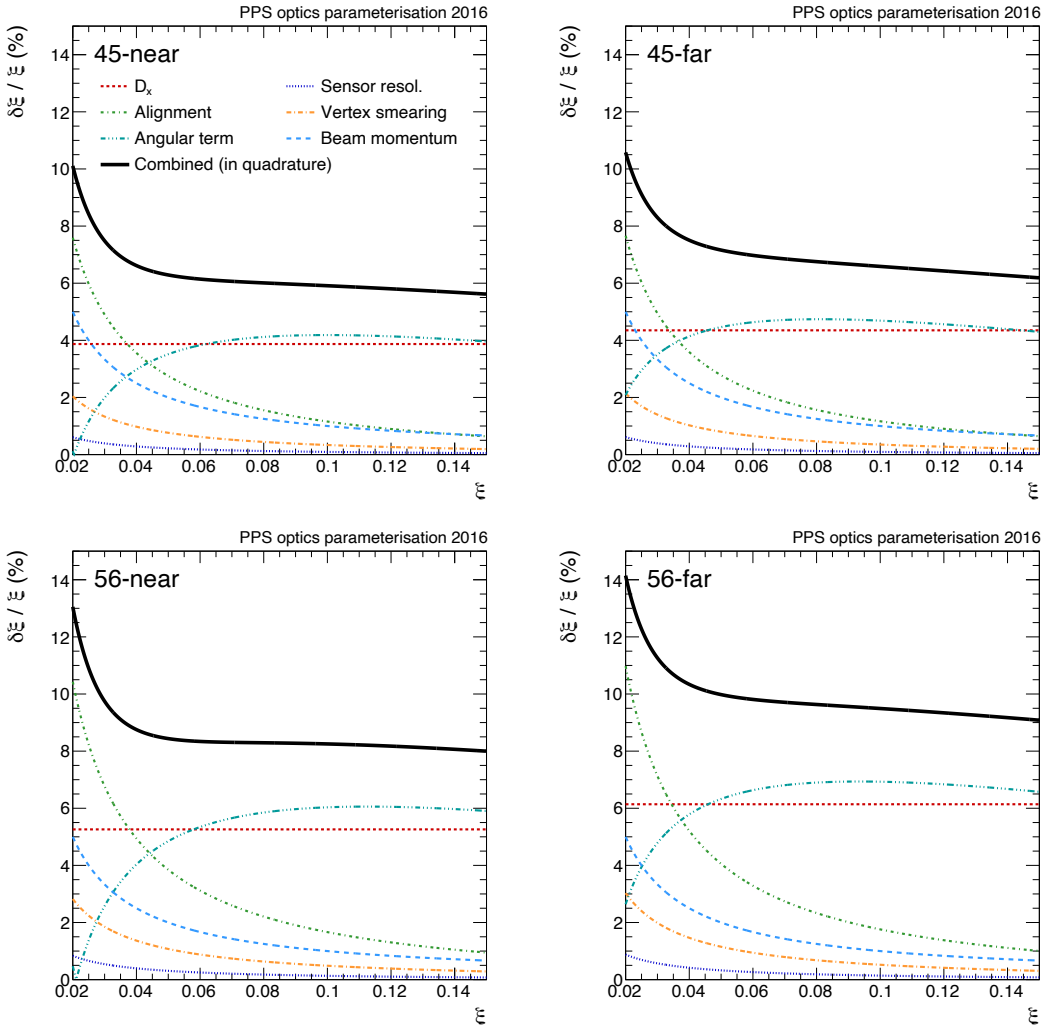

Figure 3.19: Uncertainty on the longitudinal momentum loss ξ as reconstructed from the PPS forward tracks horizontal position.

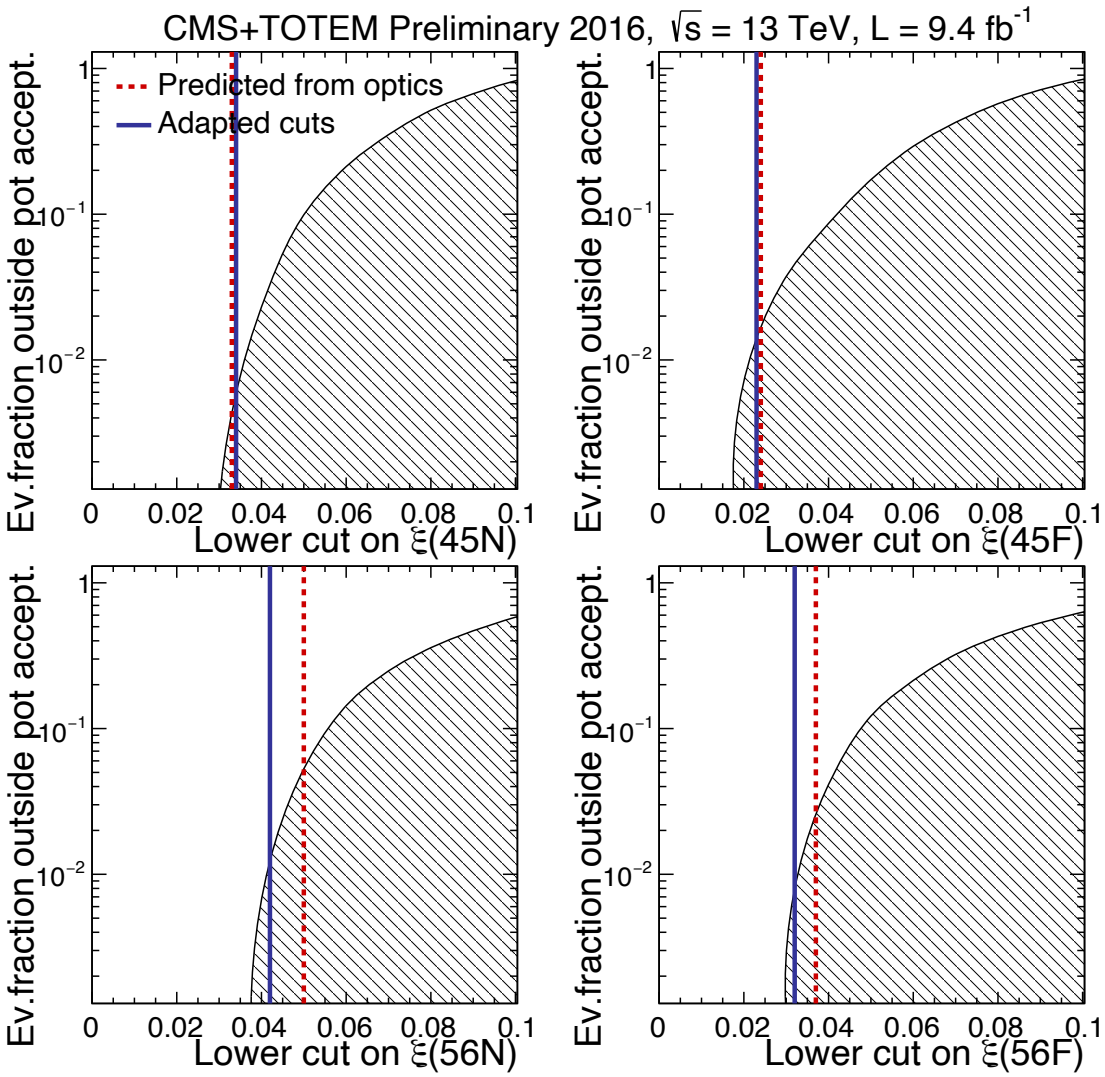

Figure 3.20: Cumulative ξ distribution for the 4 strips passing the same L1 trigger selection as used to select signal events. The vertical lines represent the minimum ξ value used in each station defined as the maximum value where less than 1% of forward tracks are rejected. The red dotted line is the minimum ξ value predicted analytically from the LHC optics and the blue line is the observed value.

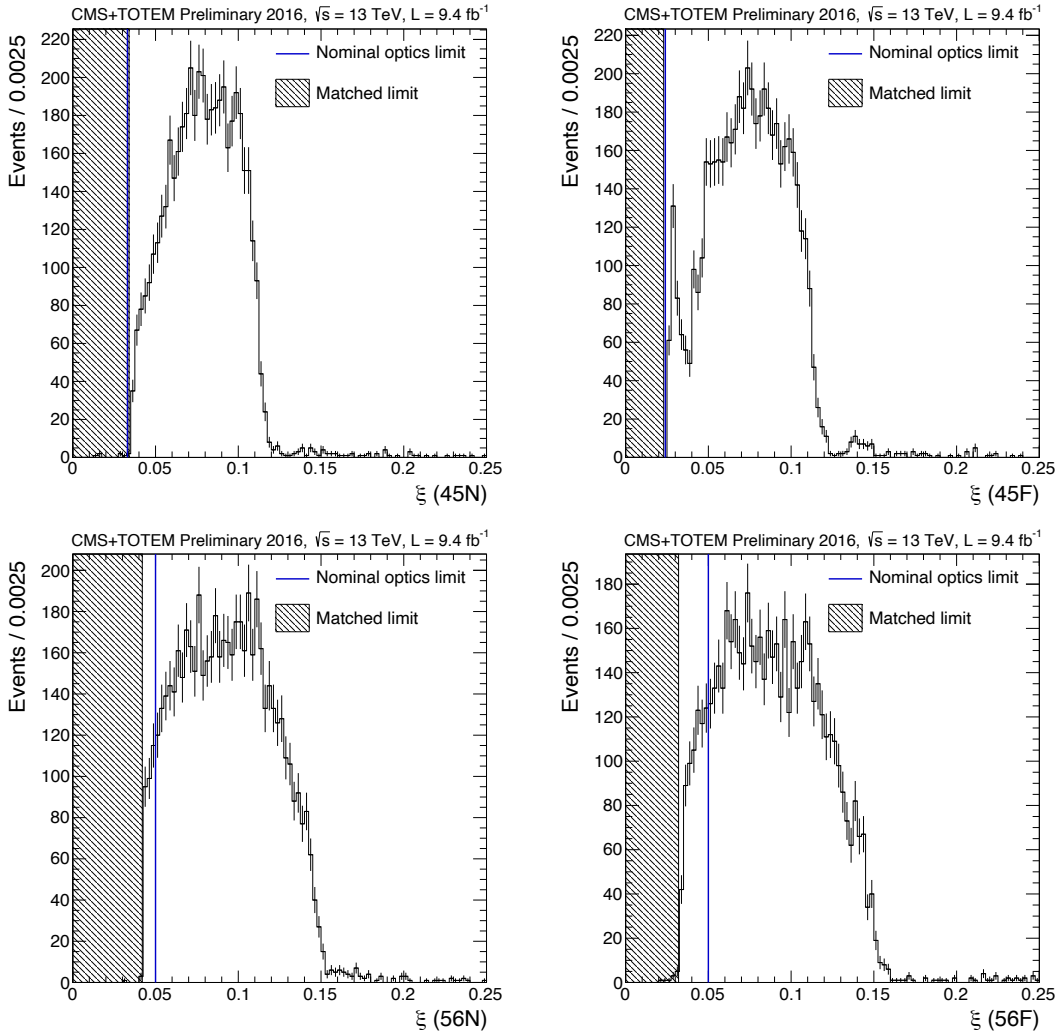

Figure 3.21: ξ spectrum for events containing at least one diphoton pair, for all four silicon strips Roman pots. From top to bottom, LHC sector 45 and 56 pots. The greyed out area corresponds to the region out of the individual pots acceptance. The blue line corresponds to the expected acceptance.

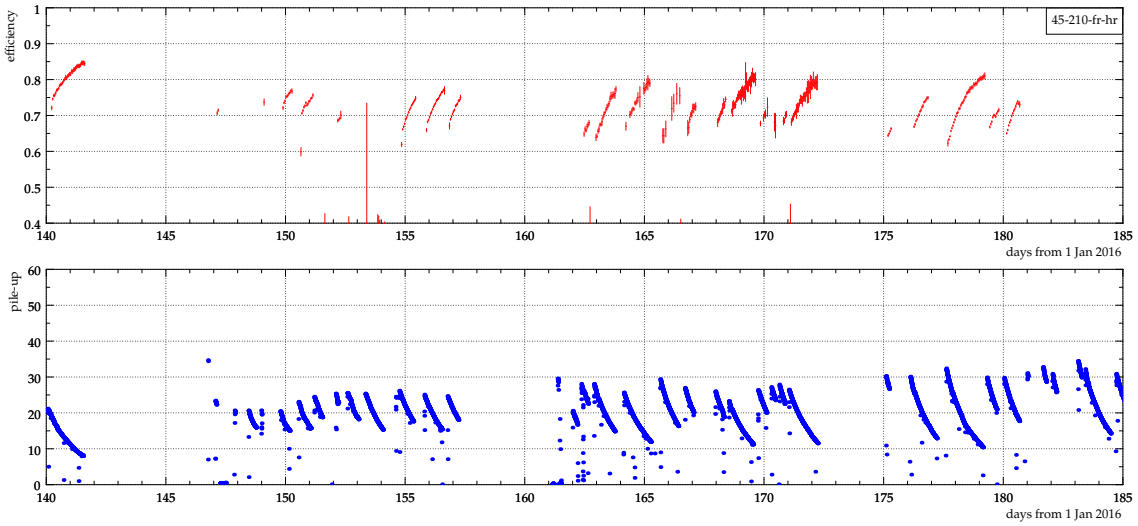

Figure 3.22: Reconstruction efficiency as observed during the full 2016 data-taking period, for the 45-far pot (top). The average vertex multiplicity at IP5 during the same period. A strong negative correlation is observed between the two plots.

Radiation Damage

The second source of inefficiency stems from the radiation damage to the RPs because of their proximity to the LHC beam. The effect is therefore time and luminosity dependent causing a decrease in the sensitivity of the detectors.

During the 2016 data taking period the inefficiency reached a level that caused the RPs to be removed from the data acquisition system. Later on in 2016, an increase in the operating voltage (300 V) allowed for the data acquisition to resume.

To understand the extent of the inefficiency created by the radiation damage, we studied each individual LHC fill in 2016 with respect to a reference fill when the detectors were operating at optimal conditions. The reference fill was chosen to be the alignment run used for the horizontal PPS stations utilizing the same beam properties. The radiation damage in the reference period is assumed to be negligible.

The radiation damage is most prevalent at low values of ξ (and thus, low values of x) as can be seen in Figure 3.23. This kinematic region has a minimal effect on the high mass (and hence high ξ) diphoton signal.

The behavior of this efficiency as a function of ξ can be modeled through the following template:

$$\epsilon(\xi) = \frac{p_2}{2}\left[1 + \mathrm{erf}\left(\frac{\xi - p_0}{p_1}\right)\right], \tag{3.3}$$

where erf is the error function. Three degrees of freedom $p_{0,1,2}$ represent the ξ_0 value such that $\epsilon(\xi_0)$ cancels, the slope parameter, and the asymptotic efficiency value, respectively. The value of these parameters after the fit can be seen in the legend of Figure 3.24 with the format (p_0, p_1, p_2).

In Table 3.9, the lower limit on the ξ region with less than 10% radiation damage inefficiency is shown.

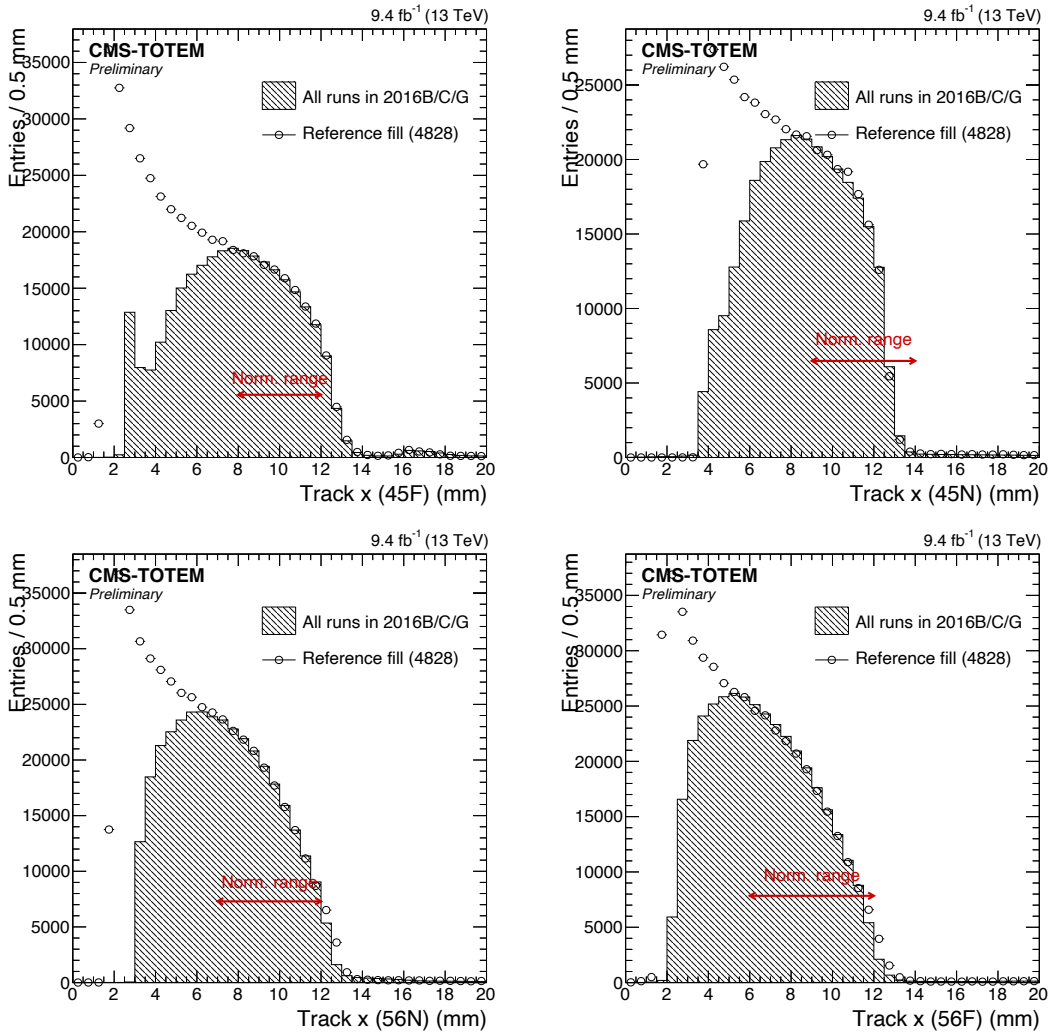

Figure 3.23: Horizontal track coordinates spectrum for diphoton events passing the L1 trigger selection that have been normalized. The radiation damage is portrayed by the gap between the number of events for the individual fills, and the reference fills.

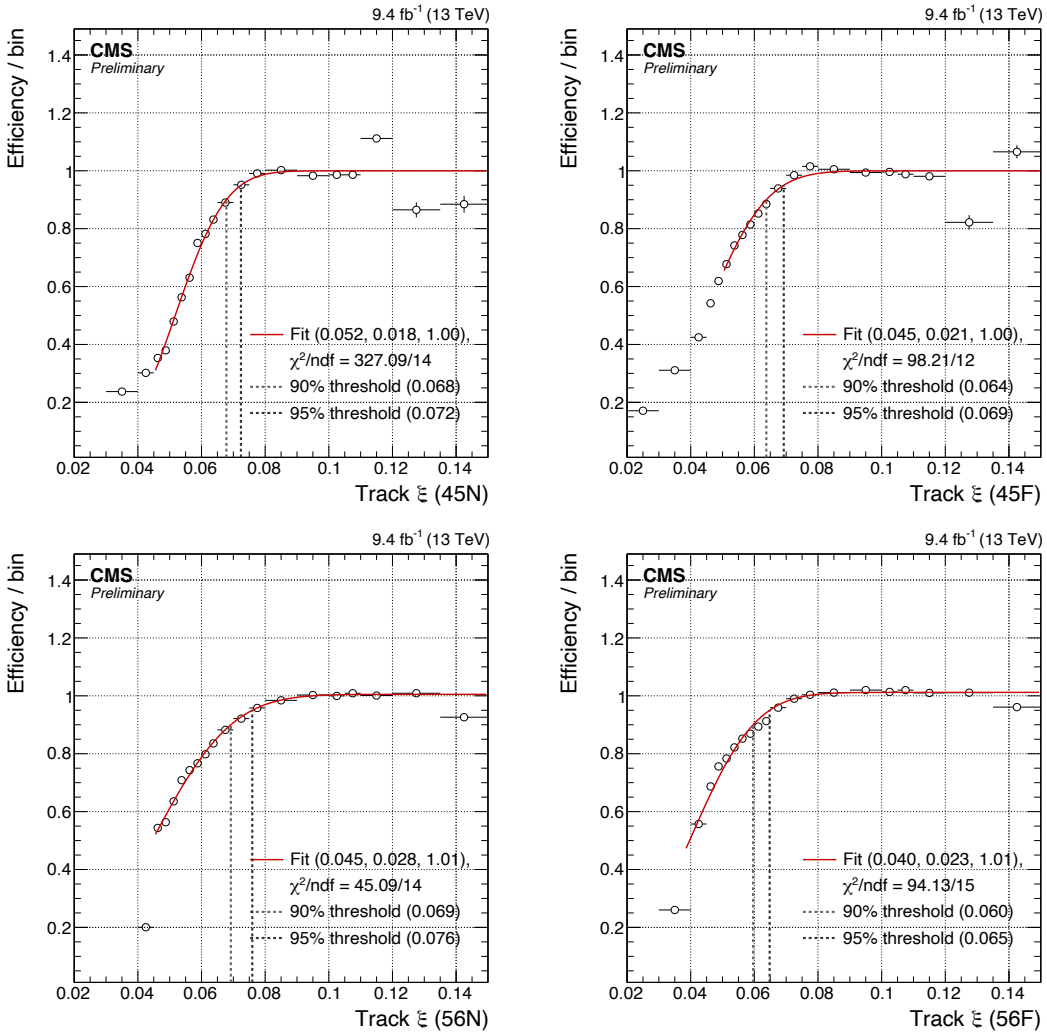

Figure 3.24: Summary of radiation damage component of the total PPS silicon strips inefficiency for all four pots used in pre-TS2 2016 data taking. A template fit is performed using the Eq. 3.3 template. Resulting fitted p_{0-2} parameters are quoted between parenthesis in all four legends. The regions with efficiency above 90% are used in this study.

Pot	45N	45F	56N	56F
observed min(ξ)	0.033	0.024	0.050	0.037
ξ s.t. $\epsilon(\xi) > 90\%$	0.068	0.064	0.069	0.060

Table 3.9: Lower limits on ξ_{RP} for the different pot acceptance and radiation damages selections defined in the text.

Additionally, the fit to the ξ distribution for sectors 45 and 56 performs poorly for values above 0.110 and 0.138, respectively. It was chosen to use these asymmetric values as upper limits for the region with less than 10% radiation damage. We choose to exclude events having a reconstructed ξ value within the range where the radiation damage inefficiency is less than 10%. The lower selection on ξ is shown in Figure 3.25.

3.5 Results

3.5.1 Diphoton candidates

A tightened selection of the diphoton candidates can be defined using the ξ_{RP} limits extracted in section 3.4.3. In addition to the selection criteria defined in 3.3, $\xi_{\gamma\gamma}$ can be further required to be within the ξ range where the PPS detectors have a less than 10% radiation damage inefficiency.

A summary of the relative agreement between MC and data for all selections described in Section 3.3 (bins 1-3) and with a $\xi^{\pm}_{\gamma\gamma}$ compatible with the PPS strips detectors acceptance (bin 4) or such that the strips radiation damage is under 10% following the procedure described above (bin 5) can be found in Figure 3.26. Table 3.10 shows the selection efficiency for a SM signal sample with a prior $0.07 < \xi < 0.15$ selection (compatible with the forward tracks acceptance with less than 10% radiation damage), and $p_T(\gamma) > 75$ GeV, along with the number of events observed in data for all these diphoton kinematic regions.

Central system selection	Signal	Data
HLT + diphoton preselection	72.3%	23650
Elastic selection	28.9%	266
$\xi^{\pm}_{\gamma\gamma}$ in PPS strips acceptance	28.7%	43
$\xi^{\pm}_{\gamma\gamma}$ s.t. $\epsilon_{rad}(\xi) > 90\%$	21.1%	2

Table 3.10: Summary of signal efficiency and cut flow for the successive selection stages defined in the text. No forward proton selection is applied there.

3.5.2 Central-forward matching

Forward tracks originating from pileup and detected in PPS are the main source of coincidental background. Therefore, we require the central system's kinematics to be compatible (within a given number of standard deviations) with the forward tracks. The kinematic variables of interest for this matching are the mass and rapidity of the two systems.

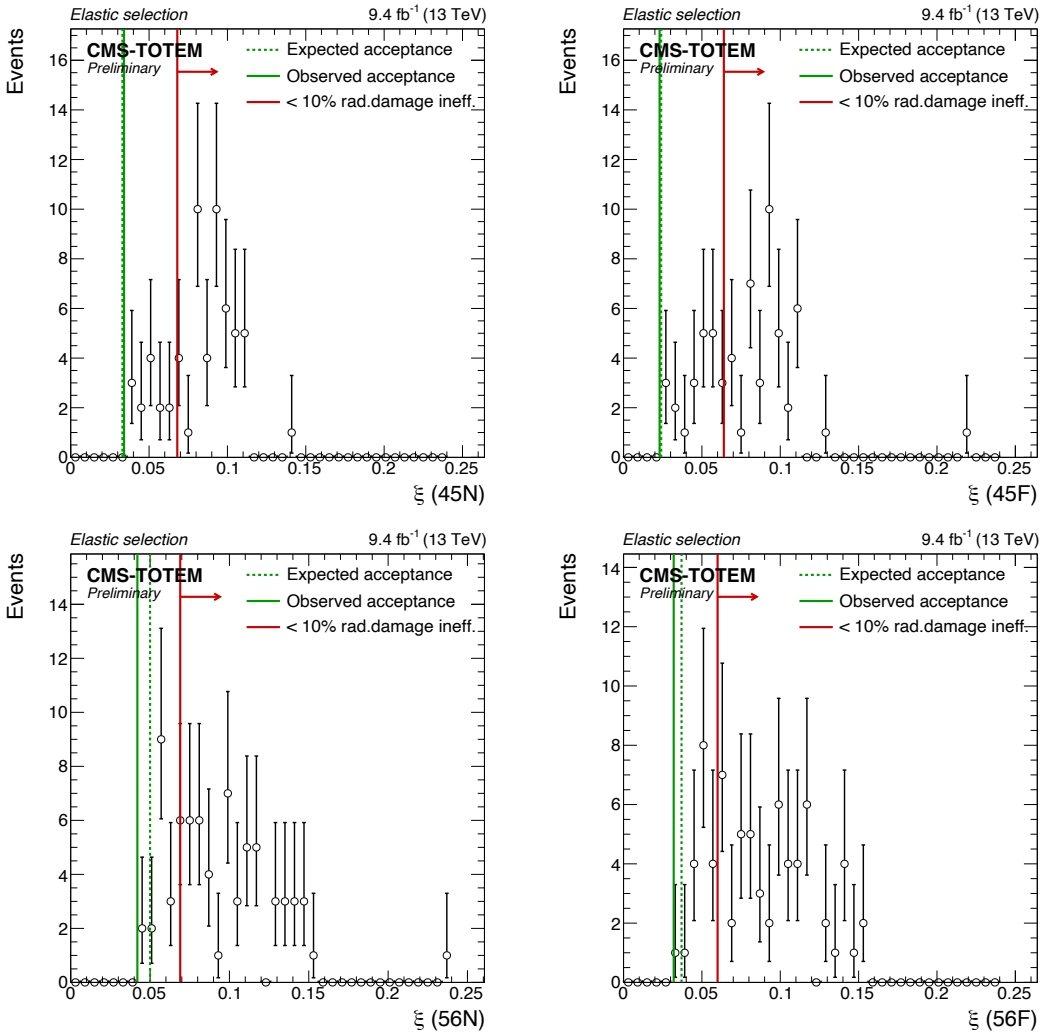

Figure 3.25: Longitudinal forward tracks' momentum loss distribution for the two pots of sector 45 (top row) and 56 (bottom row) for events with a diphoton candidate following the selection defined in the text. The solid green limits are depicting the individual pot acceptance as observed from the technique used in Section 3.4.2. The red line shows the region for which the radiation damage was observed to be below 10%.

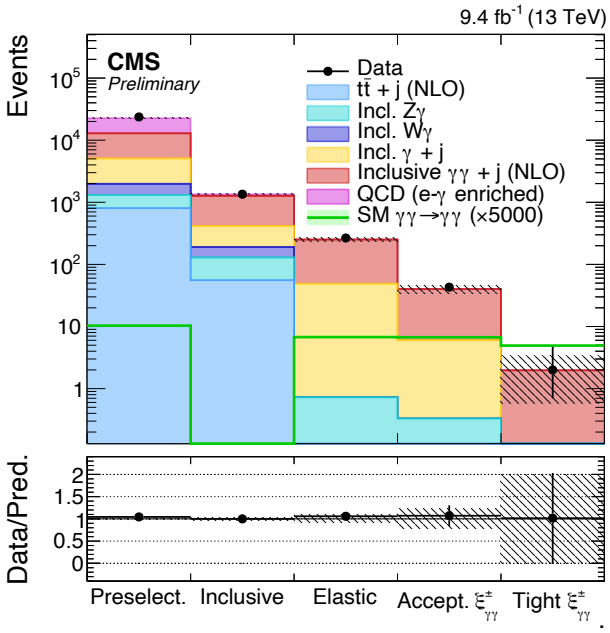

Figure 3.26: Number of simulated and observed events falling in all sideband and signal regions described in this section. All selections described in this figure are made in the diphoton system only. The color scheme of all samples may be found in all other plots above.

The missing diproton mass and rapidity can be expressed as a function of the two opposite-arm longitudinal momentum losses as shown in equation 1.5. Therefore, the uncertainties on the diphoton missing mass and rapidity can be expressed as the following quadrature sums:

$$\frac{\delta m_{pp}}{m_{pp}} = \delta y_{pp} = \frac{1}{2} \frac{\delta \xi_p^+}{\xi_p^+} \oplus \frac{\delta \xi_p^-}{\xi_p^-} \quad . \tag{3.4}$$

Here, we use the CMS conventions to define the positive and negative sides of the spectrometer. The CMS to LHC/TOTEM convention correspondence is the following:

- CMS positive z is LHC sector 4-5,
- CMS negative z is LHC sector 5-6.

With 9.4 fb^{-1} collected at 13 TeV with the PPS strips detectors in 2016, 22 exclusive diphoton candidates are selected with at least one track in the computed acceptance of silicon strips sensor on each side. The diphoton/diproton mass ratio and rapidity difference for the events are shown in Figure 3.27. The mass ratio plot has a asymmetric distribution as expected because of the fact that the diphoton mass is less than the missing mass, which is effectively the "total" mass.

This matching can be seen in two dimensions in the scatter plots for both 2 and 3σ matching in Figure 3.28.

Among these candidates, none have a diphoton system mass compatible at 2σ with the two-forward tracks system's. One has compatible rapidities. No diphoton candidates are found to be compatible at 2σ in both mass and rapidity with the forward tracks.

At 3σ, one event matching in mass and rapidity is observed. The kinematic properties

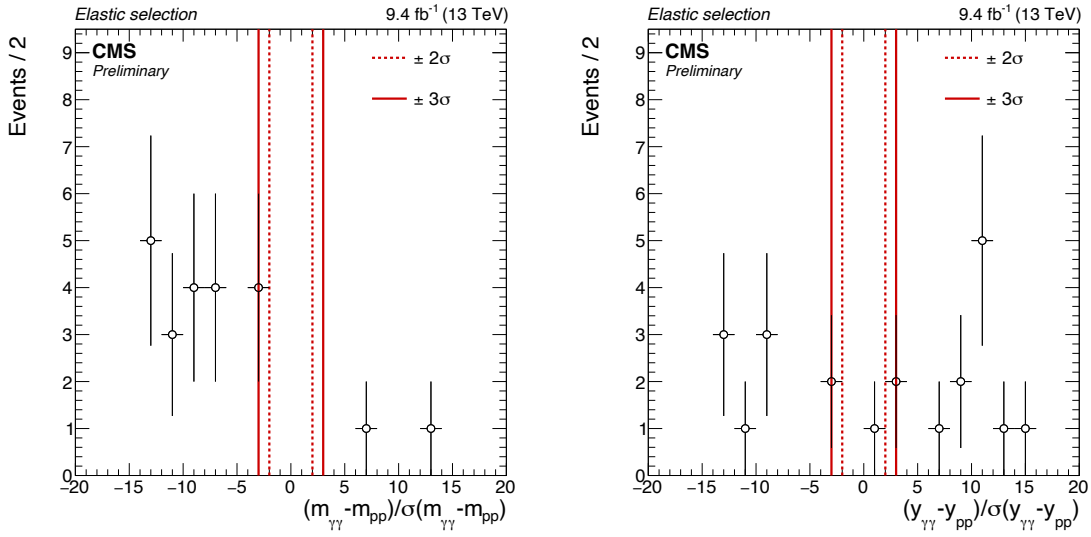

Figure 3.27: For the 22 diphoton candidates with at least two forward protons reconstructed in each arm acceptance, pull distributions between the diphoton invariant mass and the diproton missing mass (left), and the diphoton/diproton rapidities (right). The two quantities are normalized to the absolute error on the difference (sum in quadrature of the central and forward systems' uncertainties). Also overlaid are the 2σ and 3σ deviations bands.

	System	
	$\gamma\gamma$	pp
mass (GeV)	640.3 ± 12.8	733.8 ± 41.6
rapidity	−0.378 ± 0.028	−0.450 ± 0.057

Table 3.11: Central and forward kinematic information for the event with both systems matching at 3σ.

of this event are shown in Table 3.11.

3.5.3 Search region with less than 10% radiation damage

In Figures 3.29, 3.30 and 3.31, several kinematics distributions are shown for the final search region in which less than 10% radiation damage (see Section 3.4.3) was observed in forward strips detectors. Using only this chosen ξ region (as listed in Table 3.9), only 2 diphoton events remain instead of the 22 referenced above.

This selection does not yet define any matching between central two-photon and forward two-proton systems. This is the selection that will be used for the rest of the analysis.

A 6.2% deficit compatible within uncertainties is observed between the 2 events observed in data and an expected 2.11 + 0.96 - 0.66 (stat) background events yield. In this tighter region, a total of 1×10^{-3} SM exclusive $\gamma\gamma \to \gamma\gamma$ signal events are expected.

To summarize, we have defined three regions of interest in this note.

1. Elastic selection ("loose" elastic selection): defined with acoplanarity < 0.005 only, no $\xi_{\gamma\gamma}$ selection, and no RP information.

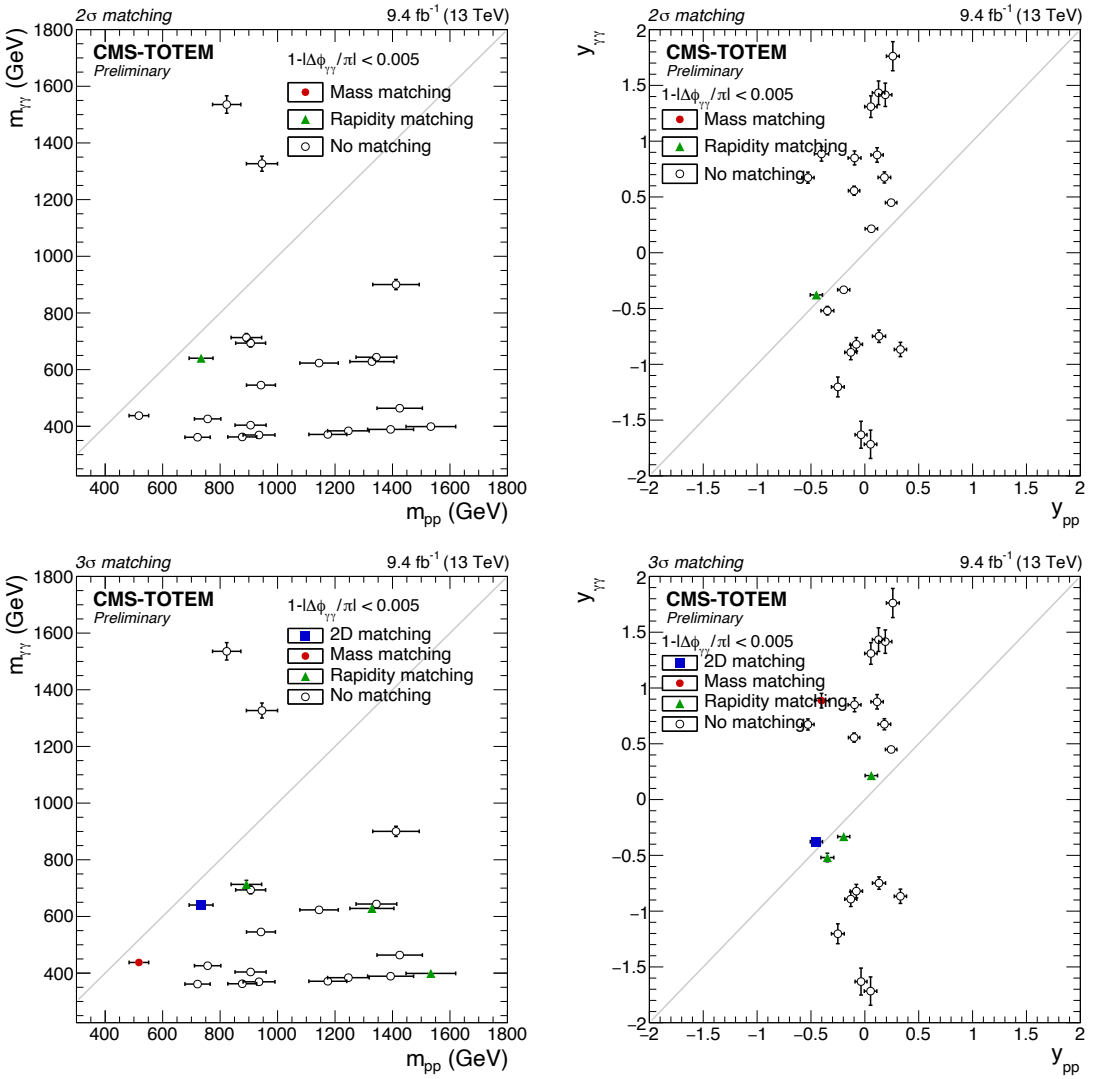

Figure 3.28: Balance between the diproton missing mass and the diphoton invariant mass (lhs. figure), and the diproton and diphoton rapidities (rhs. figure), for events with double tagging at 2σ (top figures), and 3σ (bottom figures).

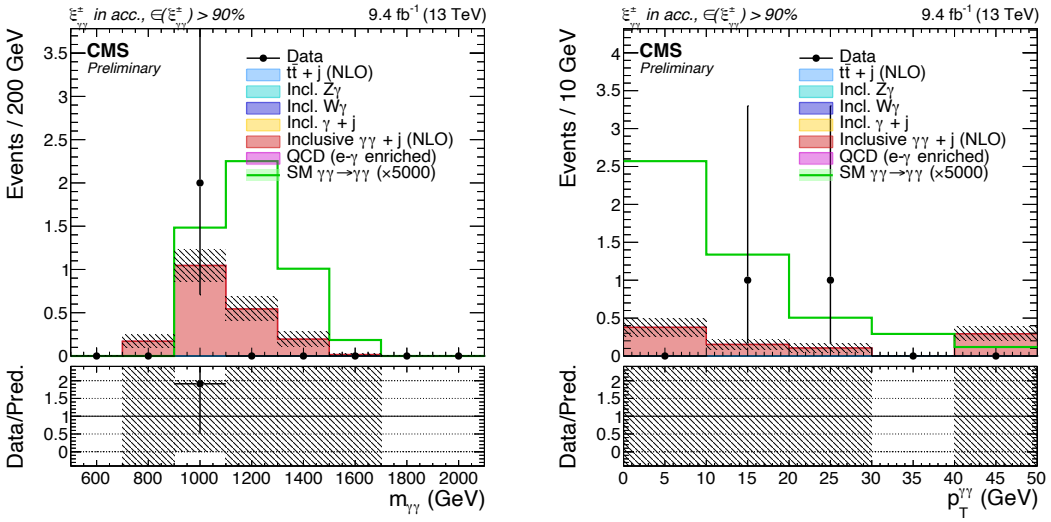

Figure 3.29: Distributions of the diphoton invariant mass and transverse momentum spectra in the signal search region with $\xi_{\gamma\gamma}$ within the pots acceptance (and for the PPS strips having less than 10% radiation damage).

2. Elastic selection + pots acceptance: same as above with the addition of $\xi_{\gamma\gamma}$ within the observed pots acceptance (different minimum value per pot, but maximum value of 0.15 for all pots).
3. Elastic selection + "tight" pots acceptance: same as 2 with $\xi_{\gamma\gamma}$ within the range such that radiation damage $< 10\%$.

   The final limits will be extracted from this last region as discussed in a later section.

3.5.4 Background estimations

After all selection criteria discussed in the previous sections, backgrounds come mainly from inclusive diphoton events in coincidence with proton tracks from unrelated pileup interactions. Given the large uncertainties associated to diffractive and non-diffractive events production and the lack of a proper simulation of the full effects of proton propagation through the LHC beamline, a toy experiment is performed to estimate this accidental background contribution in the signal search region.

To create the toy experiment, a pseudo-event is defined by the mixing of protons taken from the same data sample as the selected events with a random diphoton kinematics sampled from the templated fit performed in the inclusive-enhanced selection of data observed in Section 3.3.3.

The background contributions for the 2 and 3σ mass/rapidity matching windows is estimated by mixing simulated diphoton events with protons from data. This process for calculating the expected background coming from an accidental matching is equivalent to the one developed for single-arm tagging in [60].

For the final estimate of the accidental matching events, the total number of events from the toy simulation is normalized to the number of events from the MC passing the central selection. Therefore, the background estimate needs to be corrected for the fraction of events passing the central selection but not containing at least one forward

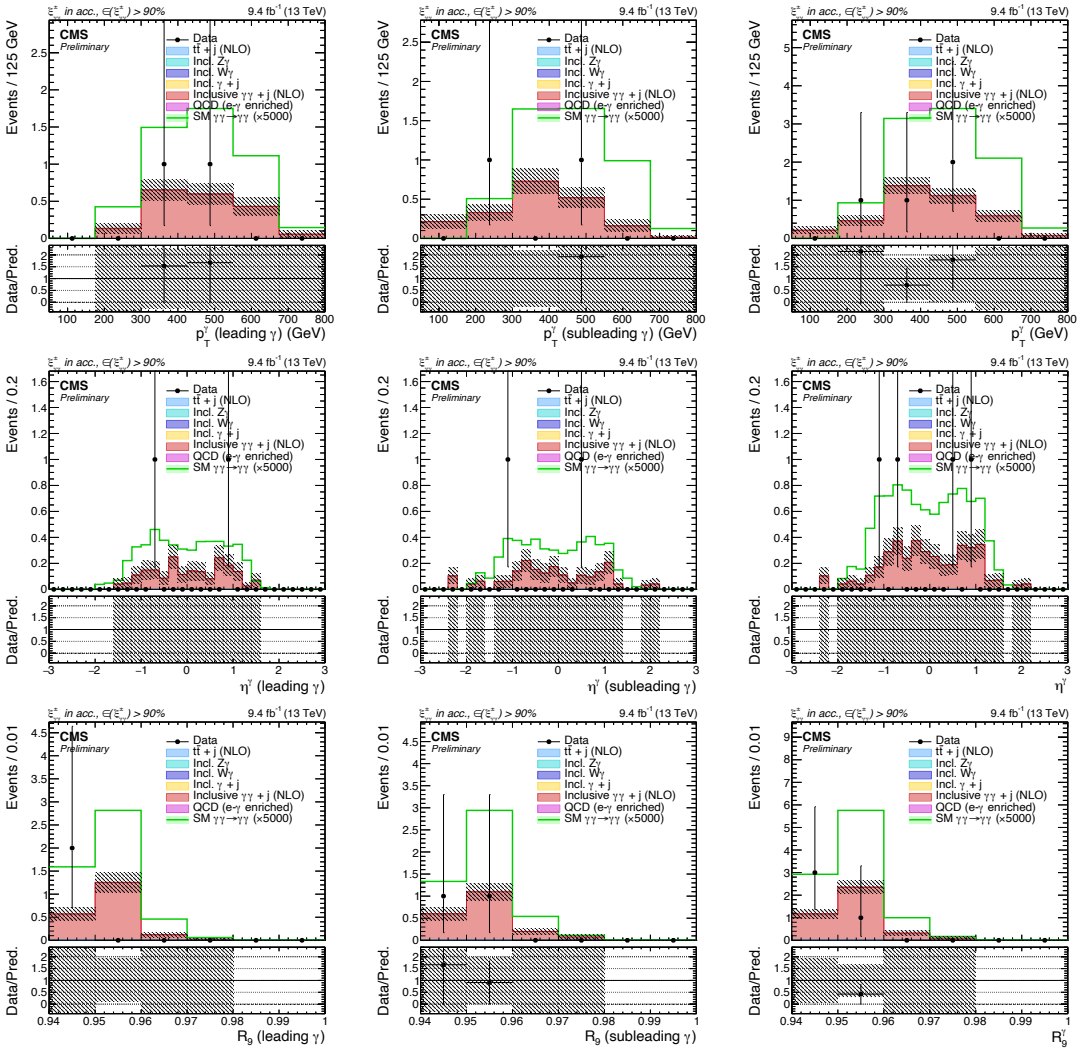

Figure 3.30: Single photon distributions for the elastic search + tight pots acceptance region defined in the text.

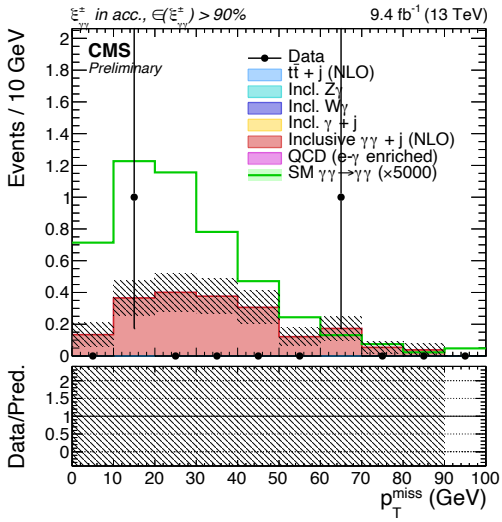

Figure 3.31: Total missing transverse energy for events with a diphoton system passing the elastic selection and with a $\xi_{\gamma\gamma}$ within the pots acceptance (with less than 10% radiation damage).

proton track. This fraction of events without any proton tracks reconstructed in RPs is obtained from data, and evaluated at 53% .

In Figure 3.32 the mass and rapidity distributions generated for 500k "toys" are pictured, along with the 1, 2 and 3σ limits.

As an extra check, another fitting function is used to evaluate the modeling dependence of this accidental backgrounds contribution. Using

$$f(\xi) = p_0 e^{-p_1/\xi^2},$$

we obtain numbers compatible with the $1-\sigma$ band of the previous template, resp. 0.884(2), 0.249(1), and 0.456(2) events where the central two-photon and forward two-proton systems are unmatched, matched at 2-σ, and at 3-σ.

Matching window	Bck.yield	min(1σ)	max(1σ)
unmatched	0.833(3)	0.676(3)	1.109(3)
2σ	0.231(1)	0.192(2)	0.314(2)
3σ	0.429(2)	0.350(2)	0.571(2)

Table 3.12: Summary of combinatorial, “accidental” inclusive background contributions, and candidates matching both in mass and rapidity at 2 and 3σ. Last two columns represent the minimum and maximum of these yields obtained from 100 replicas of 100k events with the $\xi_{\gamma\gamma}$ fit results for the inclusive control region varied over the 1 standard deviation ellipse shown in Figure 3.11. The matching is considered only for the regions of ξ such that the strips radiation damage is under 10%. Errors quoted in parenthesis are statistical only.

The pileup dependency of this background estimation procedure is estimated running the same workflow using three parameterizations of $\xi^{\pm}_{\gamma\gamma}$ extracted in three bins of the event vertex multiplicity: $0 < n_{\text{vtx}} \leq 15$, $15 < n_{\text{vtx}} \leq 25$, and $n_{\text{vtx}} \geq 25$. As observed in

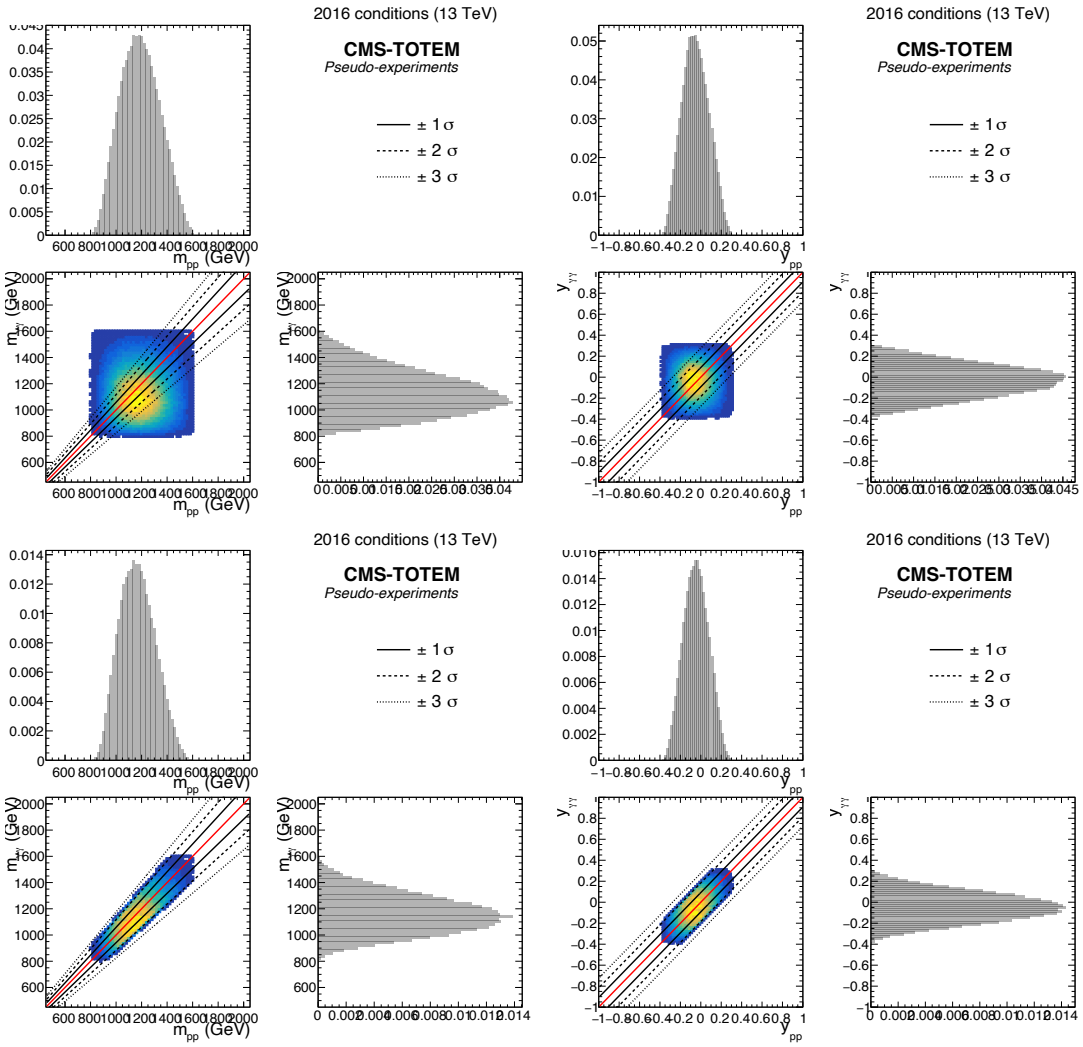

Figure 3.32: Mass and rapidity correlation without (top row) and with a 2σ correlation in mass and rapidity (bottom row), for 500k toys generated as described in the text. 1, 2, and 3σ deviation bands are overlaid to both distributions. For each 2D plot, the 1D projections are shown for the diphoton and diproton systems.

Table 3.13, the values obtained following the three templates agree within a few percent and their differences are fully covered by the systematic uncertainties quoted for the full procedure. This ensures a good stability of the method both for the central and forward systems.

Matching window	$0 < n_{\text{vtx}} < 15$	$15 < n_{\text{vtx}} < 25$	$n_{\text{vtx}} > 25$
unmatched	0.832(3)	0.832(3)	0.832(3)
2σ	0.228(1)	0.232(1)	0.231(1)
3σ	0.424(2)	0.427(2)	0.426(2)

Table 3.13: Inclusive background contribution for the various matching windows, for three slices of vertices multiplicity (or pileup condition), as described in the text.

A summary of the selection stages and their background rejection may be found in Table 3.14.

Selection criteria	Data	SM LbL	$\gamma\gamma + j$	Oth.incl.back.
HLT + preselection	23,650	0.00206	7810.6	14849.4
Elastic	266	0.00135	202.4	49.0
$\xi_{\gamma\gamma}$ in pots acc.	43	0.00134	34.1	6.0
$\epsilon_{\text{rad}}(\xi_{\gamma\gamma}) > 90\%$	2	0.00099	2.0	negl.

Table 3.14: Cut flow summary for the exclusive diphoton candidates selection.

3.5.5 Systematic uncertainties

The following sources of systematic uncertainties are considered:

- A 37% nuisance is assigned to the overall method to extract the yield correction for the inclusive control region (see Section 3.3.3 and Appendix A for the procedure).
- an accidental background uncertainty evaluated as the maximal envelope size when the inclusive $\xi_{\gamma\gamma}$ distribution fit is varied by ± one standard deviation; this corresponds to another 33% systematic uncertainty source.
- A 13% uncertainty is assigned to the radiation damage and multi-tracking inefficiencies of the PPS strips detectors, also accounting for cases in which a proton can be observed in only one of the two pots, in both arms.
- the uncertainty on the CMS recorded luminosity for the run ranges considered; it is taken as the same evaluated for the whole 2016 data taking period, hence 2.5% [39].
- finally, a 10% uncertainty on the signal cross section is accounted for. This covers the total uncertainty on the proton survival factor for two-photon processes around the electroweak energy scale, as previously evaluated in e.g. [69] for the $\gamma\gamma \to \mu^+\mu^-$ process.

3.5.6 Limit calculation

To calculate the upper limit on anomalous quartic gauge couplings, we use the version 7.0.12 of CMS Higgs "combine" tool [77].

We use a LHC-style profile likelihood ratio as test statistic, and systematic uncertainties are accounted for as nuisance parameters with a log-normal prior. Given the background yields observed in Table 3.12, an observed hybrid bayesian-frequentist upper limit of 2.795(42) events is computed using the LHC-style parameterization of the HybridNew method. This limit may be converted into observed upper limits on the production cross section:

$$\sigma = \frac{N}{(\epsilon \times A) \times \mathcal{L}}$$

where N is upper limit observed for signal events as quoted above, and $(\epsilon \times A)$ the efficiency times acceptance for the overall signal selection. This latter is evaluated to be 9.3% for an elastic SM-like signal sample generated with FPMC, using $0.07 < \xi_p < 0.111$, $0.07 < \xi_p < 0.138$ for sectors 45 and 56 respectively, and $p_T(\gamma) > 75$GeV. This term accounts for the 21.1% CMS selection efficiency, 30% multi-tracking inefficiency in each arm, and 10% radiation damage at most for PPS strips detectors. At 95% CL, the upper limit on the exclusive LbL cross section in the kinematic range quoted above is found to be:

$$\sigma(pp \to p\gamma\gamma p | \xi_p \in \xi^{\text{PPS}}) < 4.4 \text{ fb} \qquad 3.5$$

3.5.7 Limits on anomalous quartic gauge couplings

Given the upper limit on the LbL cross section within the fiducial cuts defined above, corresponding limits can be extracted on anomalous exclusive diphoton production mechanisms.

An upper limit is set on the partial cross section for $pp \to p\gamma\gamma p$ with $E_T^\gamma > 75$ GeV, $|\eta^\gamma| < 2.5$ and $\xi_{\gamma\gamma}^{\pm}$ within PPS strip detectors acceptance (and ξ_p such as the radiation damage observed in these detectors is $< 10\%$).

To probe the two-dimensional space of ζ_1 vs. ζ_2, the theoretical cross section estimates were scanned using the FPMC generator interfaced to Pythia 8 over the parameters range of interest. The same phase space cuts as applied on the SM signal selection are defined for the selection efficiency.

In this study, 20 anomalous samples of approximately 5000 events were produced with the same pileup conditions as used for all other signal and background samples.

As illustrated in Figure 3.33, the various diphoton kinematics distributions – and hence selection efficiency – do not vary strongly between the coupling parameters ζ_1 and ζ_2 within the acceptance.

In this study, a constant CMS selection efficiency of $63.8\% \pm 1.7\%$ is set for the whole anomalous parameters range of interest. To reiterate, the selection efficiency is much lower for the SM LbL process that is most prevalent at lower masses. The overall $\epsilon \times A$ factor is calculated to be 14.5% accounting for the 63.8% CMS selection efficiency, 30% multi-tracking inefficiency in each arm, 51.4% signal efficiency in the asymmetric ξ range, and 10% radiation damage for the PPS detectors.

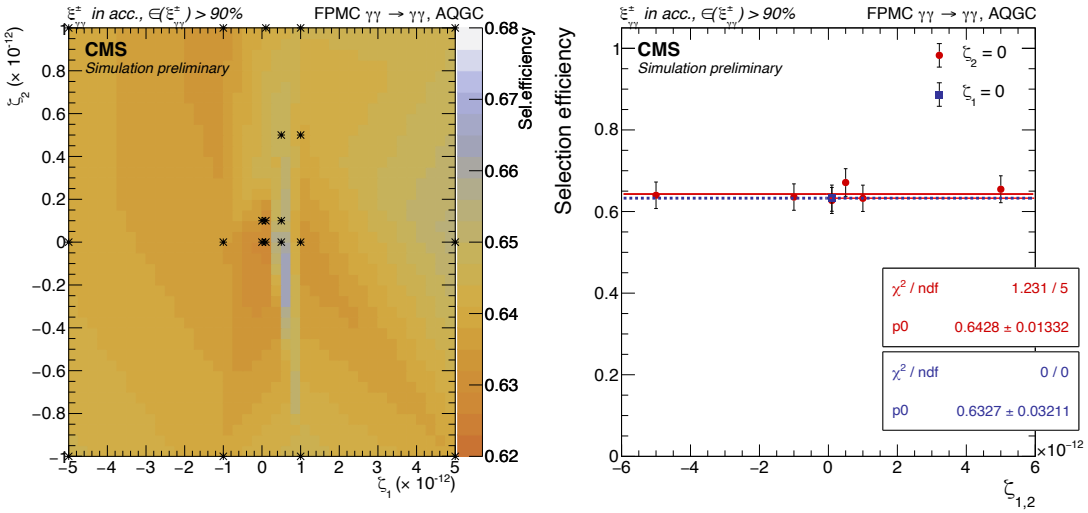

Figure 3.33: Left: efficiency for the "tight ξ" elastic selection (where at most 10% radiation damage is expected in the PPS strips detectors), as a function of the two AQGC parameters for EFT extension of the LbL process. Efficiencies are interpolated from parameters values marked by stars on the two distributions. Right: efficiency for the same selection as a function of the two AQGC parameters when the other is set to 0.

The observed (expected) results are

$$\sigma^{fid}_{prod} < 2.079(2.488) \text{ fb}. \tag{3.6}$$

The AQGC cross-section follows a family of ellipses in the ζ_1, ζ_2 plane described by the equation

$$\sigma = A\zeta_1^2 + B\zeta_1\zeta_2 + C\zeta_2^2 \tag{3.7}$$

where A, B, and C are constants in the proportions described in equation 2.5 in Reference [22].

Once one cross-section is known in the ζ_1, ζ_2 plane, every other point can be calculated analytically. Using the one FPMC AQGC sample generated within the fiducial volume having $\zeta_1 = 5{\times}10^{-13}$, $\zeta_2 = 0$, and $\sigma = 6.25$ fb, the constant A can then be found can be found using the following relation:

$$A = \sigma/\zeta_1^2 \tag{3.8}$$

Using the proportions of 48, 40, and 11 for A, B, and C, respectively, we then get the full equation for the analytical conical form:

$$\sigma(\zeta_1, \zeta_2) = 2.5001 \times 10^{25} \cdot \zeta_1^2 + 1.0417 \times 10^{25} \cdot (2 \times \zeta_1\zeta_2) + 6.5902 \times 10^{24} \cdot \zeta_2^2.$$

This equation has been validated by confirming that it gives the same cross-section as FPMC for various points in the (ζ_1, ζ_2) plane.

This equation may be used to derive the limits on each coupling parameter separately

by setting the other to zero.

$$|\zeta_1| < 2.88 \times 10^{-13}\ \text{GeV}^{-4} \quad (\zeta_2 = 0)$$
$$|\zeta_2| < 6.03 \times 10^{-13}\ \text{GeV}^{-4} \quad (\zeta_1 = 0)$$

The observed and expected limits are shown in Figure 3.34.

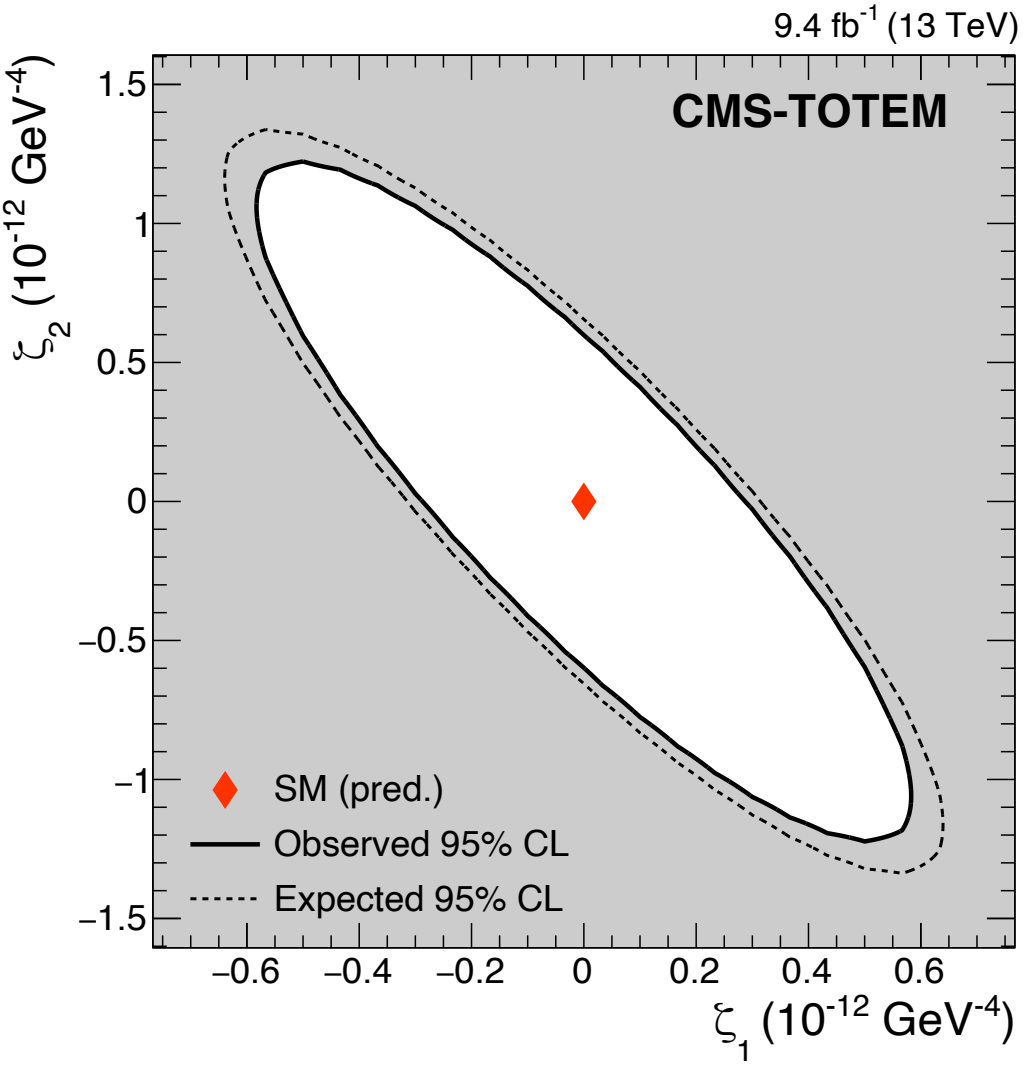

Figure 3.34: Two-dimensional limits on AQGC anomalous diphoton production mechanisms given the upper limit observed on production cross section.

Chapter 4: Search for exclusive diphoton events using the full Run 2 dataset

Contents

A search for high-mass exclusive diphoton production via photon-photon fusion with intact protons is presented. The analysis utilizes 102.7 fb^{-1} of data collected by the CMS and PPS detectors in the full Run II dataset at $\sqrt{s}$ = 13 TeV. Events are selected with each photon having a $p_{\text{T}} > 100$ GeV, a diphoton mass > 350 GeV, and having opposite-side protons within the asymmetric acceptance $0.035 < \xi < 0.15$ (0.18) for sector45 (sector56). The diphoton system is then required to satisfy an acoplanarity selection with $a < 0.0025$. Using proton tagging techniques from the CMS Precision Proton Spectrometer, final state intact protons from the corresponding photon-exchange event can be measured to remove the dominant backgrounds. In addition to different transverse momentum and proton ξ selections with respect to the previous analysis, a more robust photon ID, completely data-driven background estimation procedure, and shape-based limits are utilized. One-dimensional limits are derived on the four-photon

anomalous coupling parameters for $\zeta_1 < 7.26\times10^{-14}$ GeV^{-4}, $\zeta_2 < 1.52\times10^{-13}$ GeV^{-4}. Finally, the strongest limits to-date are placed on Axion-Like Particle production in the fiducial volume of this search.

4.1 Datasets

The samples used in this study include LHC data collected by the CMS experiment in 2016, 2017, and 2018 as well as inclusive background MC samples and signal samples modeling AQGCs and ALPs.

4.1.1 Data samples

Ers	**Run Range**	$\mathcal{L}$ **fb**$^{-1}$
Run 2016 B	273725–275376	4.55
Run 2016 C	275657–275931	1.58
Run 2016 G	279766–280385	3.65
	Total	9.78

Table 4.1: Data samples, run ranges, and luminosity used in this analysis for the 2016 data taking year.

Era	**Run Range**	$\mathcal{L}$ **fb**$^{-1}$
Run 2017 B	297023–299330	2.3609
Run 2017 C	299359–302045	8.5772
Run 2017 D	302111–302679	4.0748
Run 2017 E	303708–304798	8.9597
Run 2017 F	305016–306462	13.2199
	Total	37.2198

Table 4.2: Data samples, run ranges, and luminosity used in this analysis for the 2017 data taking year.

Era	**Run Range**	$\mathcal{L}$ **fb**$^{-1}$
Run 2017 A	297023–299330	12.1038
Run 2017 B	299359–302045	6.7859
Run 2017 C	302111–302679	6.5297
Run 2017 D	303708–304798	30.2966
	Total	55.7161

Table 4.3: Data samples, run ranges, and luminosity used in this analysis for the 2018 data taking year.

The data used in this analysis corresponds to the LHC runs where both the CMS and PPS detectors were fully operational. For the 2016 data taking period, data is only used from eras B, C, and G (same as in Chapter 3) corresponding to runs when the PPS detectors were part of the data acquisition as shown in Table 4.1. The gap between eras C and G correspond to a period where radiation damage to the PPS strip detectors caused the efficiency to drop drastically. For the data taking years of 2017 and 2018, all CMS

eras are used in the analysis as shown in Tables 4.2 and 4.3, respectively. The luminosity of data recorded by PPS with respect to CMS for Run II can be seen in Figure 2.15.

The run ranges for the CMS eras are further divided by PPS based on the detector conditions. This is necessary for correct implementation of detector efficiencies. The PPS eras and the corresponding integrated luminosities used in the analysis can be found in Table 4.4.

PPS Era	**Run Range**	$\mathcal{L}$ **fb**$^{-1}$
2016 B1	272007–274286	0.64
2016 B2	274314–275386	3.91
2016 C	275657–276283	1.58
2016 G	278820–280385	3.65
2017 B	297020–299329	2.36
2017 C1	299337–300785	5.31
2017 C2	300806–302029	3.26
2017 D	302030–303434	4.07
2017 E	303435–304826	8.96
2017 F1	304911–305114	1.71
2017 F2	305178–305902	7.88
2017 F3	305965–306462	3.63
2018 A	315252–316995	12.10
2018 B1	316998–317696	6.38
2018 B2	318622–319312	0.40
2018 C	319313–320393	6.53
2018 D1	320394–322633	19.88
2018 D2	323363–325273	10.42
	Total	102.67

Table 4.4: The recorded luminosity for each PPS era and corresponding run ranges within the LHC Run II data-taking period.

The data format used for this analysis was developed by the author on behalf of the CMS collaboration. This marks the first time that protons have been integrated into the "NanoAOD" format – the recommended data format of CMS. Access to protons at this level allows for quick and convenient analysis techniques with minimal storage requirements.

4.1.2 Monte Carlo background samples

A complete list of the background samples used for the description of the selection regions is shown in Table 4.5.

All samples are reweighted for their corresponding pileup conditions and average energy density (`fixedGridRho`).

As in Chapter 3, the dominant background in all selection regions is the inclusive $\gamma\gamma$+jet(s) sample where "jet(s)" are loosely classified as any radiation of energy by the CMS MC nomenclature. This sample is modeled at NLO through the MadGraph5_aMC@NLO [63] package. The subleading $t\bar{t} + j$ and $V + \gamma$ samples are also modeled through the MadGraph5_aMC@NLO package where V represents a photon, W boson, or Z boson. The decay channel used in the aforementioned samples is $Z \to \ell^+\ell^-$ and $W^\pm \to \ell^\pm \nu_\ell$. To

estimate the QCD background, an electron and photon enriched QCD sample generated with PYTHIA 8 (CP5 tune) is also utilized. All background samples are listed in Table 4.5 along with the generated cross-section.

Sample	σ_{gen} **(pb)**
Incl. $\gamma\gamma$	118.0
Incl. γ	873.7
$Z\gamma$	55.47
$W\gamma$	191.1
$t\bar{t}$	815.96
QCD	117,500

Table 4.5: A list of the background samples used to describe the data as well as their generated cross-section. Different numbers of events are generated for each sample in each simulated data taking year.

The phenomenological studies in [22] are used as a reference for the main expected background processes where it is shown that the QCD contribution to the two-photon cross-section dies out quickly with increased diphoton masses. In fact, almost all backgrounds are diminished at high-diphoton masses. The remaining background contribution is discussed later in section 4.5.2.

4.1.3 Signal samples

LbL signal samples are generated using the Forward Physics Monte Carlo (FPMC)[66] assuming collinear photon emission from both incoming protons. The photon fluxes from proton are modeled using the Budnev et al. parameterization. For the simulated conditions of each data taking year, multiple signal samples are generated with various ζ_1 and ζ_2 values. One SM LbL sample is also generated for each year. These samples serve to derive the signal efficiency.

The signal is expected to exist at high diphoton mass, high p_T, and central η. Because the two final state photons are produced exclusively, they are expected to be back-to-back with respect to the azimuthal angle ϕ. These characteristics are evident in Figure 4.1 where the 2017 samples are shown as an example.

Another model that is considered is the s-channel exchange of an Axion-Like Particle (ALP). In this case, the main parameters of interest are the mass of the particle and the coupling constant,f^{-1}, describing the coupling to the four photons. Multiple samples are also generated for each year having various ALP masses ranging from 500 GeV to 2000 GeV. For the analysis discussed in Chapter 3, the luminosity and acceptance did not provide sufficient sensitivity to this process with respect to previous LHC studies.

Kinematics for various ALP masses are shown in Figure 4.2 for the 2017 CMS pileup conditions as an example. Distributions of the observables do not change with varying values of f^{-1}, so only one value for the coupling strength is used. In the ALP diphoton mass plot, the sample with m = 2000 GeV has a different distribution due to the requirements placed on the ξ variable at generator level ($0.035 < \xi < 0.18$).

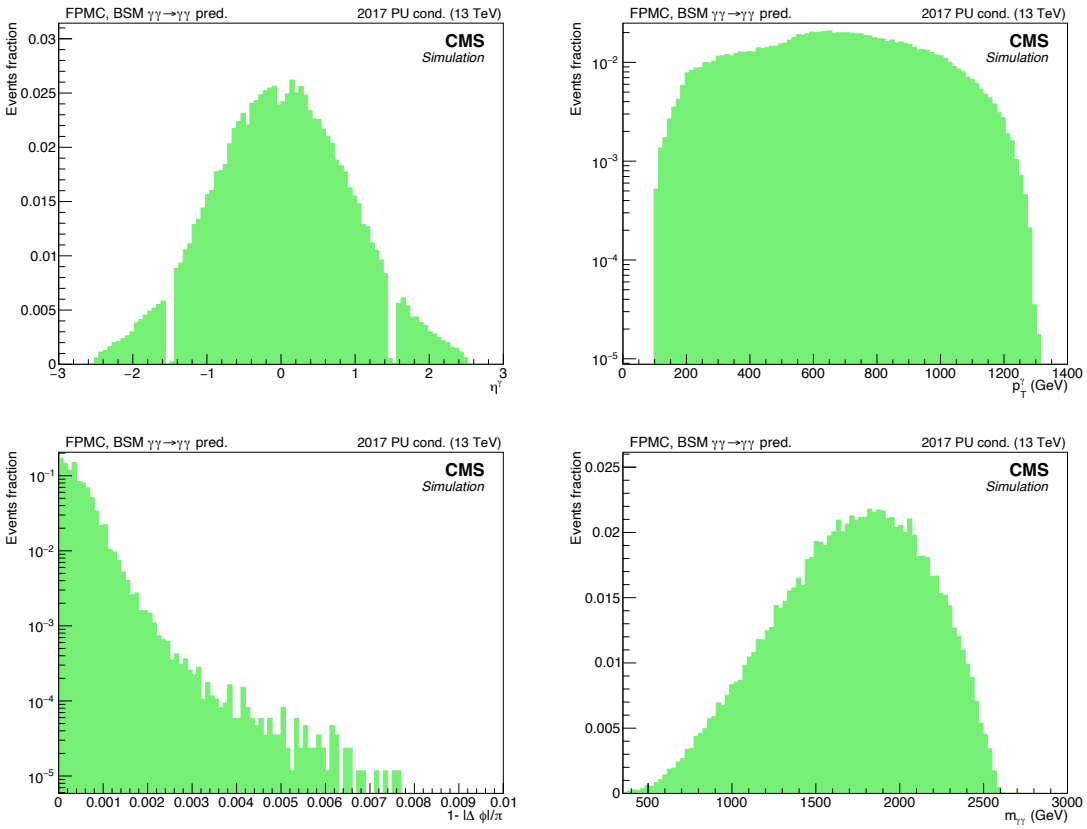

Figure 4.1: Anomalous coupling signal kinematics for the single photon η (top left), single photon p_T (top right), diphoton acoplanarity (bottom left), diphoton mass (bottom right). The signal simulation shown here is generated with FPMC for an Anomalous Quartic Gauge Coupling signal using $\zeta_1 = 10^{-12}$, $\zeta_2 = 10^{-12}$. The distributions represent the signal sample after undergoing the full CMS detector response. The simulated samples are shown for the 2017 CMS pileup conditions.

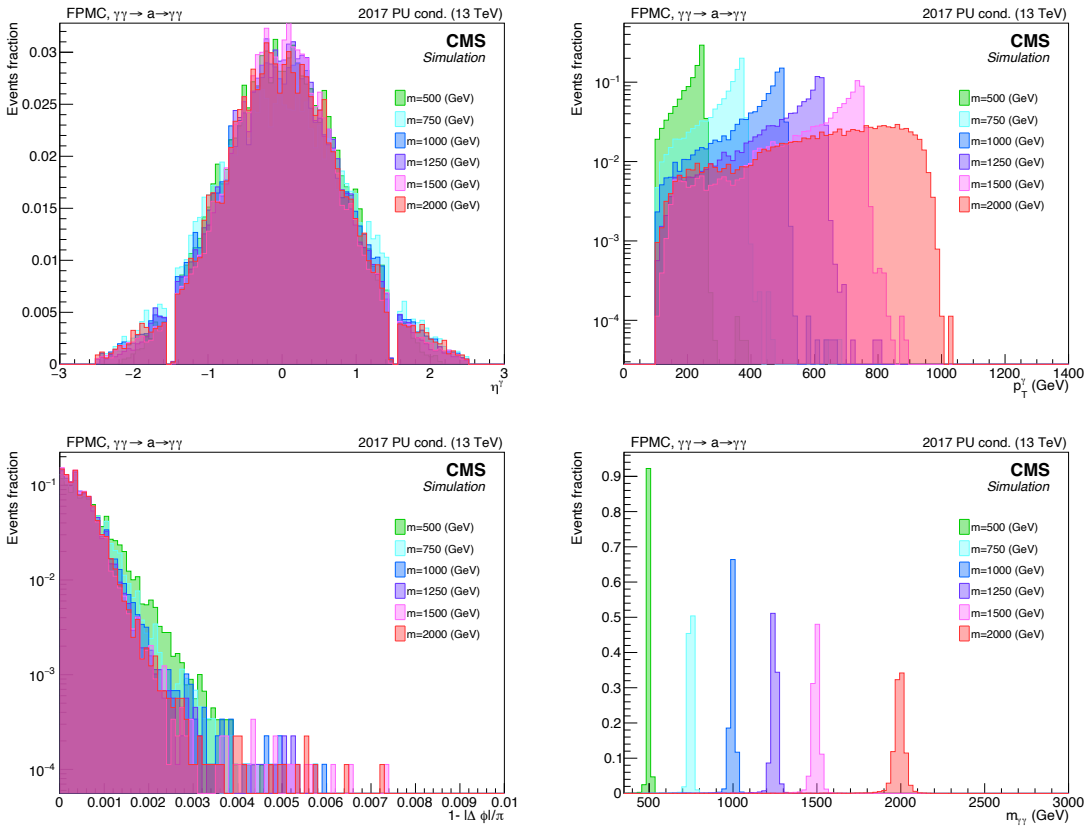

Figure 4.2: ALP signal kinematics for the single photon η (top left), single photon p_T (top right), diphoton acoplanarity (bottom left), diphoton mass (bottom right). All samples shown here are generated with FPMC for an Axion-Like Particle signal using $f^{-1} = 10^{-1} TeV^{-1}$. The distributions represent the signal sample after undergoing the full CMS detector response. The simulated samples are shown for the 2017 CMS pileup conditions.

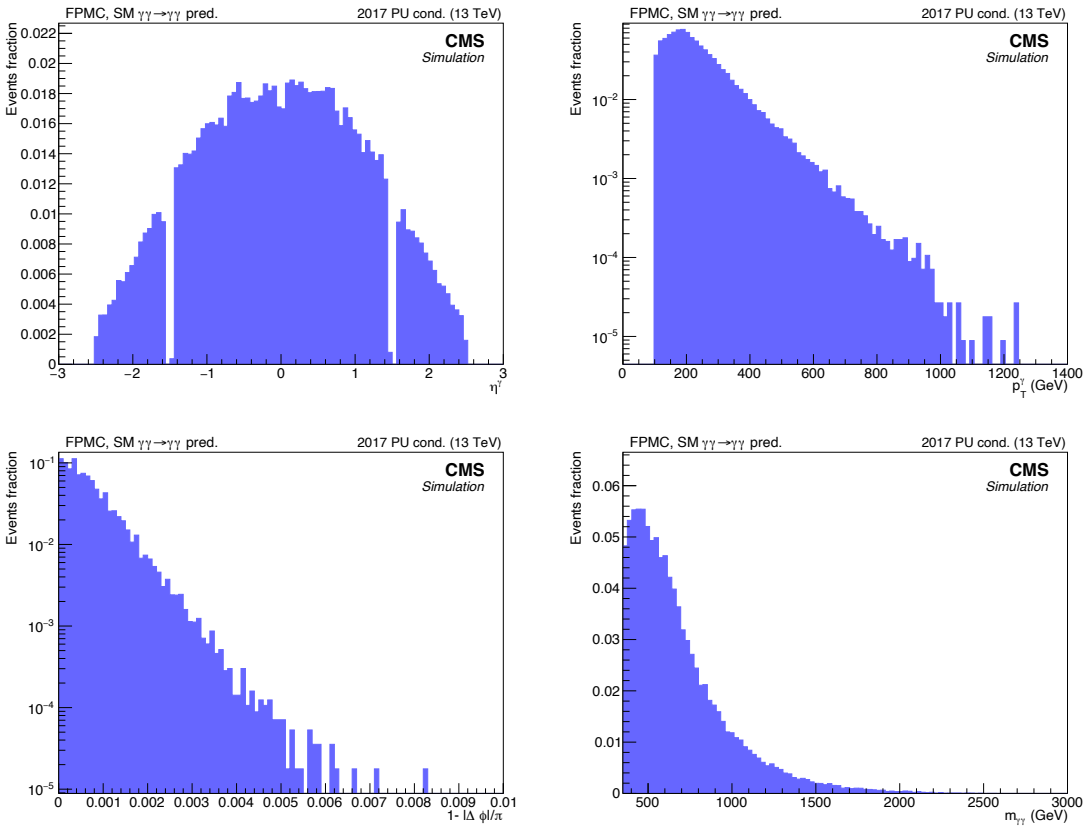

Figure 4.3: Kinematics for the single photon η (top left), single photon p_T (top right), diphoton acoplanarity (bottom left), diphoton mass (bottom right). All samples shown here are generated with FPMC for the SM LbL. The distributions represent the signal sample after undergoing the full CMS detector response. With respect to the anomalous coupling signal, the SM LbL events are expected at lower masses and transverse momenta. The simulated samples are shown for the 2017 CMS pileup conditions.

The kinematics for the SM LbL process can be seen in Figure 4.3 for the 2017 pileup conditions as an example. The contrast between the $p_T{}^{\gamma}$ and $m_{\gamma\gamma}$ is noted between the BSM kinematics and the SM kinematics.

Samples are shown for the 2017 UL reconstruction conditions. The distributions for the other data taking years are essentially identical.

4.2 Photon identification

Various photon identification (ID) recipes developed by the CMS collaboration were tested in this analysis to attain the best signal efficiency. For this study, the AQGC signal samples described in section 4.1.3 were used for testing the performance of each ID.

A multivariate analysis (MVA) utilizing a boosted decision tree (BDT) [78] is chosen for identifying and isolating photons. This technique allows for the definition of a single discriminating variable for each photon candidate that is based on many variables that help discriminate prompt photons from backgrounds. The inputs into the BDT are shower shape variables, isolation variables, and quantities based on the shower and isolation of pileup present in the event [53], each of which are described here. The $\sigma_{i\eta i\eta}$ variable is the spatial second-order moment of the photon candidate with respect to the angle η [53]. The R_9 variable is calculated as the sum of the energy contained by the 3×3 centered on the most energetic crystal in the supercluster divided by the supercluster energy. The $cov_{\eta}\phi$ variable is the covariance of the single-crystal values in η and ϕ for the 5×5 array of crystals centered on the highest energy crystal. The S_4 variable is the energy contained by the most energetic 2×2 array of crystals (containing the seed crystal) divided by the energy of the supercluster. The BDT also considers the η and ϕ width of the electromagnetic shower. The photon isolation variables that are considered are based on the PF algorithm. The Iso_{γ}, Iso_{chg}, and Iso_n are obtained by summing the transverse momenta of the photons, charged hadrons, and neutral hadrons, respectively, inside an isolation region of radius ΔR in the (η,ϕ) plane around the photon candidate [53]. Other variables used as inputs are the raw supercluster energy and supercluster η of the photon candidate as well as the average energy density of the event. Specifically for photon candidates in the endcap, the preshower σ_{η} and preshower energy divided by the supercluster energy are inputted to the decision tree.

The BDT is trained on simulated $\gamma + j$ events. The photon candidates are required to pass a preselection of criteria. The criteria are specific to each of the four categories that the photon candidate can belong to based on its location and R_9. The preselection cuts are shown in Table 4.6 where Iso_{trk} is the tracker hollow cone isolation defined as the sum of the transverse momenta of all tracks inside a cone around the photon candidate.

A working point (WP) can be defined where the BDT output gives a signal efficiency of 90% for identifying photons. The corresponding BDT output for this WP90 is found to be -0.02 for EB photons and -0.26 for EE photons.

The MVA ID makes identification and isolation requirements on the physics object in the CMS ECAL, but makes no prediction about whether the particle is a photon or an electron. For this reason, an electron veto is needed. A conversion-safe electron veto

	H/E	$\sigma_{i\eta i\eta}$	R_9	Iso_γ	Iso_{trk}
EB & $R_9 > 0.85$	0.08	-	> 0.5	-	-
EB & $R_9 \leq 0.85$	0.08	< 0.015	> 0.5	< 4.0	< 6.0
EE & $R_9 > 0.9$	0.08	-	> 0.8	-	-
EE & $R_9 \leq 0.9$	0.08	< 0.035	> 0.8	< 4.0	< 6.0

Table 4.6: Preselection for events to be used as a training sample for the photon identification BDT.

(CSEV) is used to remove photon candidates that are actually electrons without removing converted photons. For the signal samples described in Section 4.1, the MVA WP90 ID is found to be 84.76% efficient, and the CSEV is found to be 96.20% efficient for signal photons passing the ID.

4.3 Event selection

In this section, the sequential event selection placed on the CMS diphoton system is described. It is important to note that the selection criteria differ slightly between the 2016 data taking period and the rest of the Run II period. The HLT triggers that are chosen for the analysis are discussed first. Then, a group of quality selections are described that are labeled as the preselection. Next, the elastic selection targeting exclusively produced photons is detailed. Lastly, the final signal selection region is derived.

4.3.1 HLT selection

For the data taken in the 2016 period, the `HLT_DoublePhoton60` trigger is requested to be fired as in Chapter 3.

Conversely, for the 2017 and 2018 data, the `HLT_DoublePhoton70` trigger is requested to be fired. The collaboration chose this trigger path to be the successor to the `HLT_DoublePhoton60` trigger described previously. In a similar way, this trigger requires the photon candidate to have transverse momentum greater than 70 GeV and H/E ratio below 0.15.

The efficiency of each of these triggers have been studied as a function of the photon transverse momentum and trigger-safe p_T selections are applied to the data. The efficiency of these triggers with respect to the `HLT_DoublePhoton33_CaloIdL` trigger can be seen in Figure 4.4. For the 2016 data, the trigger-safe p_T cut is placed at 75 GeV and, for the 2017 and 2018 data the p_T cut is placed at 100 GeV. Additionally, a trigger-safe H/E cut is required such that $H/E < 0.10$.

The HLT selection can be summarized by the chosen HLT trigger path and the trigger-safe selection criteria:

- `HLT_DoublePhoton60` (`HLT_DoublePhoton70`) for 2016 (2017-2018) data
- ${p_T}^\gamma > 75$ (100) GeV for 2016 (2017-2018) data
- $H/E < 0.1$

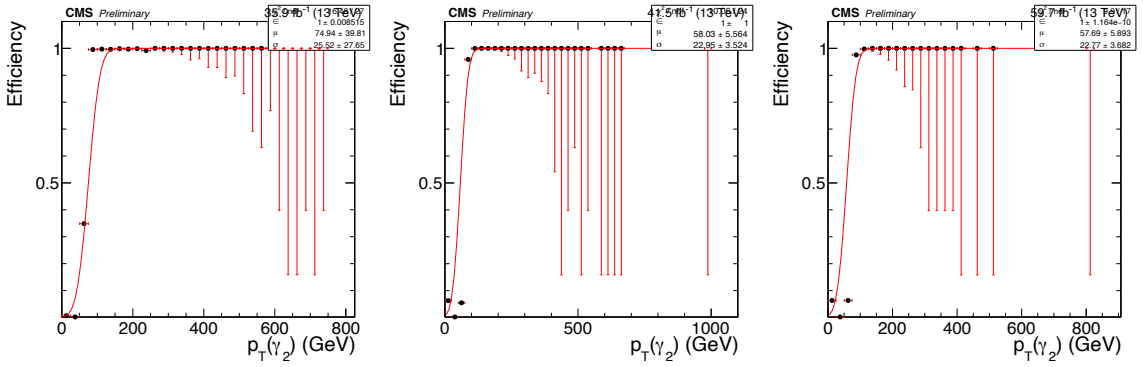

Figure 4.4: Study of the HLT_DoublePhoton60 (2016) and HLT_DoublePhoton70 (2017-2018) triggers with respect to the HLT_DoublePhoton33_CaloIdL trigger. The red line is a fit to the turn-on curve for the efficiency.

4.3.2 Preselection

Applied on top of the HLT selection, the preselection makes selection cuts to ensure quality of the selected events. To be sure that the electromagnetic objects selected by the trigger are photons, we use the recommended MVA working-point-90 (WP90) photon ID described in section 4.2. This algorithm does not distinguish between electrons and photons, therefore we also apply an electron veto to the photon candidates. This electron veto is said to be "conversion-safe" since it takes measures to not veto photons that have been converted. Furthermore, the single photon pseudorapidity is constrained in the region $|\eta^{\gamma}| < 2.5$, with an additional veto between ± 1.4442 and ± 1.566, corresponding to the ECAL transition region between the barrel and the endcaps. The last requirement of the preselection is that the mass of the diphoton pair be greater than the 350 GeV to avoid large contributions from SM backgrounds as motivated in [28].

The preselection can be summarized by the following:

- MVA WP90 Photon ID
- Conversion-safe electron veto
- $|\eta^{\gamma}| < 2.5$
- $m^{\gamma\gamma} > 350$ GeV

4.3.3 Elastic selection

In addition to the preselection, the elastic selection applies a singular and powerful cut to select purely exclusive events. The elastic selection is used for selecting the exclusive process of $\gamma\gamma \to \gamma\gamma$. In this special scattering process, the resulting photons are expected to be back-to-back with respect to the azimuthal angle ϕ providing a criterion from which truly exclusive events can be selected.

The variable of interest to define this selection is the *acoplanarity* between the two photons.

This selection results in the rejection of major inclusive backgrounds [22]. Signal events are expected to peak at very low acoplanarities, hence the selection cut is chosen to be $a < 0.0025$ as in Chapter 3. The kinematic distributions of events in this selection

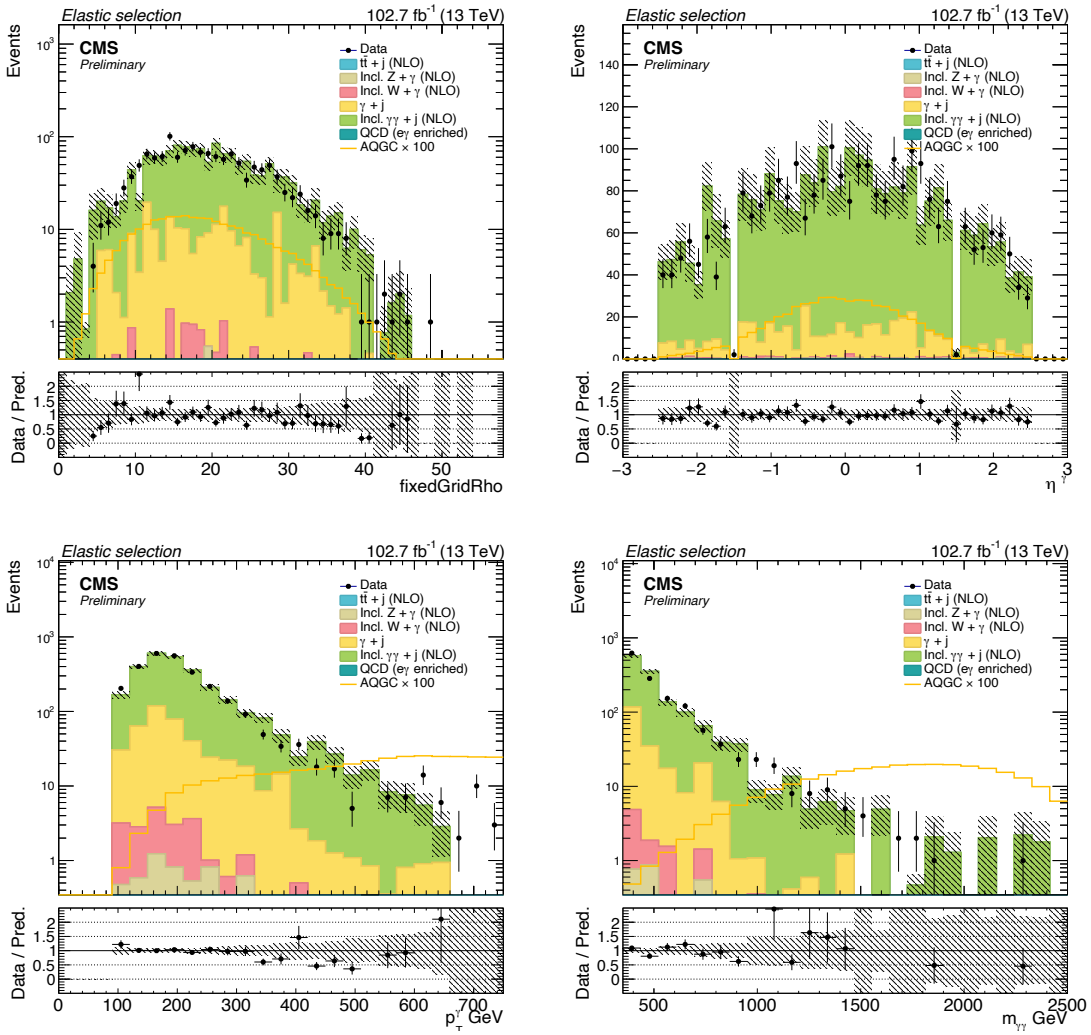

Figure 4.5: Kinematic distributions for four variables of interest in the elastic selection region defined in the text. The top left plot shows the average energy density ("fixedGridRho"), the variable used for reweighting at an earlier selection stage. The top right plot shows the single photon η distribution. The bottom left plot shows the single photon p_{T}. The bottom right plot shows the diphoton mass. The filled histograms represent various SM backgrounds and the yellow line histogram represents a potential AQGC signal multiplied by a factor of 100 for illustration purposes. All errors shown are statistical only.

region can be seen in Figure 4.5. A summary of the events passing the elastic selection can be seen in Table 4.7

Sample	Events
Incl. $\gamma\gamma + j$	1154.36 ± 57.46
Incl. $\gamma + j$	198.33 ± 29.33
Incl. $W\gamma$	8.17 ± 2.39
Incl. $Z\gamma$	3.09 ± 0.98
Total predicted	1363.95 ± 89.18
Observed	1380
Data/MC	1.01

Table 4.7: Summary of the predicted number of events for each Standard Model background contributing to the Elastic selection region. The errors quoted are statistical only.

4.3.4 $\xi \in$ PPS selection

The final step in the signal selection requires a cut on the ξ variables of the diphoton system within CMS. The motivation for this cut requires an understanding of the forward proton acceptance in PPS. Due to the LHC beam parameters and the location of the forward proton detectors, proton kinematics can be only be reconstructed for protons having a fractional momentum loss in the range of 2%-20%. This fractional momentum loss is referred to as the variable ξ with respect to the forward system.

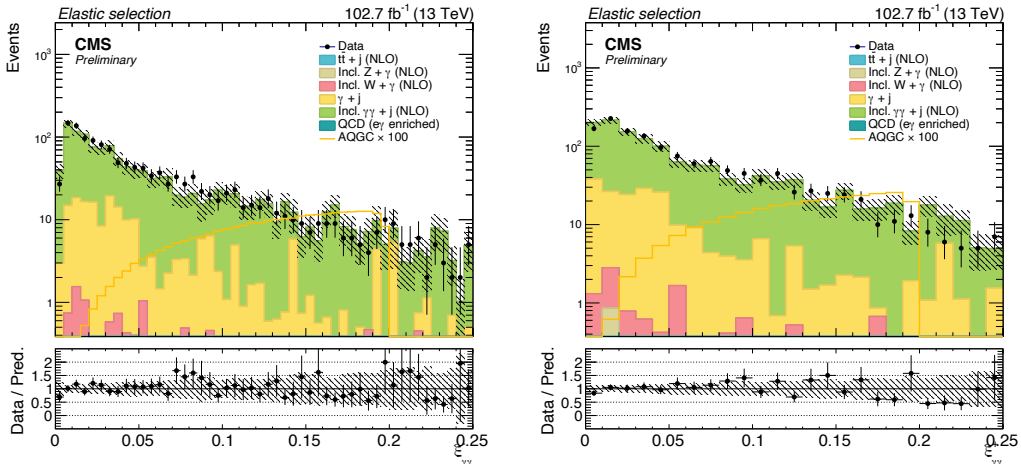

Figure 4.6: $\xi^{\pm}_{\gamma\gamma}$ distributions for diphoton events passing the elastic selection criteria. The filled histograms represent various SM backgrounds and the yellow line histogram represents a potential AQGC signal. All errors shown are statistical only.

In the case of a truly exclusive scattering event, the ξ values of the two intact protons are directly correlated to the central photons in CMS. We can therefore derive corresponding ξ values for the diphoton system based purely on kinematics. The positive and negative diphoton ξ values corresponding to the positive and negative side protons can be defined in this way:

$$\xi^{\pm}_{\gamma\gamma} = \frac{1}{\sqrt{s}} \sum_{i=1}^{2} p_{\mathrm{T}}^{\gamma_i} e^{\pm\eta_{\gamma i}} \tag{4.1}$$

The $\xi^{\pm}_{\gamma\gamma}$ distributions from the Elastic selection can be seen in Figure 4.6.

Since it is known that events having ξ values outside the range of 2-20% cannot be studied by this analysis, a loose cut is placed on the $\xi^{\pm}_{\gamma\gamma}$ such that $0.02 < \xi^{\pm}_{\gamma\gamma} < 0.20$.

The kinematic distributions of events in this selection region can be seen in Figure 4.7. A summary of the events passing the $\xi \in PPS$ selection can be seen in Table 4.8.

Sample	Events
Incl. $\gamma\gamma + j$	580.42 ± 41.03
Incl. $\gamma + j$	110.25 ± 22.47
Incl. $W\gamma$	3.72 ± 1.59
Incl. $Z\gamma$	2.04 ± 0.81
Total predicted	696.43 ± 65.90
Observed	735
Data/MC	1.06

Table 4.8: Summary of the predicted number of events for each Standard Model background contributing to the $\xi \in PPS$ selection region. Good agreement is observed between the data and simulation. The errors quoted are statistical only.

4.4 Proton reconstruction

4.4.1 Precision Proton Spectrometer

Detection of the forward protons is performed by PPS, which consists of RP detectors on both sides of CMS equipped with various sensor technologies throughout the Run II data-taking period. Silicon and pixel detectors were used for tracking whereas diamond and ultra-fast silicon (UFSD) detectors were used for timing. Only PPS tracking detectors are used in this analysis. The RP detectors are grouped into stations. The following nomenclature is commonly used to refer to those stations:

- 2016
  - 45-near (45N): +z-direction of CMS, 210 m from IP5 (closer to IP)
  - 45-far (45F): +z-direction of CMS, 210 m from IP5 (farther from IP)
  - 56-near (56N): -z-direction of CMS, 210 m from IP5 (closer to IP)
  - 56-far (56F): -z-direction of CMS, 210 m from IP5 (farther from IP)
- 2017, 2018
  - 45-near (45N): +z-direction of CMS, 210 m from IP5
  - 45-far (45F): +z-direction of CMS, 220 m from IP5
  - 56-near (56N): -z-direction of CMS, 210 m from IP5
  - 56-far (56F): -z-direction of CMS, 220 m from IP5

The naming scheme for sectors 45 and 56 is due to the positioning of the detectors between IP4 and IP5 or IP5 and IP6. A set of alignment parameters allows hits in the detector to be extracted as proton track kinematics [59].

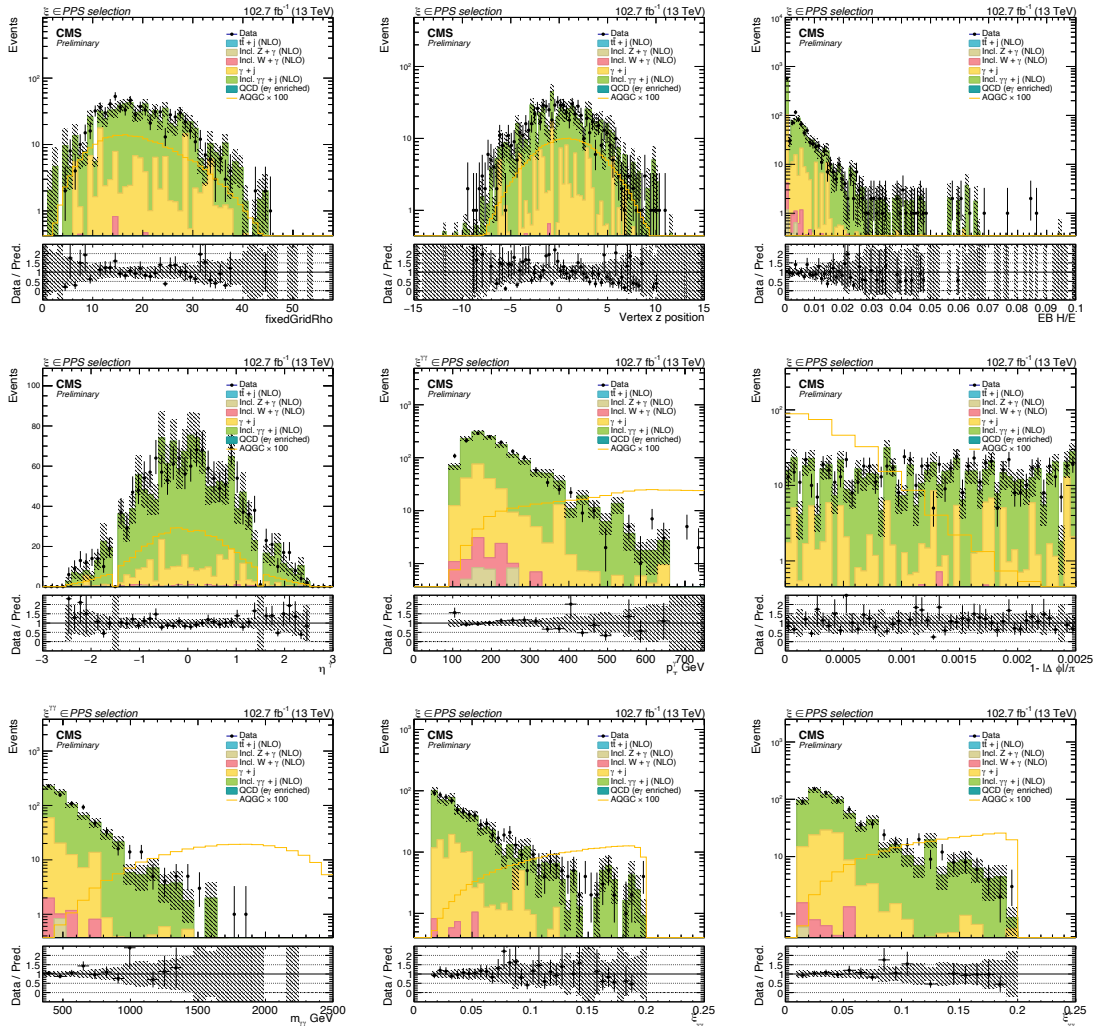

Figure 4.7: Kinematic distributions for four variables of interest in the $\xi \in PPS$ selection region defined in the text. From left to right and top to bottom, the variables plotted are the average event energy density, vertex-z position, H/E for photons in the barrel, single photon eta, single photon p_T, diphoton acoplanarity, diphoton mass, diphoton ξ^-, and diphoton ξ^+. The filled histograms represent various SM backgrounds and the yellow line histogram represents a potential AQGC signal. Good agreement is observed between the data and simulation. All errors shown are statistical only.

PPS utilized a different detector layout in each data-taking year of Run II. The differences in the experimental setups can be seen in Figure 2.9.

4.4.2 Reconstruction methods

Once the PPS detectors have been aligned, the relevant proton track parameters can be appropriately extracted. The amount of information that can be known about the forward protons is based on the reconstruction method that is used. There are two reconstruction methods, each with their own advantages.

Multi-RP reconstruction

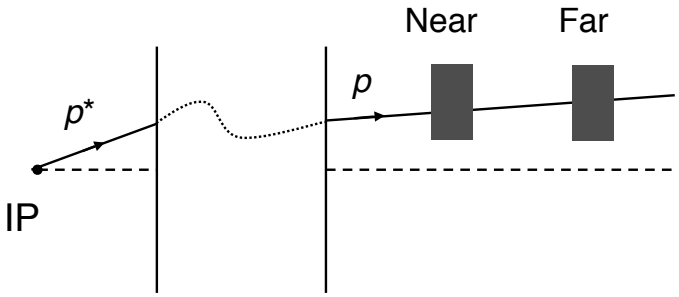

Figure 4.8: Schematic of one side of PPS showing the flight path of multi-RP reconstructed protons.

Multi-RP reconstruction occurs when a forward proton travels through both stations of PPS detectors on a given side as seen in Figure 4.8. Since the proton travels through both detectors, two points of the flight path are known, providing more information about the proton kinematics. The lever-arm of ~ 10 m between the two detectors allows for reconstruction of the scattering angle, θ, of the proton. Using the x-position and scattering angle of the proton, the fractional momentum loss can be calculated using the proton transport equation:

$$x(s) \simeq v_x x^* + L_x \theta_x^* + D_x \xi \qquad 4.2$$

where v_x is the vertex offset, L_x is the horizontal effective length, D_x is the horizontal dispersion, θ_x^* is the horizontal scattering angle, and ξ is the fractional momentum loss $\Delta p/p$.

The advantage to using this method is that the uncertainty on the ξ measurement is much smaller than in the alternate reconstruction case. However, the trade-off is the loss of statistics by requiring protons to travel through both the near and far detectors. This is the recommended reconstruction method by the CMS collaboration. This analysis uses the multi-RP method for the final limits. The resolution for both methods is discussed in section 4.4.5.

Single-RP reconstruction

Conversely, the single-RP reconstruction method is able to reconstruct any proton that traverses any of the RP stations. Since there is no lever arm to reconstruct the scattering angle of the protons, a linearized version of the proton transport equation is used:

$$x(s) \simeq D_x \xi$$

While the single-RP reconstruction method provides the advantage of statistics, the resolution on ξ is worse due to the approximation made in the transport equation. Comparisons between the ξ distributions of single-RP protons and multi-RP protons can be seen in Figure 4.9 for 2017 and 2018 data.

In this study, the multi-RP reconstruction is used by default and the single-RP reconstruction is used as a cross-check.

4.4.3 Proton treatment

The recommended treatment of the proton object by the collaboration is documented in this section.

Event-by-event proton characteristics

The specific imperfections in reconstruction pertaining to each proton based on the PPS data taking period and the ξ value are considered in the analysis. There are three characteristics studied for each proton:

- The bias in the reconstruction – calculated as the mean of the reconstructed ξ minus the true ξ for protons from simulation.
- The resolution – calculated as the RMS of the reconstructed ξ minus the true ξ for protons from simulation.
- The systematic uncertainties – imperfections in the alignment and optic corrections.

The values for each of the three characteristics are provided for each PPS era as a function of the proton ξ.

Shifted bunch-crossings

In 2017, for the RP equipped with pixel detectors in sector-45, a shift of one bunch-crossing was applied to 3 of the 6 sensors. This was done to mitigate the effects of radiation damage, which delayed the sensor readout time larger than the time interval between bunch-crossings. The period with this shift applied is referred to as the detector being in "3+3" mode. In this mode, a large fraction of proton tracks reconstructed closest to the beam are expected to be from the adjacent bunch-crossing. In practice, this means that the efficiencies of the detectors during this period need special treatment, and only the proton tracks coming from the three unaffected sensors (from the correct bunch-crossing) should be used for analysis. The run ranges where this occurred are:

- 300802 - 303337

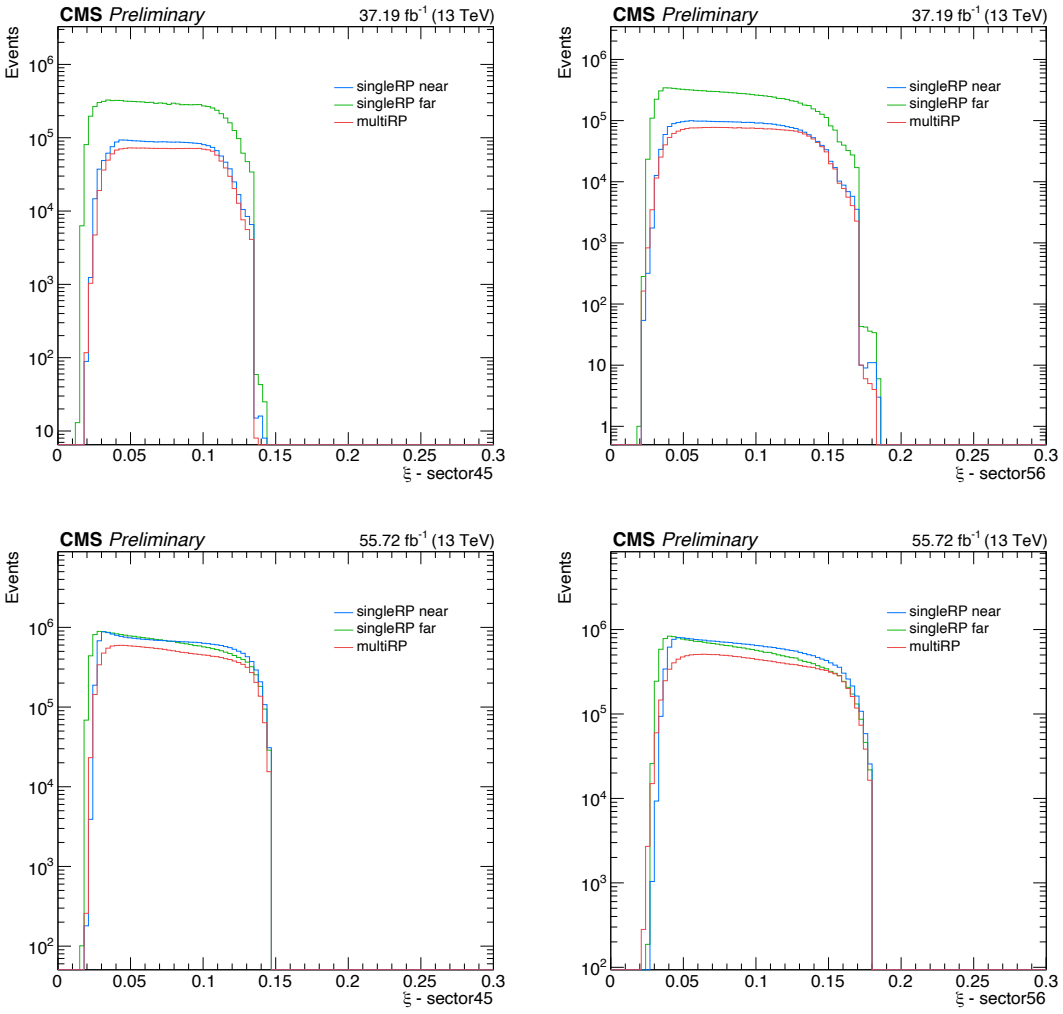

Figure 4.9: Comparison of single-RP and multi-RP reconstructed ξ values in data passing the recommended proton fiducial cuts. The top row is data from 2017 and the bottom row is from 2018. The left column is for protons in sector-45 and the right column is from protons in sector-56. The difference between the number of reconstructed protons in the near pot vs the far pot for the two years can be ascribed to the different detector configurations described in Section 4.4.1.

- 305169 - 307082

Similarly, the same problem existed in 2017 in sector 56 for the following run ranges:

- 305965 - 307802

Fiducial Cuts

Fiducial cuts are applied to the proton object for both data and simulation in this analysis. The lower limits are motivated by the study of the edge effects of the sensors whereas the upper limits are motivated by the LHC collimator aperture studies. Cuts are made on the scattering angle, θ_x^*, as a function of the proton ξ. For 2017 and 2018 protons, the cuts are also dependent on the LHC crossing angle. Additionally, lower limits on ξ are taken in to account with the efficiencies described in section 4.4.5.

4.4.4 Proton distributions

Following the proper treatment of protons in the analysis, the ξ distributions are consistent with the distributions of other analyses [60, 61]. The distributions of ξ can be seen for both RP stations used in 2016 in Figure 4.10 and for all four RP stations used in 2017 and 2018 in Figure 4.11. The events that are reconstructed by the single-RP and multi-RP algorithms in 2017 and 2018 can be seen in Figure 4.12. The distribution of the number of reconstructed protons can be seen for the three years of data taking in Figure 4.13.

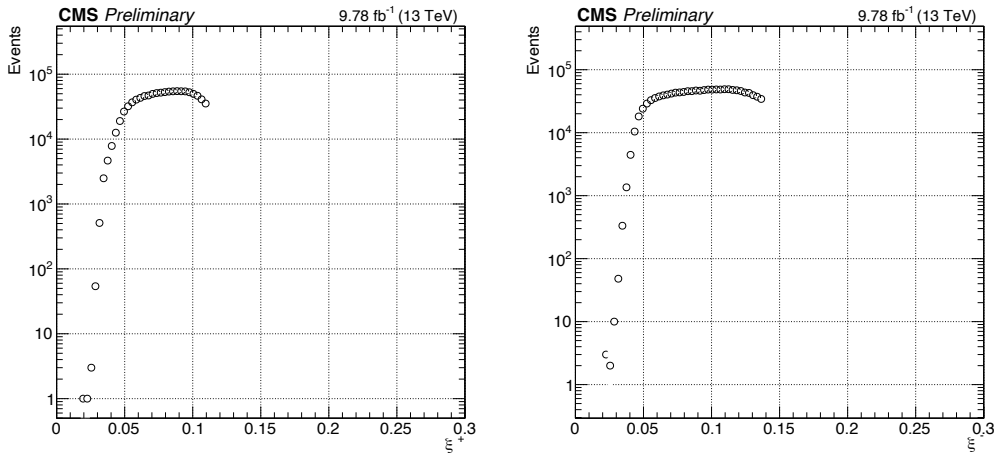

Figure 4.10: ξ distributions for the two RP stations used in 2016. The cut off is based on the aperture cuts for applying efficiencies.

4.4.5 Proton direct simulation

PPS developed a direct simulation of the propagation from IP5 to the forward detectors based on the LHC optics configuration and the PPS experimental setup. This simulation was not available at the time of the analysis discussed in Chapter 3. The direct simulation takes simulated protons as an input and correctly propagates them through the LHC magnetic lattice, providing a collection of reconstructed protons as would exist in

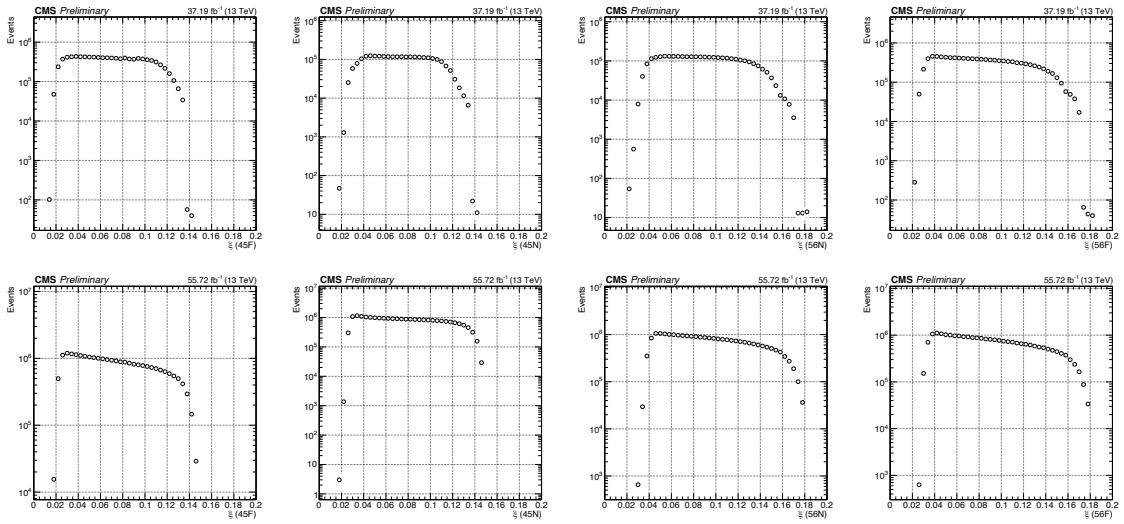

Figure 4.11: ξ distributions for the four RP stations. Plots for 2017 data are shown in the top row and plots for 2018 data are shown in the bottom row.

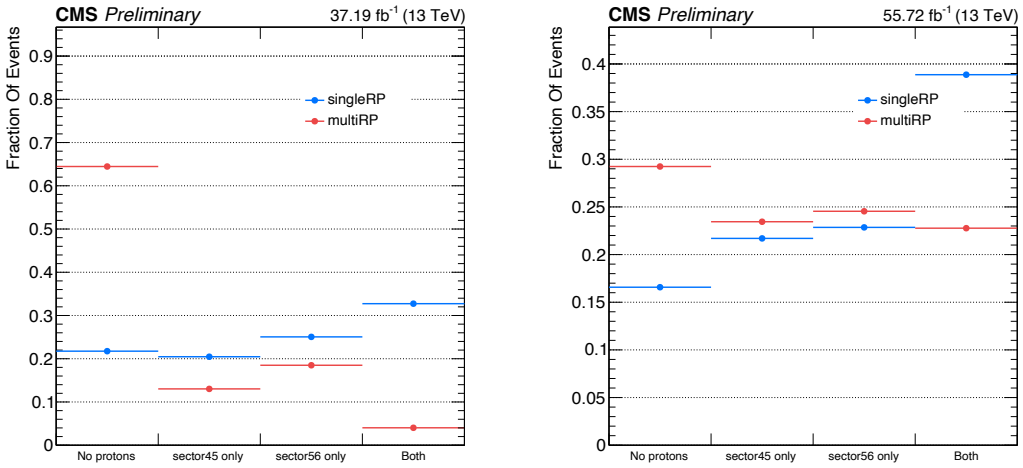

Figure 4.12: Events passing the HLT trigger are separated into four categories. Events with no protons, one proton in sector-45, one proton in sector-56, or at least one proton in each sector. These distributions are shown for 2017 data (left) and 2018 data (right). This analysis uses events from the fourth category.

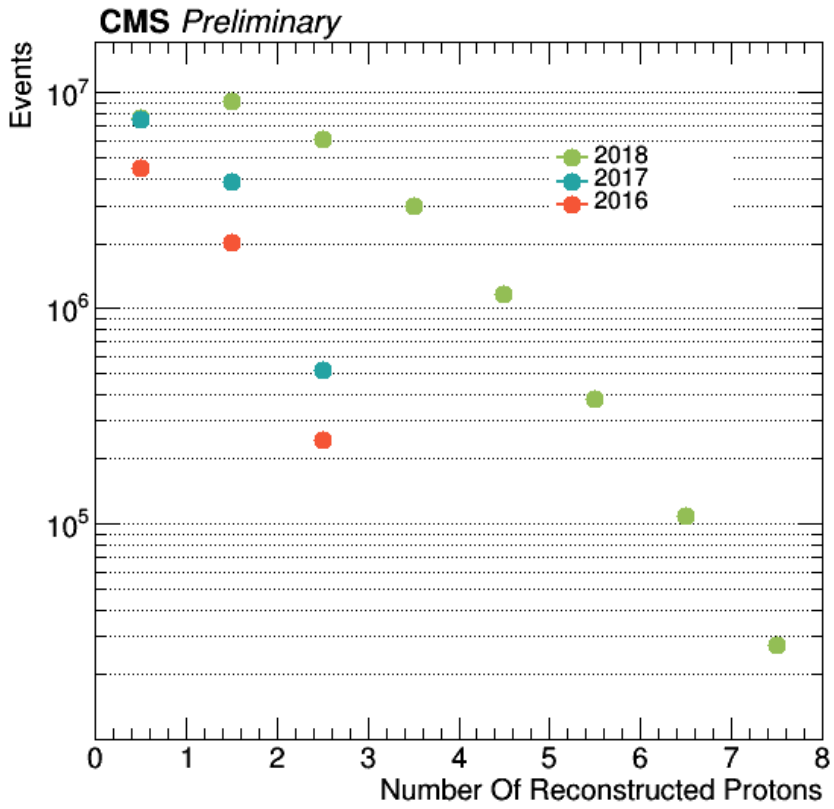

Figure 4.13: Number of reconstructed protons in each data taking year. The number of protons is much higher in 2018 because of the use of pixel detectors.

data. The simulation can be configured to specify the year, detector configuration, beam divergence, average beam spot, and LHC crossing-angle.

In this study, the direct simulation is applied to generated signal MC samples.

The various configurations of the proton simulation are used with the MC sample in proportion to the parameters that appear in the Run II data. For example, the crossing-angle is configured in the simulation proportional to the amount of data that was taken using that LHC crossing-angle.

Using the generated and reconstructed proton information, one can study the resolution on the proton reconstruction methods. The difference on the ξ resolution between the single-RP reconstruction method and the multi-RP reconstruction method can be seen in Figures 4.14 and 4.15. The root mean square (RMS) is observed to be much smaller for the multi-RP protons compared to the single-RP protons. To reiterate, the multi-RP reconstruction is used by default in this analysis.

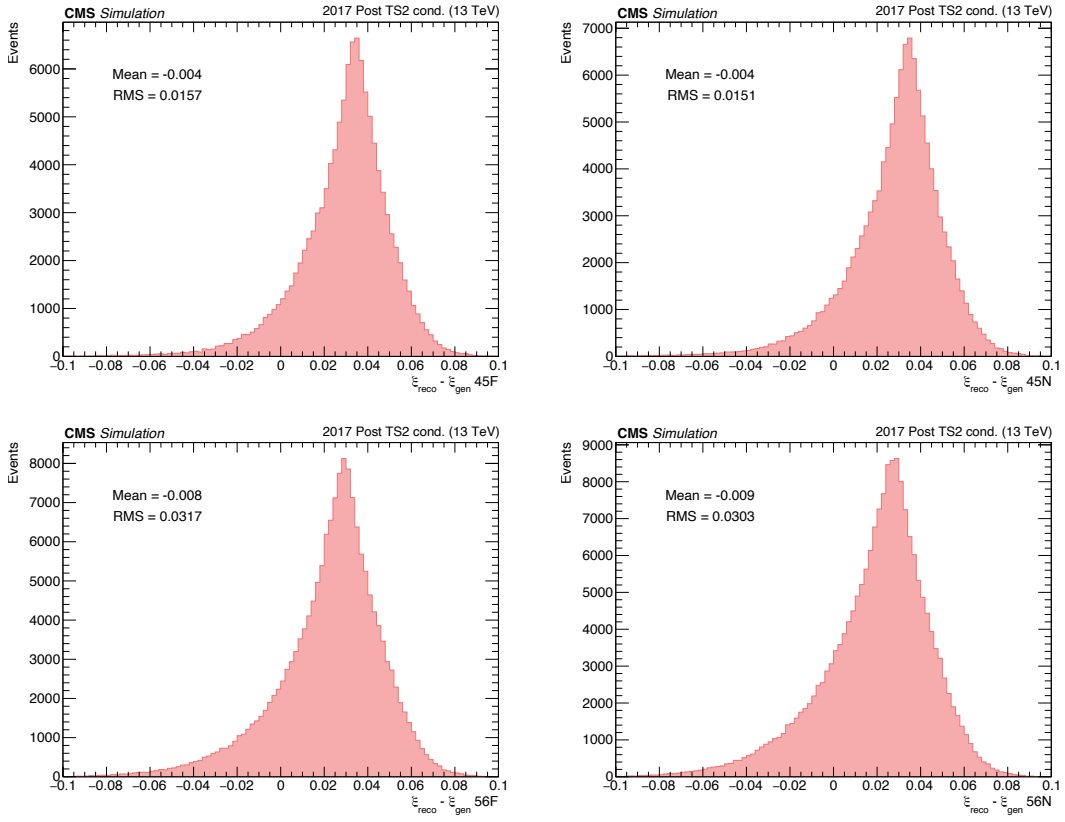

Figure 4.14: Difference between the reconstructed and generated ξ value for all four RP stations for single-RP protons. The distributions are not centered at zero, which is accounted for in the bias term of the reconstruction uncertainty.

PPS Acceptance

The acceptance of PPS is nominally between fractional momentum losses of 2-20%, however, there are many variables that affect the experimental acceptance. For example, the acceptance can be affected by LHC collimators, LHC crossing-angle, location of the RPs, LHC magnet parameters, configuration of the sensors, types of detectors, etc.

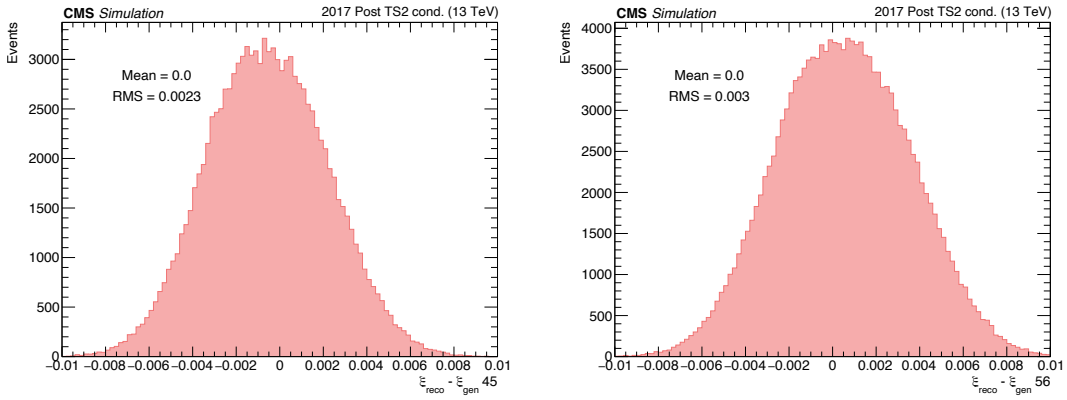

Figure 4.15: Difference between the reconstructed and generated ξ value for all four RP stations for multi-RP protons.

A set of aperture cuts were derived by the collaboration and are used in the direct simulation. Separate sets of aperture cuts exist for each PPS detector and each PPS era. The aperture cuts for pixels are given for 2017 in Table 4.9 and for 2018 in Table 4.10. The aperture cuts for the strip detectors are taken as the maximum and minimum track values for which the two-dimensional efficiencies are calculated.

2017 Era	45F x_{min}	45F x_{max}	45F y_{min}	45F y_{max}	56F x_{min}	56F x_{max}	*56F y_{min}	56F y_{max}
2017B	1.995	24.479	-11.098	4.298	2.422	24.620	-10.698	4.698
2017C1	1.860	24.334	-11.098	4.298	2.422	24.620	-10.698	4.698
2017C2	1.860	24.334	-11.098	4.298	2.422	24.620	-10.698	4.698
2017D	1.860	24.334	-11.098	4.298	2.422	24.620	-10.698	4.698
2017E	1.995	24.479	-10.098	4.998	2.422	24.620	-9.698	5.498
2017F1	1.995	24.479	-10.098	4.998	2.422	24.620	-9.798	5.398
2017F2	1.995	24.479	-10.098	4.998	2.422	24.620	-9.798	5.398
2017F3	1.995	24.479	-10.098	4.998	2.422	24.620	-9.798	5.398

Table 4.9: Aperture cuts applied to the proton tracks for 2017 data. All values are given in mm.

2018 Era	45 210 x_{min}	45 210 x_{max}	45 210 y_{min}	45 210 y_{max}	45 220 x_{min}	45 220 x_{max}	45 220 y_{min}	45 220 y_{max}
2018A	2.850	17.927	-11.598	3.698	2.421	24.620	-10.898	4.398
2018B1	2.850	17.927	-11.598	3.698	2.421	24.620	-10.898	4.198
2018B2	2.564	17.640	-11.598	4.198	2.140	24.479	-11.398	3.798
2018C	2.564	17.930	-11.098	4.198	2.421	24.620	-11.398	3.698
2018D1	2.850	17.931	-11.098	4.098	2.421	24.620	-11.398	3.698
2018D2	2.850	17.931	-10.598	4.498	2.421	24.620	-11.698	3.298
2018 Era	56 210 x_{min}	56 210 x_{max}	56 210 y_{min}	56 210 y_{max}	56 220 x_{min}	56 220 x_{max}	56 220 y_{min}	56 220 y_{max}
2018A	3.275	18.498	-11.298	3.298	2.421	25.045	-10.398	5.098
2018B1	3.275	18.070	-11.198	4.098	2.564	25.045	-10.398	5.098
2018B2	3.275	17.931	-10.498	4.098	2.279	24.760	-10.598	4.498
2018C	3.275	17.931	-10.498	4.698	2.279	24.760	-10.598	4.398
2018D1	3.275	17.931	-10.498	4.698	2.279	24.760	-10.598	4.398
2018D2	3.275	17.931	-9.998	4.698	2.279	24.760	-10.598	3.898

Table 4.10: Aperture cuts applied to the proton tracks for 2018 data. All values are given in mm.

PPS Efficiencies

Efficiencies of the PPS detector system are considered separately for strip and 3D pixel detectors. Two-dimensional histograms are provided for each PPS era as a function of the

proton track x and y positions in contrast with the flat efficiencies applied in Chapter 3.

Two sources of inefficiency are considered for the silicon strip detectors (2016 and 2017 data). When more than one proton passes through the strip detectors per bunch crossing, the reconstruction algorithm fails. This failure is considered as a "multi-tracking" inefficiency and is one of the two components considered for the strip efficiencies. The second component is the inefficiency due to radiation damage.

The efficiencies for the 3D pixel detectors (2017 and 2018 data) are also comprised of two factors: the radiation damage to the readout of the detectors and the tracking inefficiency.

In both cases, an upper limit is placed on the possible inefficiency due to showers in the detectors. This upper limit is quoted at 1.5% (1.7%) for protons in sector-45 (sector-56).

These efficiencies are accounted for in the direct simulation. Efficiencies from each PPS era are applied to the simulation in proportion to the amount of data recorded from that era.

Calculating $\epsilon \times A$

Combining the two effects of acceptance and efficiency is crucial for contextualizing potential signal events. The $\epsilon \times A$ term is used for translating signal significance into cross-sections. Using the proton direct simulation, one can study these two effects together as a function of ξ. The combination of these two effects can be seen for each data taking year in Figure 4.16. This simulation is applied directly to the signal protons to study the PPS signal efficiency that will be discussed in Section 4.5.4.

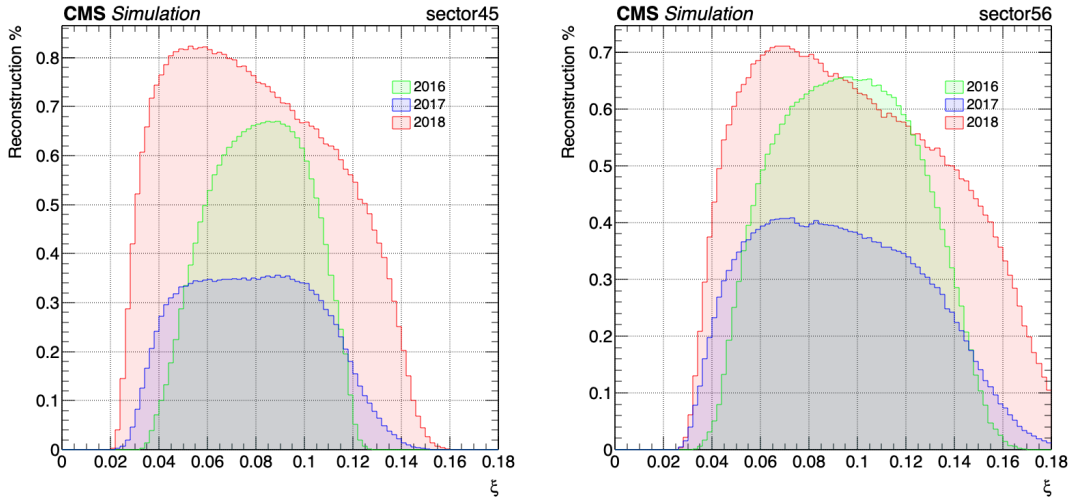

Figure 4.16: Both efficiency and acceptance effects parameterized as function of the proton ξ for all years. Differences in the reconstruction percentage can be attributed to differences in detector location, configuration, and design.

4.5 Results

A summary of the CMS-only event selection can be seen in Figures 4.17 and 4.18. In addition to the CMS selection cuts, it was found that placing a lower cut on the proton ξ values of 0.035 decreases the background (discussed in Section 4.5.2) while not decreasing the signal efficiency. An asymmetric cut is placed on the upper end of the proton ξ spectrum motivated by the efficiency plots shown in Figure 4.16. These asymmetric cuts are placed at 0.15 for sector45 and 0.18 for sector56. A selection on the number of protons in a given bunch crossing per arm was investigated, but it was found that no significant improvement was gained on the signal to background ratio. After the final selection stage, a comparison between the forward diproton and central diphoton kinematics is performed. This is done by converting the proton ξ values to diproton "missing mass" and rapidity values using Equation 4.3. The uncertainties on these calculated values are given by Equation 4.4.

4.5.1 Forward-central matching

$$m_{pp} = \overline{s\xi_p^+\xi_p^-}, \quad y_{pp} = \frac{1}{2}\log\frac{\xi_p^+}{\xi_p^-} \ . \tag{4.3}$$

$$\frac{\delta m_{pp}}{m_{pp}} = \delta y_{pp} = \frac{1}{2}\ \frac{\delta\xi_p^+}{\xi_p^+} \oplus \frac{\delta\xi_p^-}{\xi_p^-} \ . \tag{4.4}$$

The window for an event to be considered matching is within 2σ of equivalence between the forward and central mass and rapidity. The criteria for this matching within 2σ of the uncertainties can be found in Equations 4.5 and 4.6. We also check for matching within a 3σ window for comparison.

$$m_{pp} - m_{\gamma\gamma}\ /\sigma\ m_{pp} - m_{\gamma\gamma}\ < 2 \tag{4.5}$$

$$y_{pp} - y_{\gamma\gamma}\ /\sigma\ y_{pp} - y_{\gamma\gamma}\ < 2 \tag{4.6}$$

where $\sigma\ m_{pp} - m_{\gamma\gamma}\ $ and $\sigma\ y_{pp} - y_{\gamma\gamma}\ $ are the uncertainties on the diphoton and diproton mass and rapidity, respectively. These uncertainties are derived event-by-event.

Figure 4.19 shows all of the events passing the final CMS diphoton selection within a 20σ mass matching window. Figure 4.20 shows the same events within a 20σ rapidity matching window. Combining these plots into a single 2D plot is seen in Figure 4.21. Two events are observed in the 2σ window – the final signal region.

4.5.2 Background estimation

The signal region of the forward-central matching is expected to have contamination from pileup contributions. The overlapping of pileup protons with inclusively produced diphotons in CMS can lead to "accidental" forward central matching. Figure 1.6 shows the overlapping of two separate and mutually exclusive processes that could be misinterpreted

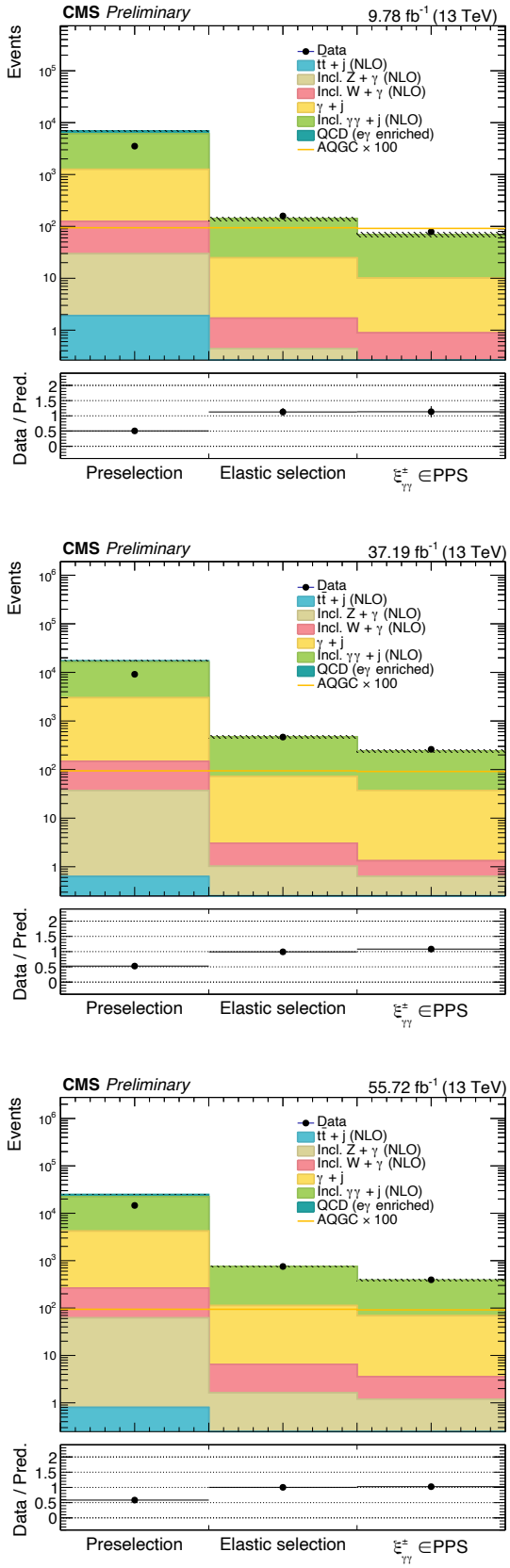

Figure 4.17: Summary of the contributions to the various selection regions described in section 4.3. The top plot is for 2016 data, the middle plot is for 2017 data, and the bottom plot is for 2018 data.

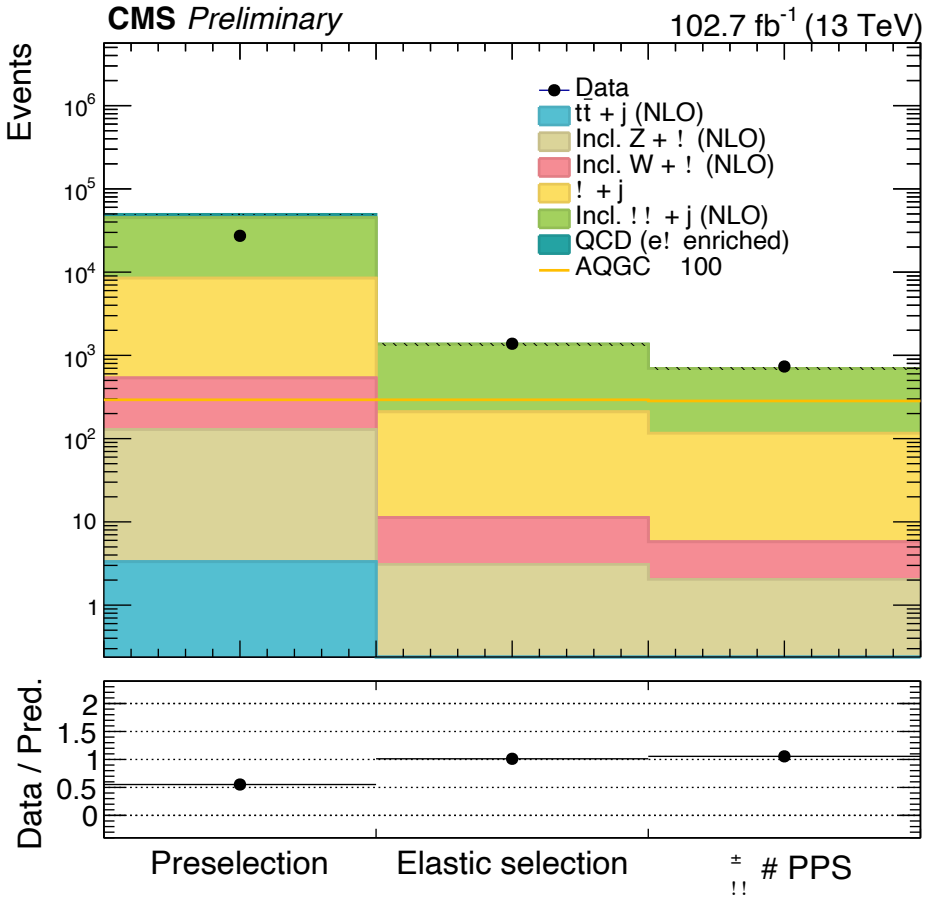

Figure 4.18: Summary of the contributions to the various selection regions described in section 4.3 for 2016, 2017, and 2018 samples combined.

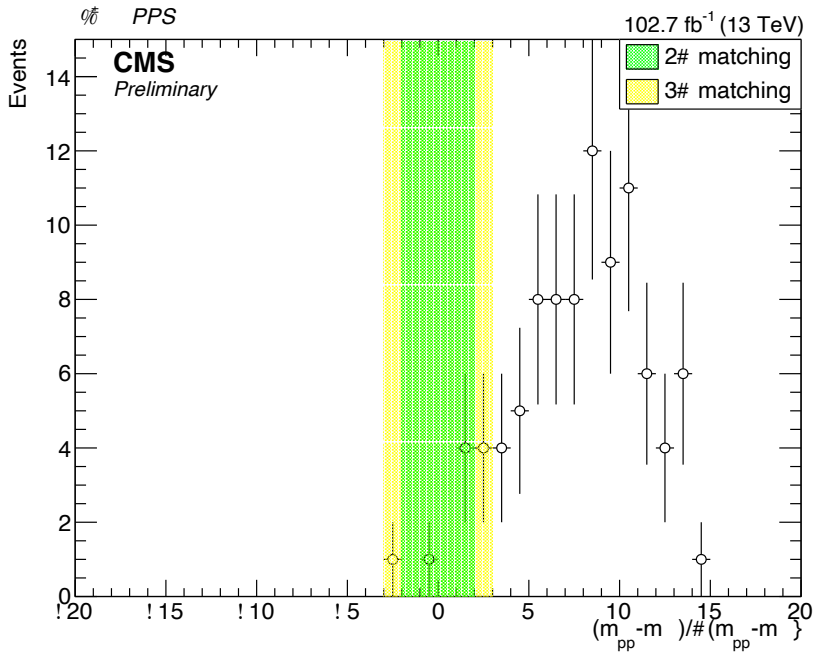

Figure 4.19: Mass matching for events passing the CMS diphoton selection with two multi-RP reconstructed protons. Events matching at 2σ appear in the green region and events matching at 3σ appear in the yellow region.

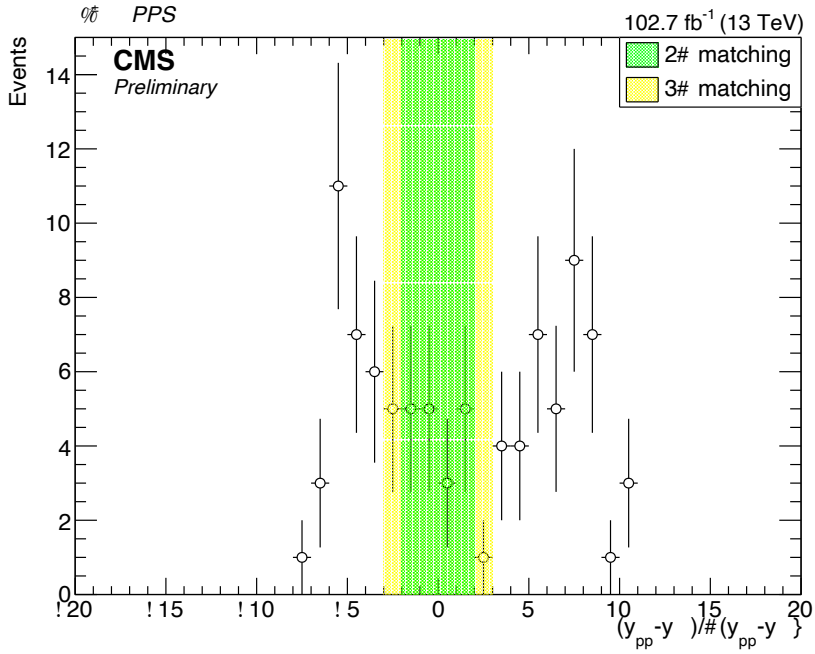

Figure 4.20: Rapidity matching for events passing the CMS diphoton selection with two multi-RP reconstructed protons. Events matching at 2σ appear in the green region and events matching at 3σ appear in the yellow region.

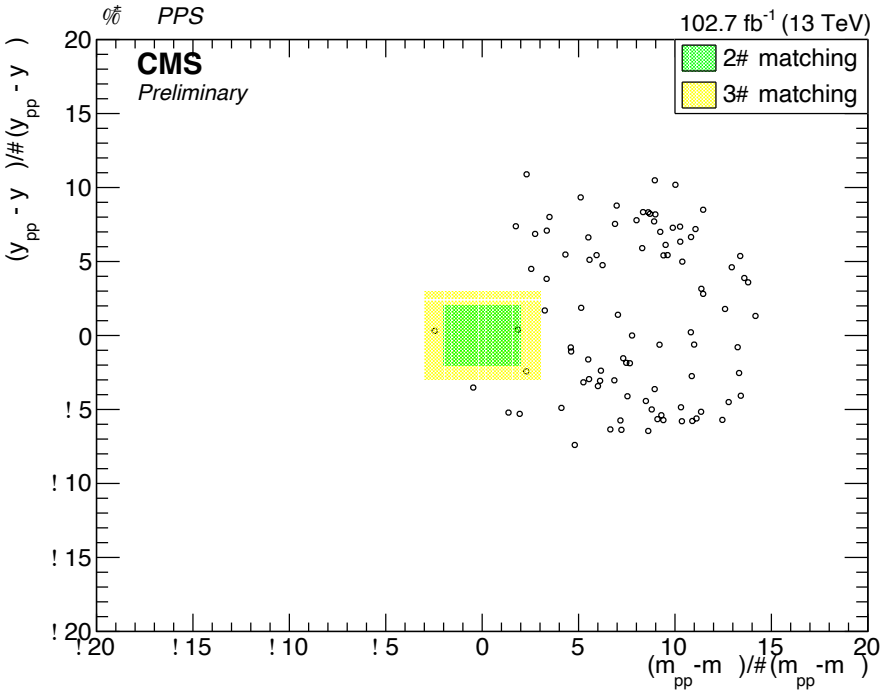

Figure 4.21: Two-dimensional mass and rapidity matching for events passing the CMS diphoton selection with two multi-RP reconstructed protons. Events matching at 2σ appear in the green region and events matching at 3σ appear in the yellow region.

as one signal event. To quantify how these events contaminate the signal region, we use a fully data-driven approach to creating toy events. This can be contrasted with the approach in Chapter 3 that sampled diphoton kinematics from a fitted function.

As inputs for the creation of the toy events, diphoton events in the signal region described in section 4.3.4 are used as well as all protons from the Run 2 data taking period passing the diphoton trigger described in section 4.3.1. Starting with the first diphoton pair, a set of protons are added to the two photons from the same run and LHC crossing-angle. We then check for the forward-central matching in mass and rapidity. This procedure is done for all of the diphoton events in the $\xi \in$ PPS region to create one toy experiment. This method will be referred to as "Data Mixing". Since the protons are randomly mixed with the diphotons, any matching that occurs is truly accidental and not due to a true correlation between the forward and central systems.

To fully understand how often these background events occur, many toy experiments are studied until the number of matching events at 2 and 3σ converges. From a statistics perspective, it is very useful to study the single-RP reconstructed protons – as these are more abundant – to validate the background estimation procedure.

For validation, the procedure is first explained using the 2017 data. After this explanation, the background estimations for all years will be shown.

Four of these toy experiments can be seen in Figure 4.25. Once confidence in the method has been established with large statistics, we then move on to the multi-RP reconstructed proton toy experiments. Based on the calculation for the mass and rapidity

shown in equation 4.3, we expect that $m_{pp} > m_{\gamma\gamma}$ and $y_{pp} < y_{\gamma\gamma}$.

Figure 4.22 shows the distribution of the number of toy events matching at 2 and 3σ for single-RP reconstructed protons. The distribution follows a Poisson distribution, as expected.

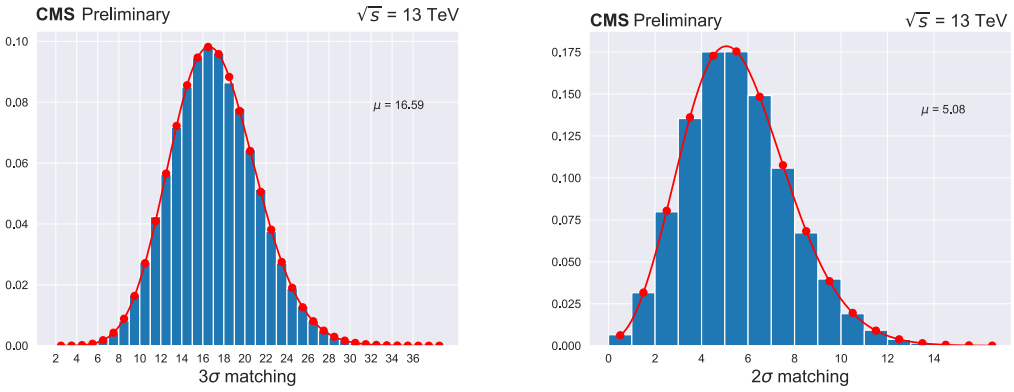

Figure 4.22: Distribution of the number of events matching at 3σ (left) and 2σ (right) for 10,000 data-driven toy experiments. The average number of matching events is shown in text on the plots and the red points are the values for a Poisson distribution at the given μ value.

The mean value of matching events was tracked during the production of the toy experiments to understand the point of convergence. The convergence of the mean value of matching events can be seen for the single-RP case in Figure 4.23. The value converges around 10,000 events so it was decided to create 100,000 events to be sure to avoid any further fluctuations.

This method of estimating the background can be verified in two independent ways. The first is another completely data driven approach, using a side band selection region of diphoton events to create toy events. By reversing the "elastic" selection described in section 4.3.3, while still keeping the requirements of the diphoton ξ values described in section 4.3.4, one obtains a large sample of diphoton events that is completely dominated by background. Using this side-band diphoton selection, we again mix each event randomly with protons from the same run and LHC crossing-angle. Checking for forward-central matching, and normalizing for the number of events in this side-band region, compared with the signal region, we obtain another independent background estimation. The distribution of events as a function of the 2-dimensional matching parameters can be seen in Figure 4.24. This method is referred to as "Reverse Elastic Mixing".

The second validation method also requires creating toy events. This time, the diphoton sample consists of the MC events falling in the signal selection. By mixing these MC diphoton events with random protons from data, a third method to estimate the background is derived. This method is referred to as "MC Mixing".

These three methods of estimating the backgrounds with the single-RP reconstructed protons can be done for multi-RP reconstructed protons since the background events will have a complete decorrelation between the forward and central systems. The summary of the background yields of these estimation procedures can be found in table 4.11.

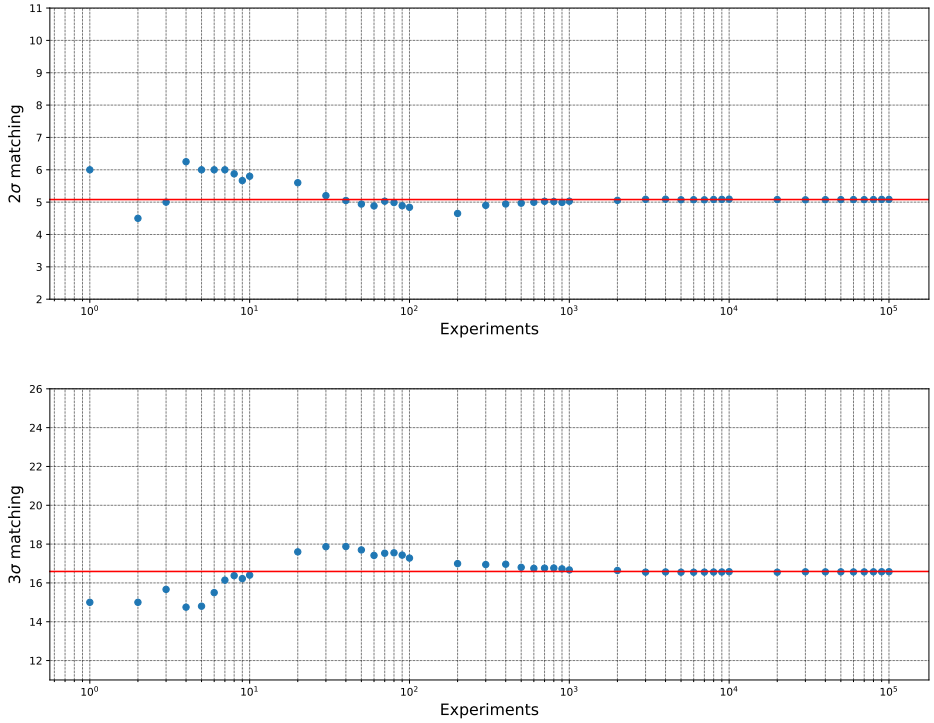

Figure 4.23: The average number of events matching at 3σ (top) and 2σ (bottom) as a function of the number of toy experiments.

	single-RP		**multi-RP**	
Significance	3σ	2σ	3σ	2σ
Data Mixing	16.59	5.08	0.37	0.15
MC Mixing	15.97	4.87	0.35	0.14
Reverse Elastic Mixing	15.59	4.44	0.29	0.12

Table 4.11: Summary of the background estimation yields for 2017 single-RP and multi-RP reconstructed protons using the three independent background estimation procedures described in the text. Good agreement is observed between the three methods.

The multi-RP background estimation is performed in the same way as the data mixing for the single-RP case.

Since the Reverse Elastic selection is, by definition, not the signal region, it can be unblinded and compared with the background estimation for the same region. It is important to note that the background estimation is an average over many toy experiments whereas the true number of matching events in this region is effectively a sampling of a distribution. The comparison of predicted and true events can be seen in Table 4.12.

Repeating this process for the 2016 and 2018 data gives the results shown in Table 4.13.

Examples of toy experiments combining all three years can be seen in Figure 4.26. These toy experiments are analogous to the true matching seen in Figure 4.21.

The difference in the background estimations between the years can be attributed to the luminosity, detector, and efficiency differences. In 2018, PPS used all pixel detectors,

	multi-RP	
Significance	3σ	2σ
Reverse Elastic Matching	55	26
Reverse Elastic Estimate	58.3	24.1

Table 4.12: Comparison of the true number of matching events in the Reverse Elastic selection region with the number of events predicted by the background estimation method detailed in the text. No rescaling to the signal region is performed. The numbers correspond to data combined from 2017 and 2018.

	2016		**2017**		**2018**	
Significance	3σ	2σ	3σ	2σ	3σ	2σ
Data Mixing	0.067	0.030	0.398	0.163	2.29	0.910
MC Mixing	0.065	0.026	0.360	0.145	1.86	0.720
Reverse Elastic Mixing	0.057	0.023	0.292	0.122	1.99	0.802

Table 4.13: Summary of the background estimation yields for multi-RP reconstructed protons using the three independent background estimation procedures described in the text.

capable of reconstructing multiple protons within a given bunch crossing. This leads to higher signal efficiency but also higher background contamination. A cross-check was performed to validate this difference. The same background estimation procedure was performed for 2018 data using only events with exactly one proton in each arm, corresponding to the 2017 scenario in which protons would be successfully reconstructed. The reason for doing this is to check that the background estimation performs the same when the multi-tracking efficiency does not affect the proton reconstruction as in the case when there is only one proton in each arm. It was observed that this background estimation for 2018 was in agreement with the results for the 2017 estimation (normalized by luminosity), thus verifying that the difference between the amount of expected background for 2017 and 2018 is due to the difference in detector configurations.

Since more than one proton can be reconstructed with the 2018 configuration, a method is needed to determine which proton to use for kinematic matching. Two methods were explored. The first method is to use the proton with an ξ value closest to the corresponding diphoton ξ value. This gives the highest signal efficiency but also the highest background efficiency. The second method, and the one currently used in the analysis, is to choose the proton with the highest ξ value. This gives a slightly higher signal to background ratio.

Using the independent background estimations procedures, systematic uncertainties can be derived on the background estimation for each year. Taking the data mixing result in the 2σ region for each year as the default, the relative difference between the other two methods' results gives two choices for the systematic uncertainty for each year. The maximum of these two options is assigned as the systematic uncertainty on the background estimation procedure. The systematic uncertainties are calculated to be 23.3%, 25.2%, and 20.9% for 2016, 2017, and 2018, respectively.

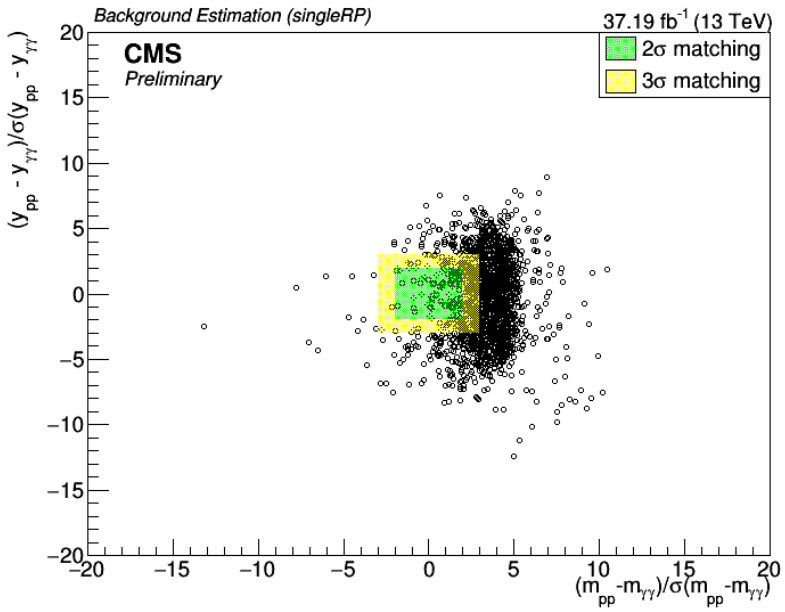

Figure 4.24: Distribution of events for the 2017 Reverse Elastic Mixing method described in the text using single-RP protons. Events within the green (yellow) box are matching at 3σ (2σ).

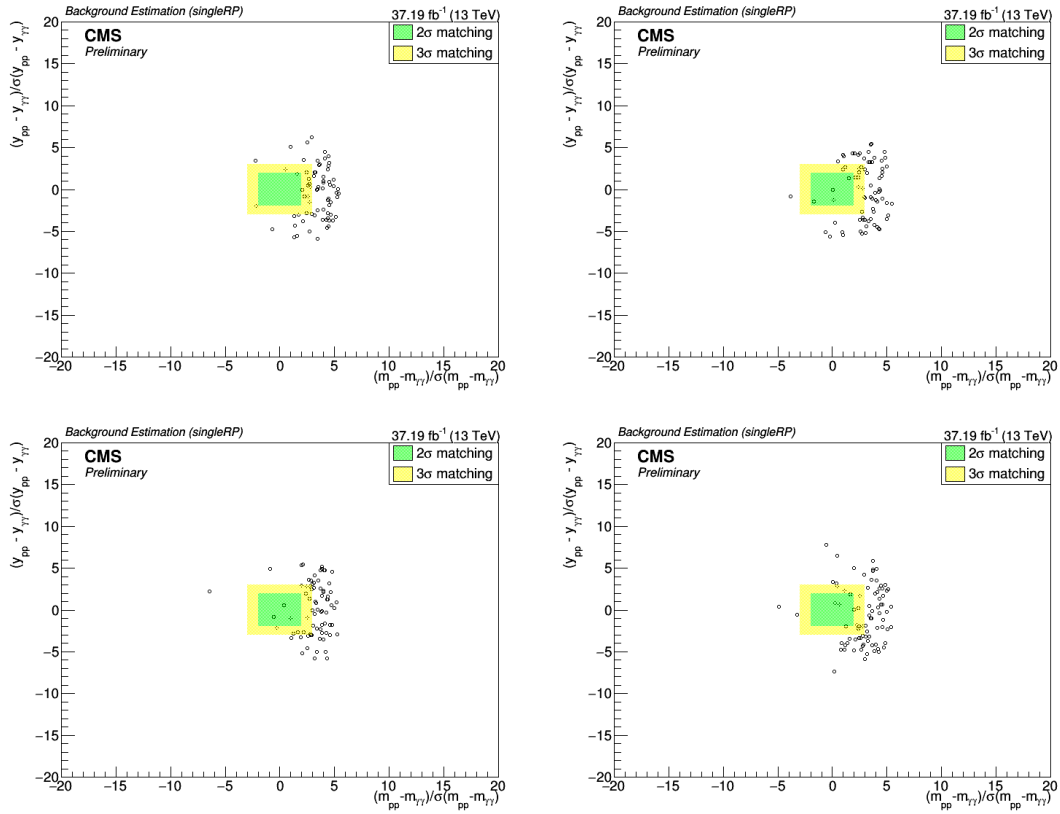

Figure 4.25: Examples of toy experiments and matching events (inside yellow and green boxes) created by the data driven background estimation procedure described in the text. These toy experiments are for the single-RP reconstructed protons in 2017 data.

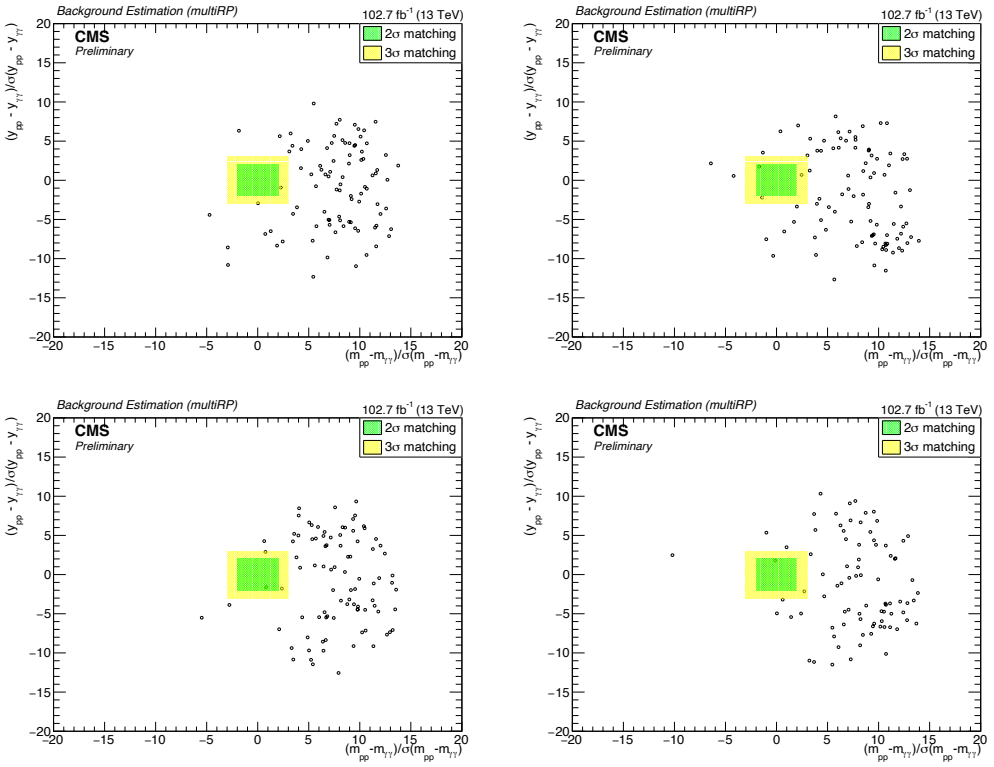

Figure 4.26: Examples of toy experiments and matching events (inside yellow and green boxes) created by the data driven background estimation procedure described in the text. These toy experiments are for the multi-RP reconstructed protons in all three years of data taking.

4.5.3 Systematic uncertainties

The following systematic uncertainties are considered in this analysis:

- For 2016, 2017, and 2018 data, the systematic uncertainties ascribed to the CMS luminosity are 2.5%, 2.3% and 2.5%, respectively.
- A conservative 1.7% uncertainty is quoted on the particle showers in the PPS detectors in 2018 only. This uncertainty was studied by the CMS proton object group.
- A 23.3%, 25.2%, and 20.9% systematic uncertainty on the background estimation procedure for 2016, 2017, and 2018, respectively as calculated in Section 4.5.2.
- A 10% uncertainty on the proton rapidity gap survival probability as done in [61] and calculated in [69].
- For 2016, 2017, and 2018, the systematic uncertainties assigned to the signal efficiency corresponding to the photon ID SF uncertainties are 3.1%, 7.0%, and 2.9%, respectively.
- Event-by-event systematic uncertainties are assigned to each proton in the matching procedure.

Source	**Uncertainty**
CMS Luminosity	1.2%
Background estimation	23.3%
Photon ID scale factors	3.1%
Rapidity Gap Survival Probability	10%

Table 4.14: Systematic uncertainties corresponding to the 2016 dataset.

Source	**Uncertainty**
CMS Luminosity	2.3%
Background estimation	25.2%
Photon ID scale factors	7.0%
Rapidity Gap Survival Probability	10%

Table 4.15: Systematic uncertainties corresponding to the 2017 dataset.

Source	**Uncertainty**
CMS Luminosity	2.5%
Particle Showers in PPS	1.7%
Background estimation	20.9%
Photon ID scale factors	2.9%
Rapidity Gap Survival Probability	10%

Table 4.16: Systematic uncertainties corresponding to the 2018 dataset.

4.5.4 Limits on anomalous quartic gauge couplings

With one event observed in the signal region for an expected background of 1.103 ± 0.007 (statistical) events, limits are placed on the anomalous coupling parameters, ζ_1 and ζ_2.

The modified frequentist criterion CLs [79, 80] with the profile likelihood ratio test statistic modified for upper limits [81] and determined by pseudo-experiments is used to evaluate the observed and expected limits at 95% confidence level (CL) on the production cross section of AQGC LbL scattering within the fiducial region. The signal efficiency is evaluated over a wide range of the couplings parameters ζ_1 and ζ_2 using FPMC [66] and found approximately constant for each year in the search region. The $\epsilon \times A$ terms for both CMS and PPS can be seen in Table 4.17.

Year	**CMS** $\epsilon \times A$	**PPS** $\epsilon \times A$	$\epsilon \times A$
2016	80.1%	6.5%	5.2%
2017	75.7%	3.3%	2.5%
2018	77.4%	18.4%	14.2%

Table 4.17: Anomalous coupling signal efficiency and acceptance for each year of the Run II period. The CMS efficiency is shown in the left column, the PPS efficiency is shown in the middle column, and product of the CMS and PPS efficiencies is shown in the right column.

In addition to these efficiency and acceptance terms, the asymmetric ξ acceptance of the detectors and hence the fiducial volume of the analysis need to be considered. The percentage of the generated signal falling within this asymmetric range is calculated to be 63.8% and is accounted for in the limit setting procedure.

Systematic uncertainties are included as a nuisance parameter in the likelihood with a log-normal probability density function. The observed and expected results from the Combine tool can then be used to derive limits on the four-photon anomalous coupling.

To translate the upper limits on the AQGC cross-section to the limit on the coupling parameters, ζ_1 and ζ_2, we use the same elliptical function presented in Chapter 3 with the constant terms calculated specifically for the fiducial volume of this analysis.

These constants can be calculated analytically using any one point in the (σ, ζ_1, ζ_2) plane within the fiducial volume ($p_T{}^{\gamma} > 100$GeV, $0.035 < \xi < 0.15$ (0.18) for sector45 (sector56)). Choosing a point where $\zeta_2 = 0$ gives $A = \sigma / \zeta_1^2$. Using an FPMC sample with ζ_1 = 5e-13 and ζ_2 =0, the cross-section is 29.1 fb. Thus, $A = 1.164 \times 10^{26}$. Using the proportionality of 48:40:11 for A:B:C, $B = 9.700 \times 10^{25}$, and $C = 2.668 \times 10^{25}$. The full equation is then

$$\sigma = (1.164 \times 10^{26})\zeta_1^2 + (9.700 \times 10^{25})\zeta_1\zeta_2 + (2.668 \times 10^{25})\zeta_2^2 \qquad 4.7$$

Substituting the output of the Combine tool into the elliptical scaling equation, the following observed (expected) limits are derived on the four photon anomalous coupling parameters:

$$|\zeta_1| < 7.26 \times 10^{-14} \quad (7.09 \times 10^{-14})\ \text{GeV}^{-4} \quad (\zeta_2 = 0),$$
$$|\zeta_2| < 1.48 \times 10^{-13} \quad (1.37 \times 10^{-13})\ \text{GeV}^{-4} \quad (\zeta_1 = 0)$$

The 2D limits on ζ_1, ζ_2 can be seen in Figure 4.27. A comparison of these limits to the limits derived in Chapter 3 is shown in Figure 4.28. A shape-based limit approach is discussed in Appendix B.1.

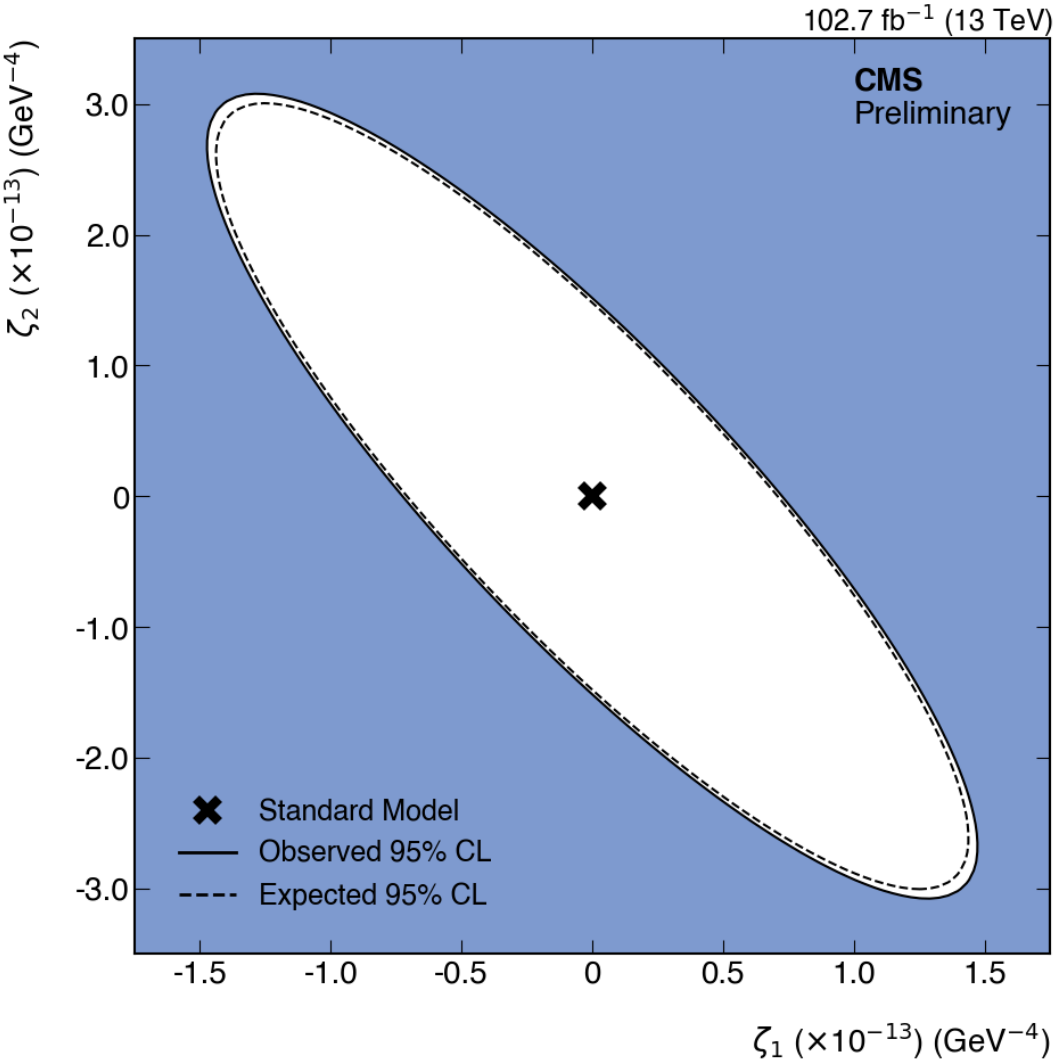

Figure 4.27: Observed and expected limits on AQGC coupling parameters corresponding to the Run II dataset at 95% CL.

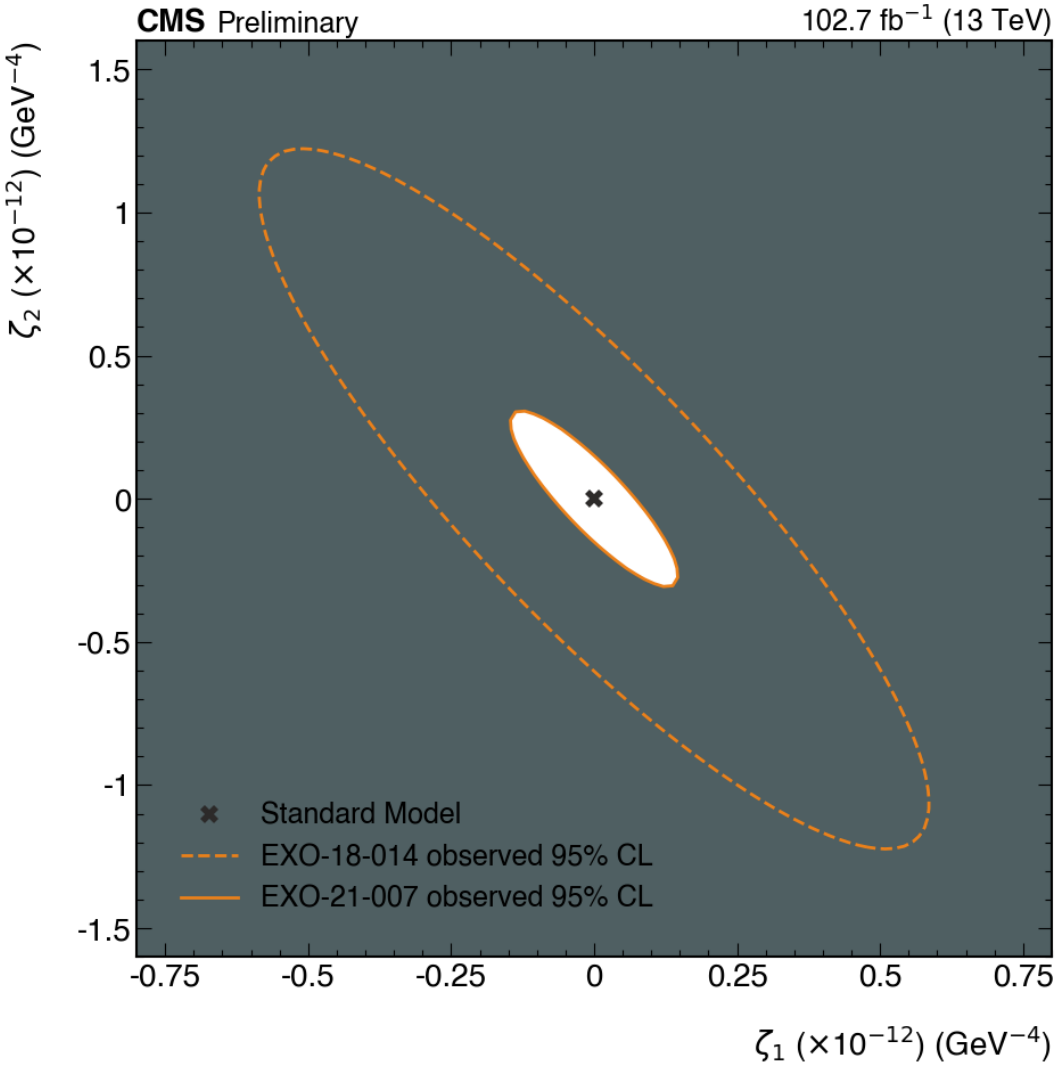

Figure 4.28: Comparison of the observed limits from the 2016 analysis described in Chapter 3, and the Run 2 analysis described in this chapter.

4.5.5 Limits on Axion-Like Particles

The same limit setting procedure is applied to the s-channel exchange of a scalar axion-like particle. Following the approach described in [23], this $\gamma\gamma \to a \to \gamma\gamma$ process can be parameterized as a function of the ALP mass, m_a, and its coupling to the diphoton system, f^{-1}. The signal efficiency for the ALP samples is observed to only depend on the generated ALP mass and not the coupling strength. The efficiency and acceptance factors for each sample and for each year are shown in Tables 4.18, 4.19, and 4.20.

Similarly to the AQGC limits, the asymmetric ξ acceptance is accounted for in each mass point separately since each ALP gives rise to a different ξ distribution.

A scan of the cross-section in the (f^{-1}, m_{ALP}) phase space within the fiducial volume is shown in Figure 4.29. This scan is used to find the limit on f^{-1} for each mass point corresponding to the limit on the cross-section given by the Combine tool.

Mass (GeV)	**CMS** $\epsilon \times A$	**PPS** $\epsilon \times A$	$\epsilon \times A$
500	85.9%	0.02%	0.02%
750	84.7%	10.7%	9.1%
1000	85.0%	19.7%	16.7%
1250	85.1%	17.6%	15.0%
1500	84.8%	7.5%	6.4%
2000	84.8%	0.08%	0.07%

Table 4.18: ALP signal efficiency for 2016 samples generated with $f^{-1} = 10^{-1}$ TeV^{-1} within the fiducial volume. The CMS efficiency is shown in the left column, the PPS efficiency is shown in the middle column, and product of the CMS and PPS efficiencies is shown in the right column. The small efficiencies for the 500 and 2000 GeV mass points are because of the RP acceptance.

Mass (GeV)	**CMS** $\epsilon \times A$	**PPS** $\epsilon \times A$	$\epsilon \times A$
500	81.9%	4.0%	3.3%
750	79.3%	10.9%	8.6%
1000	79.2%	9.1%	7.2%
1250	80.6%	6.8%	5.5%
1500	79.7%	4.1%	3.3%
2000	80.0%	0.06%	0.050%

Table 4.19: ALP signal efficiency for 2017 samples generated with $f^{-1} = 10^{-1}$ TeV^{-1} within the fiducial volume. The CMS efficiency is shown in the left column, the PPS efficiency is shown in the middle column, and product of the CMS and PPS efficiencies is shown in the right column. The small efficiency for the 2000 GeV mass point is because of the RP acceptance.

Mass (GeV)	**CMS** $\epsilon \times A$	**PPS** $\epsilon \times A$	$\epsilon \times A$
500	83.9%	25.5%	21.4%
750	80.8%	46.9%	37.9%
1000	81.5%	39.3%	32.0%
1250	80.8%	31.1%	25.1%
1500	81.1%	21.4%	17.4%
2000	81.1%	1.9%	1.5%

Table 4.20: ALP signal efficiency for 2018 samples generated with $f^{-1} = 10^{-1}$ TeV^{-1} within the fiducial volume. The CMS efficiency is shown in the left column, the PPS efficiency is shown in the middle column, and product of the CMS and PPS efficiencies is shown in the right column. The small efficiency for the 2000 GeV mass point is because of the RP acceptance.

The observed and expected limits resulting from this analysis can be seen in Figure 4.30. These are the strongest limits to date in this region of phase space. A shape-based limit approach is also discussed in Appendix B.2.

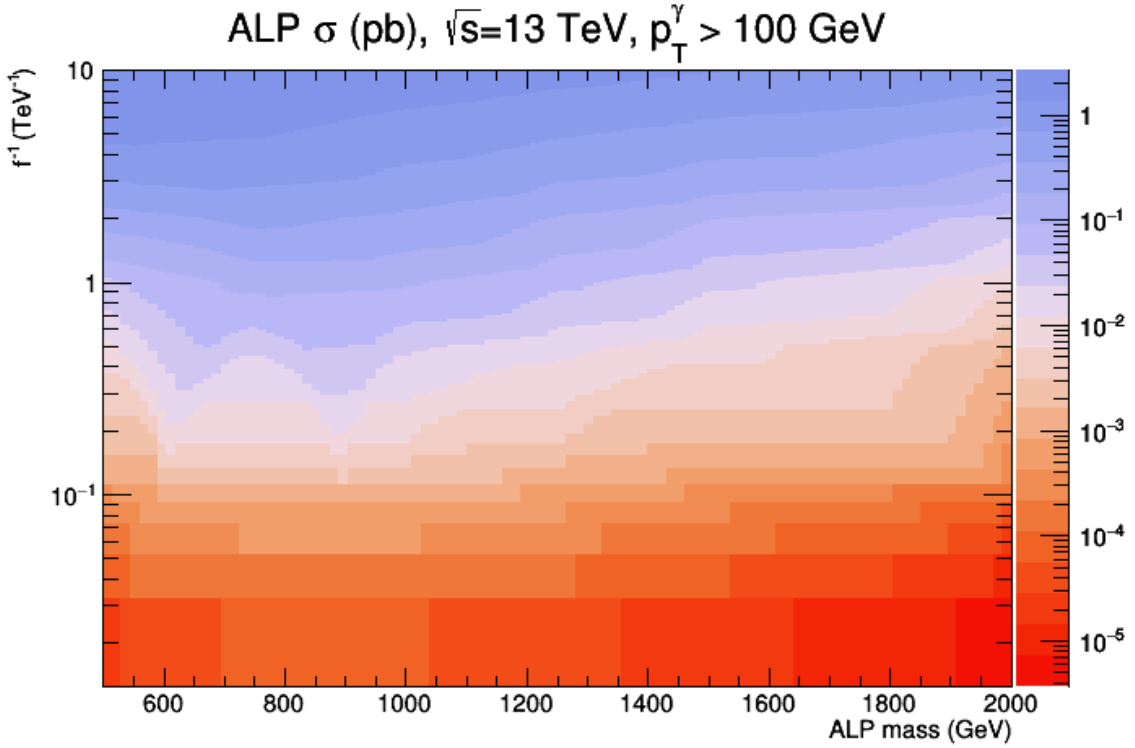

Figure 4.29: A scan of the cross-section as a function of the ALP mass and coupling strength. Interpolation between FPMC points is performed with Delaunay triangles.

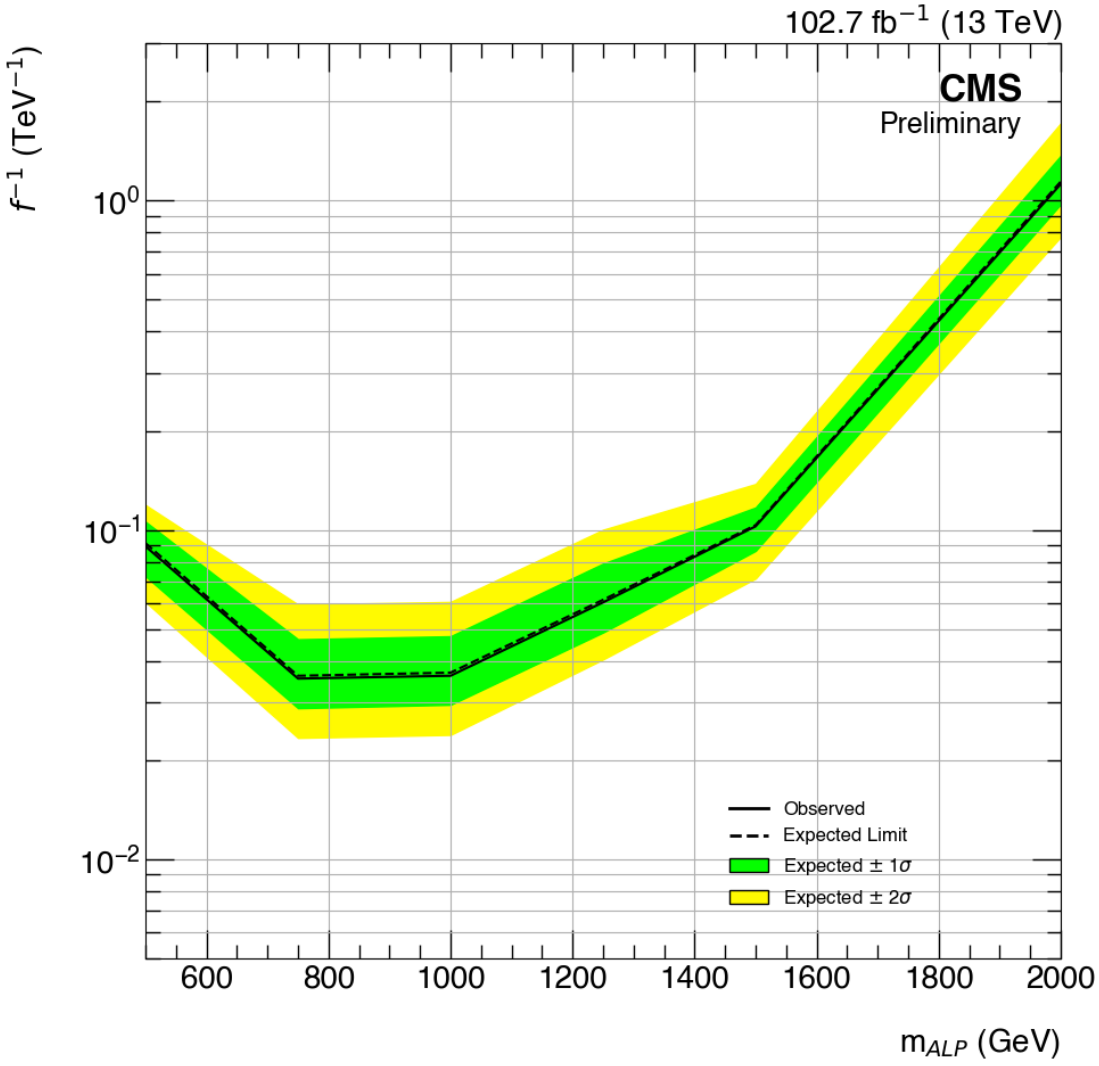

Figure 4.30: Observed and expected limits on ALP production within the fiducial volume of the search. Limits are calculated for ALP masses of 500, 750, 1000, 1250, 1500, and 2000 GeV. The sensitivity for each ALP mass is driven by the PPS acceptance and proton reconstruction efficiency.

Chapter 5: Conclusion

Photon-photon collisions are of great importance to study because of their connection to many BSM models. Furthermore, at high $\gamma\gamma$ energies attainable at the LHC, these interactions allow for the exploration of phase-space that has not yet been excluded from containing new physics. Among the corresponding BSM theories are anomalous quartic gauge couplings and axion-like particles. Many searches have been performed using general purpose detectors to look for large deviations from the SM, but no evidence has been found using these approaches. Instead, a strategy of precision physics has been used to gain the strongest sensitivity to effects of new physics contributing to the 4γ coupling. By measuring the intact protons surviving the electromagnetic interaction and correlating their kinematics to the central system, a large background suppression is obtained allowing for the search of rare processes that would be missed using the standard approaches.

A search was performed targeting exclusive diphoton production with intact protons measured by PPS using the first available dataset from the LHC with proton tagging at standard luminosity conditions from 2016 [61]. Previously, another study was performed using this same dataset that successfully measured the SM $\gamma\gamma \to \ell^+\ell^-$ process at a greater than 5σ level showing that the spectrometer was working as expected. The main difference from the dilepton analysis is that it only required one proton to be tagged whereas this study requires two opposite-side protons to be tagged.

Events are selected having kinematics consistent with the expected signal – high mass, high p_T, and small azimuthal angle separation. The number of background events is estimated using toy diphoton events mixed with protons from data. Radiation damage to the PPS silicon strip detectors was observed in the low ξ regions and therefore it was decided to make a lower cut of 7% of this variable. No events were observed in the data having a diphoton candidate passing the selection criteria and two opposite-side protons. The first limits were placed on the 4γ anomalous coupling as no limits existed prior to this study.

This search was continued by analyzing the full Run 2 dataset available with improved analysis methods including an improved photon ID, a more robust data-driven background estimation, and a larger ξ spectrum. Combining data from 2016, 2017, and 2018 provides the largest dataset with proton-tagging from the LHC at this time. As the detector configuration of PPS changed in each of these three years, the signal efficiency increased over time. An increased understanding of the efficiencies and uncertainties on the proton reconstruction allowed for probing virtually the full ξ spectrum within the forward detector acceptance. The background was estimated for each year separately using a completely data driven approach and was found to be consistent with the observation from data. The limits on the 4γ anomalous coupling were increased by an order of magnitude with respect to the previous study. The 1D limits on the coupling parameters

are

$$|\zeta_1| < 7.07 \times 10^{-14}\ \text{GeV}^{-4} \quad (\zeta_2 = 0)$$
$$|\zeta_2| < 1.48 \times 10^{-13}\ \text{GeV}^{-4} \quad (\zeta_1 = 0)$$

Additionally, the increase in luminosity allowed for the most stringent limits to date on axion-like particle production in the high mass range of the analysis. At the strongest point, the limit reaches $f^{-1} = 2.7{\times}10^{-2}$ TeV^{-1} at an ALP mass of 750 GeV.

This work has provided insight into the landscape of BSM physics coupling to photons by using unique analysis techniques at the LHC. The Run 3 data-taking period is now beginning and PPS has plans to operate during all phases with a similar experimental setup as in 2018. With increased luminosity and the power of proton tagging, new regions of phase space will be explored where evidence for new physics could exist.

Appendix A: Inclusive background yield correction

As discussed in Section 3.3.3, a flat 9.9% yield correction is accounted for in the elastic signal search region for the dominant $\gamma\gamma + j$ inclusive background.

Additionally, a reweighting of this background was extracted from the discrepancy observed in the acoplanarity distribution in the inclusive control region. As shown in Figure A.1, a log-linear templated fit is performed on the observed/expected ratio for this kinematic variable. This shape is then used as a weighting function (per diphoton candidate) and applied to the main inclusive background quoted above. Figure A.2 shows the acoplanarity distribution in the inclusive control region before and after the reweighting.

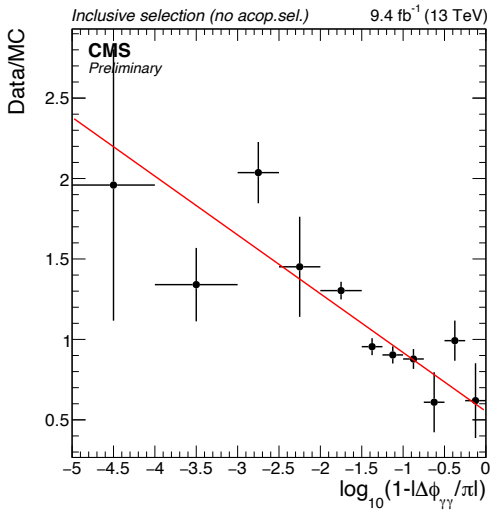

Figure A.1: A log-linear fit to the data/MC acoplanarity distribution for the inclusive control region (without the acoplanarity selection), used as an input to the events reweighting.

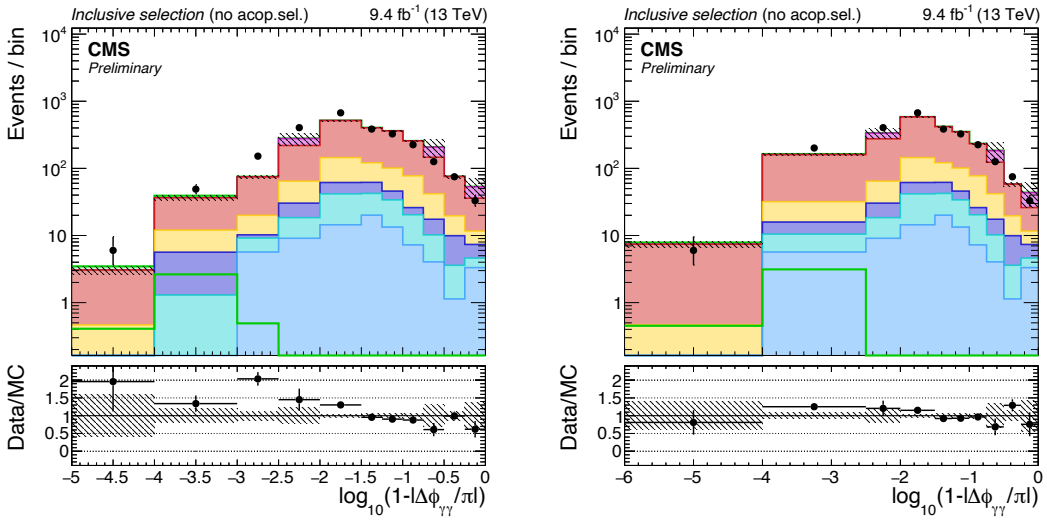

Figure A.2: Acoplanarity distribution for the inclusive control region before (left), and after (right) the event reweighting.

As a closure test shown in Figure A.3, the effect of this reweighting can be observed in a better agreement at the preselection level described in the text.

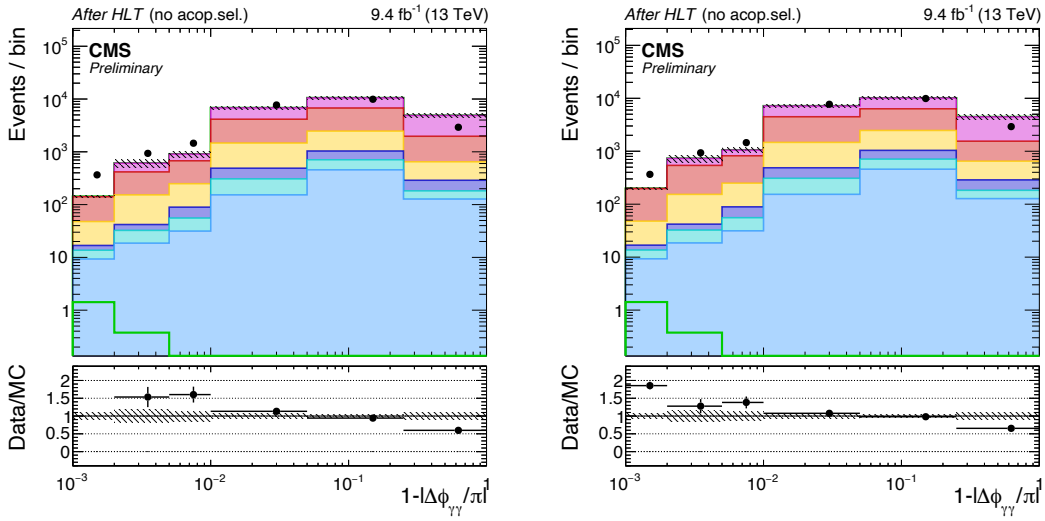

Figure A.3: Diphoton acoplanarity for the preselection defined in the text, before (left) and after the per-pair reweighting is applied on the main inclusive background sample.

In Figure A.4 however, a flat deficit of 36.9% is observed for distributions of interest in the elastic search region.

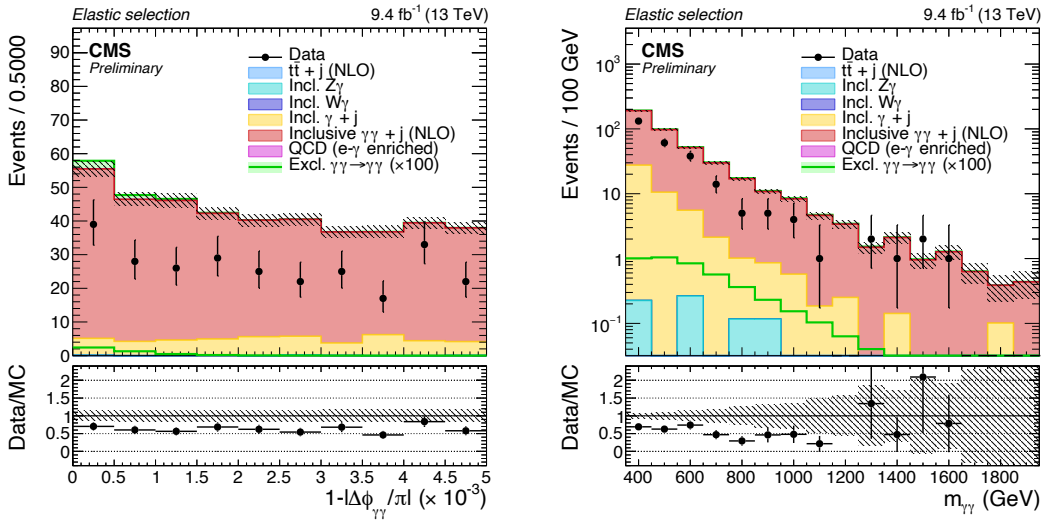

Figure A.4: Diphoton acoplanarity (left) and invariant mass (right) in the elastic signal search region after applying the reweighting described in the text. As observed here, a constant deficit is observed in major diphoton kinematic variables.

This deficit is hence treated as a systematic uncertainty for the inclusive backgrounds yield correction procedure.

Appendix B: Run 2 shape based limits

Shape-based limits can be utilized to strengthen the reach of the analysis by discriminating the signal shape with respect to the background shape. However, since the expected background is very small, it doesn't form a true "shape" and therefore isn't the best treatment of the limits.

The work that has been done to investigate the shape-base approach is shown here in this appendix. The shape-based results use the same event yield, background estimation, signal efficiency, and systematic uncertainties as detailed in sections 4.5.4 and 4.5.5.

B.1 AQGC shape-based limits

Since the background is expected at low ξ and the signal is expected at high ξ, a shape-based approach is used within the Combine tool to improve the limits. To incorporate the two ξ values into the one histogram required by the Combine tool, the two ξ values are summed. The difference between the sum of the ξ values for signal and background can be seen in Figure B.1. The signal shape is taken from signal protons simulated using the PPS direct simulation, and the background shape is taken from proton ξ values of events falling in the 2σ matching window in the default background estimation method. Uncertainty on the signal shape coming from the proton reconstruction is accounted for by providing "up" and "down" histograms for the signal shape to the Combine tool. The up and down histograms are created by shifting the proton ξ values up and down by the systematic uncertainty on the reconstruction. In a similar way, the uncertainty on the background shape is accounted for by providing these same types of histograms to the Combine tool. The up histogram is taken as the alternative estimation method that provides the largest difference between the default estimation method histogram. The down histogram is then generated as the symmetric histogram with respect to the default histogram.

The results from the Combine tool can then be used to derive limits on the four-photon anomalous coupling. The shape-based observed (expected) results for 2016, 2017, 2018, and combined are given in Equations B.1, B.2, B.3, and B.4, respectively.

$$\sigma\ pp \to p\gamma\gamma p \mid \xi_p \in \xi^{PPS} < 8.18\ (8.09)\ \text{fb} \tag{B.1}$$

$$\sigma\ pp \to p\gamma\gamma p \mid \xi_p \in \xi^{PPS} < 6.32\ (4.59)\ \text{fb} \tag{B.2}$$

$$\sigma\ pp \to p\gamma\gamma p \mid \xi_p \in \xi^{PPS} < 0.520\ (0.588)\ \text{fb} \tag{B.3}$$

$$\sigma\ pp \to p\gamma\gamma p \mid \xi_p \in \xi^{PPS} < 0.582\ (0.521)\ \text{fb} \tag{B.4}$$

Substituting the AQGC cross-sections calculated above, the following observed limits

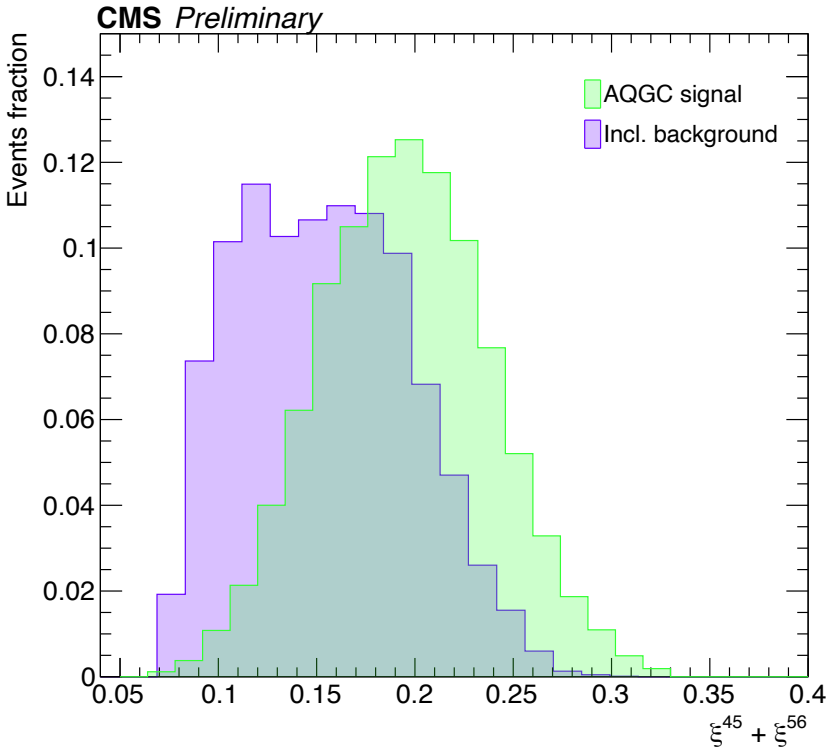

Figure B.1: The sum of the ξ values for both signal and background. These distributions are used for a shape-based limit setting approach.

are derived for 2016, 2017, 2018, and combined in equations B.5, B.7, B.9, and B.11, respectively.

$$| \zeta_1 | < 2.65 \times 10^{-13}\ \text{GeV}^{-4}\ (\zeta_2 = 0) \quad \text{B.5}$$

$$| \zeta_2 | < 5.54 \times 10^{-13}\ \text{GeV}^{-4}\ (\zeta_1 = 0) \quad \text{B.6}$$

$$| \zeta_1 | < 2.33 \times 10^{-13}\ \text{GeV}^{-4}\ (\zeta_2 = 0) \quad \text{B.7}$$

$$| \zeta_2 | < 4.87 \times 10^{-13}\ \text{GeV}^{-4}\ (\zeta_1 = 0) \quad \text{B.8}$$

$$| \zeta_1 | < 0.668 \times 10^{-13}\ \text{GeV}^{-4}\ (\zeta_2 = 0) \quad \text{B.9}$$

$$| \zeta_2 | < 1.40 \times 10^{-13}\ \text{GeV}^{-4}\ (\zeta_1 = 0) \quad \text{B.10}$$

$$| \zeta_1 | < 0.707 \times 10^{-13}\ \text{GeV}^{-4}\ (\zeta_2 = 0) \quad \text{B.11}$$

$$| \zeta_2 | < 1.48 \times 10^{-13}\ \text{GeV}^{-4}\ (\zeta_1 = 0) \quad \text{B.12}$$

The expected 2D limits on ζ_1, ζ_2 from this full Run 2 analysis with respect to the limits from the previous 2016-only analysis can be seen in Figure B.2. The limits from this analysis corresponding to each year of the Run II period individually can be seen in Figure B.3.

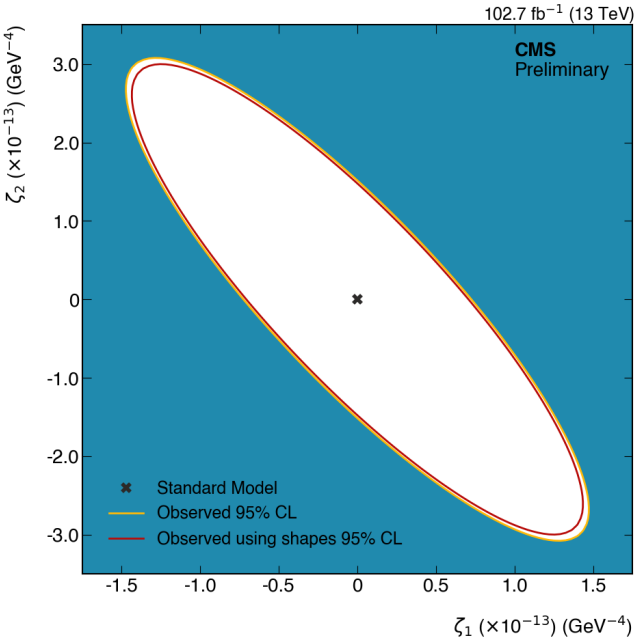

Figure B.2: A comparison between the limits placed by this analysis and the shape based limits described in this Appendix.

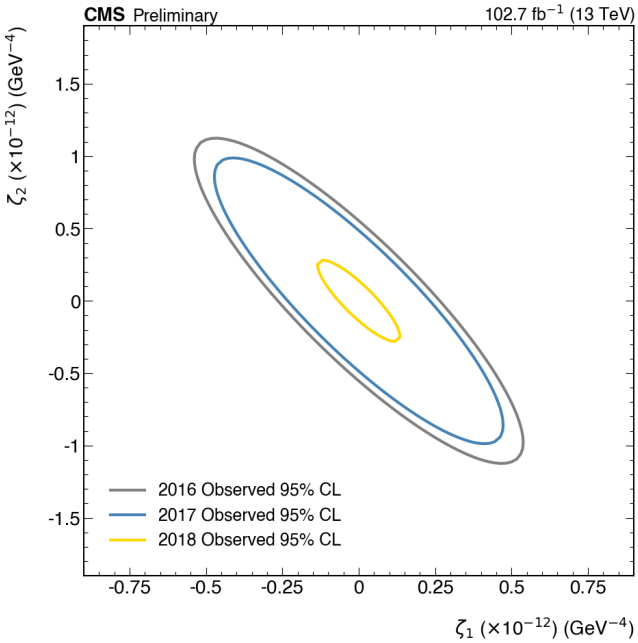

Figure B.3: Expected shape-based limits on AQGC coupling parameters using a shape-based approach. Contours are shown for the limits corresponding to each year of data taking during Run II.

B.2 ALP shape-based limits

A shape-based approach is also implemented in the Combine tool for the ALP signal using the missing mass of the forward proton system as the variable for discrimination. The shapes for the various mass points as well as the background can be seen in Figure B.4. In the same way as the AQGC shapes, up and down histograms are provided to the Combine tool using the uncertainty on the proton reconstruction for the signal shapes and the alternative background estimation methods for the background shape.

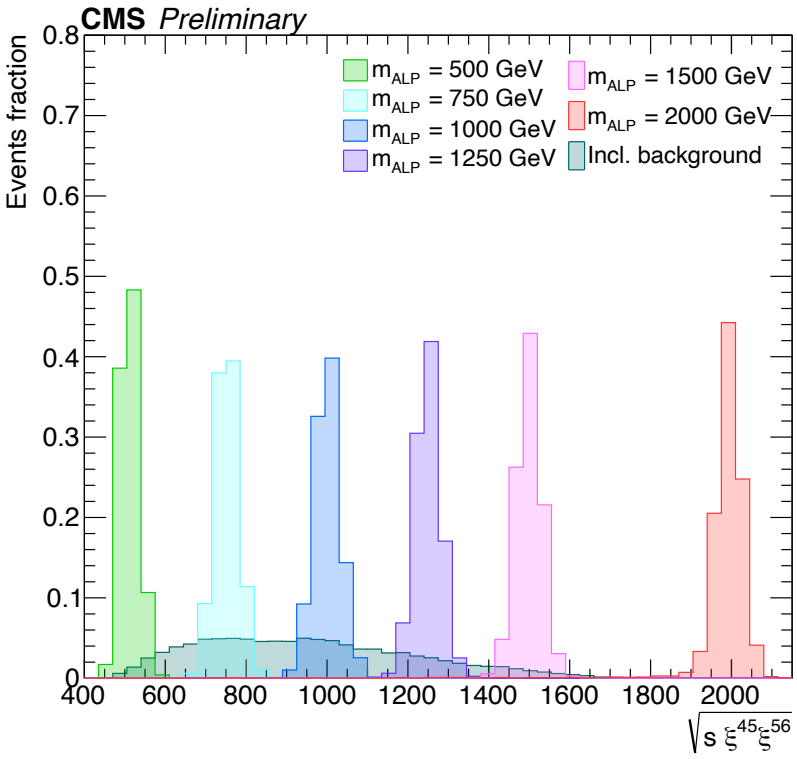

Figure B.4: The missing mass of the forward proton system given by $\sqrt{s\xi^{45}\xi^{56}}$ (where $\sqrt{s}$ is the center of mass energy) for the ALP signals and background. The distributions are used for a shape based limit setting method.

The resulting limits from this shape-based approach can be seen in Figure B.5. The deviation from the expected limit at the 1250 GeVmass point comes from the one observed event, which corresponds to a missing mass of 1202 GeV.

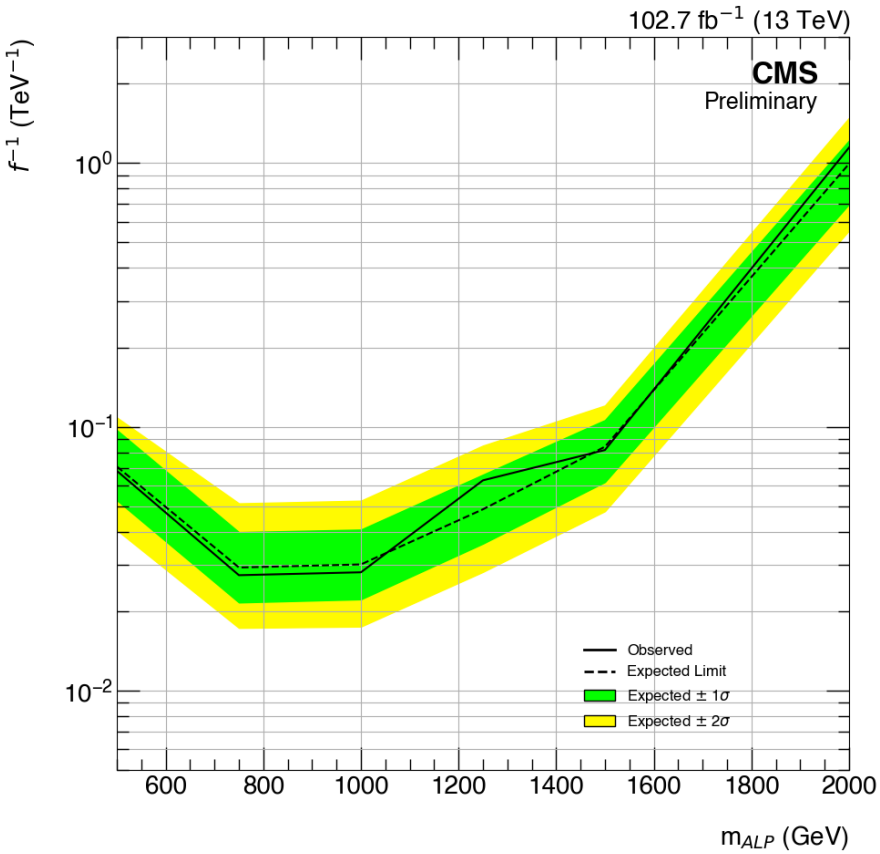

Figure B.5: Observed and expected shape-based limits on ALP production within the fiducial volume of the search. The sensitivity for each ALP mass is driven by the PPS acceptance and proton reconstruction efficiency.

Bibliography

[1] B. Abi *et al.* (Muon g-2 Collaboration), "Measurement of the Positive Muon Anomalous Magnetic Moment to 0.46 ppm," *Phys. Rev. Lett.*, vol. 126, p. 141801, 2021 doi:10.1103/PhysRevLett.126.141801

[2] A. Abulencia *et al.* (CDF Collaboration), "Observation of Exclusive Electron-Positron Production in Hadron-Hadron Collisions," *Phys. Rev. Lett.*, vol. 98, p. 112001, 2007 doi:10.1103/PhysRevLett.98.112001

[3] T. Aaltonen *et al.* (CDF Collaboration), "Observation of exclusive charmonium production and $\gamma + \gamma$ to $\mu^+\mu^-$ in $p\bar{p}$ collisions at $\sqrt{s} = 1.96$ TeV," *Phys. Rev. Lett.*, vol. 102, p. 242001, 2009 doi:10.1103/PhysRevLett.102.242001

[4] E. J. Williams, "Nature of the high-energy particles of penetrating radiation and status of ionization and radiation formulae," *Phys. Rev.*, vol. 45, pp. 729–730, 1934 doi:10.1103/PhysRev.45.729

[5] E. Fermi, "E. Sulla teoria dell' urto tra atomi e corpuscoli elettrici," *Nuovo Cim*, vol. 2, pp. 143–158, 1925 doi:10.1007/BF02961914

[6] D. d'Enterria and G. G. da Silveira, "Observing light-by-light scattering at the Large Hadron Collider," *Phys. Rev. Lett.*, vol. 111, p. 080405, 2013 doi:10.1103/PhysRevLett.111.080405, 10.1103/PhysRevLett.116.129901 [Erratum: Phys. Rev. Lett.116,no.12,129901(2016)].

[7] S. Klein and P. Steinberg, "Photonuclear and Two-photon Interactions at High-Energy Nuclear Colliders," *Ann. Rev. Nucl. Part. Sci.*, vol. 70, pp. 323–354, 2020 doi:10.1146/annurev-nucl-030320-033923

[8] L. A. Harland-Lang, M. Tasevsky, V. A. Khoze, and M. G. Ryskin, "A new approach to modelling elastic and inelastic photon-initiated production at the LHC: SuperChic 4," *Eur. Phys. J. C*, vol. 80, no. 10, p. 925, 2020 doi:10.1140/epjc/s10052-020-08455-0

[9] L. A. Harland-Lang, V. A. Khoze, M. G. Ryskin, and W. J. Stirling, "Standard candle central exclusive processes at the Tevatron and LHC," *Eur. Phys. J. C*, vol. 69, pp. 179–199, 2010 doi:10.1140/epjc/s10052-010-1404-5

[10] M. Aaboud *et al.* (ATLAS Collaboration), "Evidence for light-by-light scattering in heavy-ion collisions with the ATLAS detector at the LHC," *Nature Phys.*, vol. 13, no. 9, pp. 852–858, 2017 doi:10.1038/nphys4208

[11] A. M. Sirunyan *et al.* (CMS Collaboration), "Evidence for light-by-light scattering and searches for axion-like particles in ultraperipheral PbPb collisions at $\sqrt{s_{NN}} = 5.02$ TeV," *Phys. Lett. B*, vol. 797, p. 134826, 2019 doi:10.1016/j.physletb.2019.134826

[12] G. Aad *et al.* (ATLAS Collaboration), "Observation of light-by-light scattering in ultra-peripheral Pb+Pb collisions with the ATLAS detector," *Phys. Rev. Lett.*, vol. 123, no. 5, p. 052001, 2019 doi:10.1103/PhysRevLett.123.052001

[13] R. S. Van Dyck, P. B. Schwinberg, and H. G. Dehmelt, "New High Precision Comparison of electron and Positron G Factors," *Phys. Rev. Lett.*, vol. 59, pp. 26–29, 1987 doi:10.1103/PhysRevLett.59.26

[14] H. N. Brown *et al.* (Muon g-2 Collaboration), "Precise measurement of the positive muon anomalous magnetic moment," *Phys. Rev. Lett.*, vol. 86, pp. 2227–2231, 2001 doi:10.1103/PhysRevLett.86.2227

[15] R. N. Li, A. I. Milshtein, and V. M. Strakhovenko, "Splitting of a high-energy photon in a strong Coulomb field," *J. Exp. Theor. Phys.*, vol. 85, pp. 1049–1059, 1997 doi:10.1134/1.558376

[16] S. L. Adler, "Photon splitting and photon dispersion in a strong magnetic field," *Annals Phys.*, vol. 67, pp. 599–647, 1971 doi:10.1016/0003-4916(71)90154-0

[17] D. L. Burke *et al.*, "Positron production in multi - photon light by light scattering," *Phys. Rev. Lett.*, vol. 79, pp. 1626–1629, 1997 doi:10.1103/PhysRevLett.79.1626

[18] C. Bula *et al.* (E144 Collaboration), "Observation of nonlinear effects in Compton scattering," *Phys. Rev. Lett.*, vol. 76, pp. 3116–3119, 1996 doi:10.1103/PhysRevLett.76.3116

[19] K. Agashe, R. Contino, and A. Pomarol, "The Minimal composite Higgs model," *Nucl. Phys. B*, vol. 719, pp. 165–187, 2005 doi:10.1016/j.nuclphysb.2005.04.035

[20] K. Agashe, A. Delgado, M. J. May, and R. Sundrum, "RS1, custodial isospin and precision tests," *JHEP*, vol. 08, p. 050, 2003 doi:10.1088/1126-6708/2003/08/050

[21] L. Randall and R. Sundrum, "A Large mass hierarchy from a small extra dimension," *Phys. Rev. Lett.*, vol. 83, pp. 3370–3373, 1999 doi:10.1103/PhysRevLett.83.3370

[22] S. Fichet, G. von Gersdorff, B. Lenzi, C. Royon, and M. Saimpert, "Light-by-light scattering with intact protons at the LHC: from Standard Model to New Physics," *JHEP*, vol. 02, p. 165, 2015 doi:10.1007/JHEP02(2015)165

[23] C. Baldenegro, S. Fichet, G. Von Gersdorff, and C. Royon, "Searching for axion-like particles with proton tagging at the LHC," *JHEP*, vol. 06, p. 131, 2018 doi:10.1007/JHEP06(2018)131

[24] R. D. Peccei and H. R. Quinn, "CP Conservation in the Presence of Instantons," *Phys. Rev. Lett.*, vol. 38, pp. 1440–1443, 1977 doi:10.1103/PhysRevLett.38.1440

[25] S. Fichet, "Shining Light on Polarizable Dark Particles," *JHEP*, vol. 04, p. 088, 2017 doi:10.1007/JHEP04(2017)088

[26] P. Svrcek and E. Witten, "Axions In String Theory," *JHEP*, vol. 06, p. 051, 2006 doi:10.1088/1126-6708/2006/06/051

[27] S. Fichet, G. von Gersdorff, O. Kepka, B. Lenzi, C. Royon, and M. Saimpert, "Probing new physics in diphoton production with proton tagging at the Large Hadron Collider," *Phys. Rev.*, vol. D89, p. 114004, 2014 doi:10.1103/PhysRevD.89.114004

[28] S. Fichet, G. von Gersdorff, and C. Royon, "Scattering light by light at 750 GeV at the LHC," *Phys. Rev.*, vol. D93, no. 7, p. 075031, 2016 doi:10.1103/PhysRevD.93.075031

[29] M. Bauer, M. Neubert, and A. Thamm, "Collider Probes of Axion-Like Particles," *JHEP*, vol. 12, p. 044, 2017 doi:10.1007/JHEP12(2017)044

[30] S. Chatrchyan *et al.* (CMS Collaboration), "Observation of a New Boson at a Mass of 125 GeV with the CMS Experiment at the LHC," *Phys. Lett. B*, vol. 716, pp. 30–61, 2012 doi:10.1016/j.physletb.2012.08.021

[31] G. Aad *et al.* (ATLAS Collaboration), "Observation of a new particle in the search for the Standard Model Higgs boson with the ATLAS detector at the LHC," *Phys. Lett. B*, vol. 716, pp. 1–29, 2012 doi:10.1016/j.physletb.2012.08.020

[32] "Linear accelerator 2," Sep 2012. [Available Online]: https://cds.cern.ch/record/1997427

[33] "The Proton Synchrotron Booster," Jul 2012. [Available Online]: https://cds.cern.ch/record/1997372

[34] "The Super Proton Synchrotron," Jan 2012. [Available Online]: https://cds.cern.ch/record/1997188

[35] D. Boussard and T. P. R. Linnecar, "The LHC Superconducting RF System," CERN, Geneva, Tech. Rep. LHC-Project-Report-316. CERN-LHC-Project-Report-316, Dec 1999. [Available Online]: https://cds.cern.ch/record/410377

[36] T. Sakuma (CMS Collaboration Collaboration), "Cutaway diagrams of CMS detector," May 2019. [Available Online]: https://cds.cern.ch/record/2665537

[37] A. M. Sirunyan *et al.* (CMS Collaboration), "Performance of the CMS Level-1 trigger in proton-proton collisions at $\sqrt{s}$ = 13 TeV," *JINST*, vol. 15, p. P10017, 2020 doi:10.1088/1748-0221/15/10/P10017

[38] V. Khachatryan *et al.* (CMS Collaboration), "The CMS trigger system," *JINST*, vol. 12, p. P01020, 2017 doi:10.1088/1748-0221/12/01/P01020

[39] "CMS Luminosity Measurements for the 2016 Data Taking Period," CERN, Geneva, Tech. Rep. CMS-PAS-LUM-17-001, 2017. [Available Online]: https://cds.cern.ch/record/2257069

[40] "CMS luminosity measurement for the 2017 data-taking period at $\sqrt{s}$ = 13 TeV," CERN, Geneva, Tech. Rep. CMS-PAS-LUM-17-004, 2018. [Available Online]: https://cds.cern.ch/record/2621960

[41] "CMS luminosity measurement for the 2018 data-taking period at $\sqrt{s}$ = 13 TeV," CERN, Geneva, Tech. Rep. CMS-PAS-LUM-18-002, 2019. [Available Online]: https://cds.cern.ch/record/2676164

[42] A. M. Sirunyan *et al.* (CMS Collaboration), "Particle-flow reconstruction and global event description with the CMS detector," *JINST*, vol. 12, p. P10003, 2017 doi:10.1088/1748-0221/12/10/P10003

[43] M. Cacciari, G. P. Salam, and G. Soyez, "The anti-k_t jet clustering algorithm," *JHEP*, vol. 04, p. 063, 2008 doi:10.1088/1126-6708/2008/04/063

[44] M. Cacciari, G. P. Salam, and G. Soyez, "FastJet user manual," *Eur. Phys. J. C*, vol. 72, p. 1896, 2012 doi:10.1140/epjc/s10052-012-1896-2

[45] V. Khachatryan *et al.* (CMS Collaboration), "Jet energy scale and resolution in the CMS experiment in pp collisions at 8 TeV," *JINST*, vol. 12, p. P02014, 2017 doi:10.1088/1748-0221/12/02/P02014

[46] S. Chatrchyan *et al.* (CMS Collaboration), "The CMS experiment at the CERN LHC," *JINST*, vol. 3, p. S08004, 2008 doi:10.1088/1748-0221/3/08/S08004

[47] S. Chatrchyan *et al.* (CMS Collaboration), "Description and performance of track and primary-vertex reconstruction with the CMS tracker," *JINST*, vol. 9, p. P10009, 2014 doi:10.1088/1748-0221/9/10/P10009

[48] W. Adam *et al.* (CMS Tracker Group Collaboration), "The CMS Phase-1 Pixel Detector Upgrade," *JINST*, vol. 16, no. 02, p. P02027, 2021 doi:10.1088/1748-0221/16/02/P02027

[49] "Track impact parameter resolution for the full pseudo rapidity coverage in the 2017 dataset with the CMS Phase-1 Pixel detector," Oct 2020. [Available Online]: https://cds.cern.ch/record/2743740

[50] A. Benaglia (CMS Collaboration Collaboration), "The CMS ECAL performance with examples," CERN, Geneva, Tech. Rep. CMS-CR-2013-430, Nov 2013. [Available Online]: https://cds.cern.ch/record/1632384

[51] P. K. Siddireddy (CMS Collaboration), "The CMS ECAL Trigger and DAQ system: electronics auto-recovery and monitoring," 6 2018.

[52] S. Chatrchyan *et al.* (CMS Collaboration), "Energy Calibration and Resolution of the CMS Electromagnetic Calorimeter in *pp* Collisions at $\sqrt{s}$ = 7 TeV," *JINST*, vol. 8, p. P09009, 2013 doi:10.1088/1748-0221/8/09/P09009

[53] V. Khachatryan *et al.* (CMS Collaboration), "Performance of photon reconstruction and identification with the CMS detector in proton-proton collisions at $\sqrt{s}$ = 8TeV," *JINST*, vol. 10, p. P08010, 2015 doi:10.1088/1748-0221/10/08/P08010

[54] A. M. Sirunyan *et al.* (CMS Collaboration), "Calibration of the CMS hadron calorimeters using proton-proton collision data at $\sqrt{s}$ = 13 TeV," *JINST*, vol. 15, no. 05, p. P05002, 2020 doi:10.1088/1748-0221/15/05/P05002

[55] U. Amaldi, R. Biancastelli, C. Bosio, G. Matthiae, J. V. Allaby, W. Bartel, G. Cocconi, A. N. Diddens, R. W. Dobinson, and A. M. Wetherell, "The Energy dependence of the proton proton total cross-section for center-of-mass energies between 23 and 53 GeV," *Phys. Lett. B*, vol. 44, pp. 112–118, 1973 doi:10.1016/0370-2693(73)90315-8

[56] E. Noschis *et al.* (TOTEM Collaboration), "Final size planar edgeless silicon detectors for the TOTEM experiment," *Nucl. Instrum. Meth. A*, vol. 563, pp. 41–44, 2006 doi:10.1016/j.nima.2006.01.111

[57] M. Albrow, M. Arneodo, V. Avati, J. Baechler, N. Cartiglia, M. Deile, M. Gallinaro, J. Hollar, M. Lo Vetere, K. Oesterberg, N. Turini, J. Varela, D. Wright, and C. CMS-TOTEM, "CMS-TOTEM Precision Proton Spectrometer," Tech. Rep. CERN-LHCC-2014-021. TOTEM-TDR-003. CMS-TDR-13, Sep 2014. [Available Online]: https://cds.cern.ch/record/1753795

[58] F. Nemes, "LHC optics determination with proton tracks measured in the CT-PPS detectors in 2016, before TS2," CERN, CERN-TOTEM-NOTE 2017-002, 2017. [Available Online]: http://cds.cern.ch/record/2256433

[59] J. Kašpar, "Alignment of CT-PPS detectors in 2016, before TS2," CERN, CERN-TOTEM-NOTE 2017-001, 2017. [Available Online]: http://cds.cern.ch/record/2256296

[60] A. M. Sirunyan *et al.* (CMS, TOTEM Collaboration), "Observation of proton-tagged, central (semi)exclusive production of high-mass lepton pairs in pp collisions at 13 TeV with the CMS-TOTEM precision proton spectrometer," *JHEP*, vol. 07, p. 153, 2018 doi:10.1007/JHEP07(2018)153

[61] "First search for exclusive diphoton production at high mass with intact protons in proton-proton collisions at $\sqrt{s}$ = 13 TeV at the LHC," CERN, Geneva, Tech. Rep. CMS-PAS-EXO-18-014, 2020. [Available Online]: https://cds.cern.ch/record/2725141

[62] S. Zenz, *SM H to GG Software Status and Analysis Plans*, 2015. [Available Online]: https://indico.cern.ch/event/447066/contributions/1106799/attachments/1168497/1685678/Zenz-FLASHggStatusAndAnalysisPlans-Hgg-12Oct2015-v2.pdf

[63] J. Alwall, R. Frederix, S. Frixione, V. Hirschi, F. Maltoni, O. Mattelaer, H. S. Shao, T. Stelzer, P. Torrielli, and M. Zaro, "The automated computation of tree-level and next-to-leading order differential cross sections, and their matching to parton shower simulations," *JHEP*, vol. 07, p. 079, 2014 doi:10.1007/JHEP07(2014)079

[64] R. D. Ball *et al.* (NNPDF Collaboration), "Parton distributions for the LHC Run II," *JHEP*, vol. 04, p. 040, 2015 doi:10.1007/JHEP04(2015)040

[65] T. Sjöstrand, S. Ask, J. R. Christiansen, R. Corke, N. Desai, P. Ilten, S. Mrenna, S. Prestel, C. O. Rasmussen, and P. Z. Skands, "An Introduction to PYTHIA 8.2," *Comput. Phys. Commun.*, vol. 191, p. 159, 2015 doi:10.1016/j.cpc.2015.01.024

[66] M. Boonekamp, A. Dechambre, V. Juranek, O. Kepka, M. Rangel, C. Royon, and R. Staszewski, "FPMC: A Generator for forward physics," 2011.

[67] S. Agostinelli *et al.* (GEANT4 Collaboration), "GEANT4: A simulation toolkit," *Nucl. Instrum. Meth. A*, vol. 506, p. 250, 2003 doi:10.1016/S0168-9002(03)01368-8

[68] V. M. Budnev, I. F. Ginzburg, G. V. Meledin, and V. G. Serbo, "The Two photon particle production mechanism. Physical problems. Applications. Equivalent photon approximation," *Phys. Rept.*, vol. 15, pp. 181–281, 1975 doi:10.1016/0370-1573(75)90009-5

[69] L. A. Harland-Lang, V. A. Khoze, and M. G. Ryskin, "Exclusive physics at the LHC with SuperChic 2," *Eur. Phys. J.*, vol. C76, no. 1, p. 9, 2016 doi:10.1140/epjc/s10052-015-3832-8

[70] V. A. Khoze, A. D. Martin, and M. G. Ryskin, "Diffraction at the LHC," *Eur. Phys. J.*, vol. C73, p. 2503, 2013 doi:10.1140/epjc/s10052-013-2503-x

[71] A. V. Manohar, P. Nason, G. P. Salam, and G. Zanderighi, "The Photon Content of the Proton," *JHEP*, vol. 12, p. 046, 2017 doi:10.1007/JHEP12(2017)046

[72] V. Khachatryan *et al.* (CMS Collaboration), "Performance of Photon Reconstruction and Identification with the CMS Detector in Proton-Proton Collisions at sqrt(s) = 8 TeV," *JINST*, vol. 10, no. 08, p. P08010, 2015 doi:10.1088/1748-0221/10/08/P08010

[73] A. M. Sirunyan *et al.* (CMS Collaboration), "Measurements of Higgs boson properties in the diphoton decay channel in proton-proton collisions at $\sqrt{s}$ = 13 TeV," *JHEP*, vol. 11, p. 185, 2018 doi:10.1007/JHEP11(2018)185

[74] A. M. Sirunyan *et al.* (CMS Collaboration), "Search for physics beyond the standard model in high-mass diphoton events from proton-proton collisions at $\sqrt{s}$ = 13 TeV," *Phys. Rev. D*, vol. 98, no. 9, p. 092001, 2018 doi:10.1103/PhysRevD.98.092001

[75] S. Chatrchyan *et al.* (CMS Collaboration), "Measurement of the Inclusive W and Z Production Cross Sections in pp Collisions at $\sqrt{s}$ = 7 TeV," *JHEP*, vol. 10, p. 132, 2011 doi:10.1007/JHEP10(2011)132

[76] S. Chatrchyan *et al.* (CMS Collaboration), "Exclusive photon-photon production of muon pairs in proton-proton collisions at $\sqrt{s}$ = 7 TeV," *JHEP*, vol. 01, p. 052, 2012 doi:10.1007/JHEP01(2012)052

[77] CMS HIG group, *Higgs Combine tool*, 2019. [Available Online]: http://cms-analysis.github.io/HiggsAnalysis-CombinedLimit/

[78] L. Breiman, J. Friedman, R. A. Olshen, and C. J. Stone, *Classification and regression trees*. Chapman and Hall/CRC, 1984. ISBN 978-0-412-04841-8

[79] T. Junk, "Confidence level computation for combining searches with small statistics," *Nucl. Instrum. Meth. A*, vol. 434, pp. 435–443, 1999 doi:10.1016/S0168-9002(99)00498-2

[80] A. L. Read, "Modified frequentist analysis of search results (The CL(s) method)," in *Workshop on Confidence Limits*, pp. 81–101, 8 2000.

[81] "Procedure for the LHC Higgs boson search combination in Summer 2011," CERN, Geneva, Tech. Rep. CMS-NOTE-2011-005. ATL-PHYS-PUB-2011-11, Aug 2011. [Available Online]: https://cds.cern.ch/record/1379837